CHARACTERIZATION OF LUBRICANT DROPLETS FOR INTERNAL MINIMUM

QUANTITY LUBRICATION

A Thesis

by

AMLA SHIRISH PATIL

Submitted to the Office of Graduate and Professional Studies of
Texas A&M University
in partial fulfillment of the requirements for the degree of

MASTER OF SCIENCE

Chair of Committee,   Wayne Nguyen Hung
Co-Chair of Committee,   Bruce Li-Jung Tai
Committee Members,   Satish Bukkapatnam
Head of Department,   Andreas Polycarpou

December 2020

Major Subject: Mechanical Engineering

ABSTRACT

This study characterized airborne diameter and distribution of two commercially available lubricants' droplets for internal minimum quantity lubrication (MQL). The effect of varying air pressure on the resultant droplets and drilling performance was studied.

Resultant droplet sizes and contact angles on A380 aluminum were evaluated. Droplet formation at the drill tip was investigated with a high-speed camera. Drilling tests with MQL, flood coolants, and dry condition were performed to validate the effectiveness of through tool MQL.

Airborne droplet diameters were highly sensitive to the coolant channel sizes. Overall, the airborne droplets of Castrol oil were larger than that of Coolube oil at different air pressures and drill sizes. Contact angle of Coolube oil is about half of that for Castrol oil. High speed imaging showed the tendency of high viscosity Castrol oil sticking to the drill tip. Built-up-edges were significant when drilling A380 aluminum with Castrol oil. Due to high machinability of A380 aluminum, the hole diameter and hole cylindricity were the same when drilling with MQL or flood coolant, excessive amount of MQL lubricant did not improve the hole quality, but without coolant the hole cylindricity doubled.

The result of this study will be applied for high aspect ratio drilling of A380 aluminum engine blocks. The same procedure can be extended to study deep hole drilling of difficult-to-machine alloys and additively manufactured metals.

DEDICATION

      This thesis is dedicated to my mother Shobha, father Shirish, sister Sonal, and brother-in-law Dipesh, who motivated and supported me throughout the pursuit of my graduate studies. I am grateful for their thoughtfulness, patience and encouragement.

ACKNOWLEDGEMENTS

.

CONTRIBUTORS AND FUNDING SOURCES

Contributors

This work was supported by a thesis committee consisting of Professor Wayne Hung and Bruce Tai of the Department of Mechanical Engineering and Professor Satish Bukkapatnam of the Department of Industrial and Systems Engineering.

All other work conducted for the thesis was completed by the student.

Funding Sources

NOMENCLATURE

A	Projected area of the deposited droplet (μm^2)
a	Temperature gradient (K/m)
A_p	Air pressure (kPa)
C_c	Coolant concentration in water (%)
C_k	k^{th} cluster
$/C_k/$	Number of data samples in k^{th} cluster
C_y	Cylindricity (μm)
d	Airborne diameter of droplet (μm)
D	Hydraulic diameter of the channel (mm)
D_n	Nozzle diameter (in)
d'	Projected diameter of the droplet (μm)
D'	Drill diameter (mm)
d_p	Part thickness (mm)
f	Chip load (mm/flute)
f_D	Darcy friction factor (constant)
f_r	Feed rate (mm/min)
F_f	Flood coolant flow (L/hr)
g	Droplet zone diameter (mm)
H_o	Hole oversize (μm)
ID	Inside diameter (mm)

K	Total number of clusters
k	Thermal conductivity (W/mK)
K'	Constant for projected droplet diameter calculation
K''	Constant for fluid pressure calculation
L	Length of the channel (mm)
N	Spindle speed (rpm)
n	Number of flutes per revolution (flute/rev)
OD	Outside diameter (mm)
O_q	Oil quantity (mL/hr)
P	Projected diameter of resultant droplet (μm)
P'	Pressure at nozzle (kPa)
Q_n	Flow rate of water from nozzle (m^3/hr)
q	Heat flux (W/m^2)
R	Radius of drilled hole (mm)
t	Drilling time (s)
V	Mean velocity of the fluid (m/s)
V'	Cutting speed (m/min)
V''	Volume of large drop for contact angle measurement (mm^3)
V'''	Volume of droplet on glass plate by Unist system (mm^3)
x	Distance between the centres of the two impact zones (mm)
x_{ij}	Observations in the cluster

$x_{i'j}$	Observation in the cluster other than x_{ij}
y	Distance between the drill and the glass panel (mm)
z	Distance between the coolant hole centre and glass slide (mm)
α	Included angle of drill (°)
β	Cone angle (°)
γ	Shear rate for lubricant (1/s)
φ	Droplet zone coverage angle (°)
ΔP	Pressure drop (Pa)
θ	Contact angle (°)
θ'	Centre line angle (°)
μ	Dynamic viscosity of lubricant (dyne·s/cm^2)
ρ	Density of the fluid (kg/m^3)
σ	Shear stress of lubricant (dyne/cm^2)
ACF	Atomization-based cutting fluid
BUE	Built up edge
CFRP	Carbon Fiber Reinforced Polymer
CMM	Coordinate measuring machine
CVD	Chemical vapour deposition
EC	Mineral oil-based emulsion
FRP	Fiber Reinforced Plastic
FSO	Flood of soluble oil

HOSO	High oleic soyabean oil
HPC	High pressure cooling
HSS	High-speed steel
HSS-Co	High-speed steel with cobalt binder
LOSO	Low oleic soybean oil
MQCL	Minimum quantity cooling lubrication
MQL	Minimum quantity lubrication
MRR	Material removal rate
MWF	Metalworking fluid
PVD	Physical vapour deposition
SEM	Scanning Electron Microscopy
WC	Tungsten carbide
WC-Co	Tungsten carbide in cobalt matrix

TABLE OF CONTENTS

LIST OF FIGURES

xiii

xiv

xvi

LIST OF TABLES

Page

CHAPTER 1

INTRODUCTION

Machining generates heat due to friction at the tool-workpiece interface and shear deformation of the workpiece. These frictional forces can adversely affect the tool life and the precision of the workpiece. Frictional forces can induce tool wear through several mechanisms; predominantly abrasive tool wear. Traditional flood cooling method of lubrication requires a substantial amount of lubricant in metal cutting processes to reduce the temperature and friction between cutting tool and the workpiece. This is a redundant use of lubricant as most of the lubricant is not delivered exactly to the cutting zone. Flood cooling method requires an additional system to store, filter and pump the recycled coolant for machining. When the useful life of coolant ends, washing the coolant reservoir and disposing the used coolant lead to environmental concerns. These factors contribute to high machining and maintenance cost. Excessive use of coolants raise health and safety concerns at the workplace (Madhukar et al., 2016). On the other hand, dry machining involves high friction causing a decrease in tool life up to 50% compared to machining with a lubricant (Kadirgama et al., 2010).

In contrast, minimum quantity lubrication (MQL) system delivers the minimum quantity of metalworking fluid (MWF) to the cutting zone during machining. In MQL, cutting fluid can be delivered to the cutting zones externally via a nozzle directing to the tool/workpiece interface or internally via built-in channels inside a tool. In an external MQL system, nozzles need to be placed according to the position of the tool and the workpiece. Also, MWF supply from one nozzle might not completely lubricate the cutting

1

zone. The external MQL system is inappropriate when the cutting zone is not easily accessible for lubrication, such as in deep hole drilling. In such cases, an internal MQL system can be used to supply MWF effectively. In this system, the coolant is supplied directly or very close to the cutting zone with internal channels leading to the cutting edges. MQL application results in lower manufacturing cost as compared to traditional cooling method, because of limited use of lubricant and no maintenance cost. Researchers have also observed tool life improvement in machining processes, such as drilling and milling when MQL was used.

1.1. Research motivation

The MQL is emerging as an effective and environmentally friendly substitute to traditional lubrication methods, especially in deep drilling and gun drilling where cutting fluid delivery to the cutting edges is challenging. Although the topic of MQL has been investigated by many researchers, most of the published literature are for external MQL and very limited research papers were dedicated to internal MQL. The objectives of this research study were to understand and optimize the parameters for effective internal MQL. Specifically, the study would: (i) Characterize and compare MQL droplets resulted from two commercially available lubricants, (ii) Study droplet formation and flow exiting from through-tool coolant holes of a twist drill, (iii) Verify the effectiveness of through-tool MQL in actual drilling.

The result of this study will be applied for optimal deep hole drilling of automobile engine blocks.

2

CHAPTER 2

LITERATURE REVIEW

2.1. Tool wear and built-up-edge

Zhang et al. (2008) published a review on drilling process parameters for Ti alloys. The author mentioned the cutting force, cutting temperature, tool wear, tool life, and chip type as important considerations in drilling. Other parameters like feed rate, cutting speed, drill geometry, drill material, and lubricant were specified as important process parameters. These authors included a study of these parameters when drilling a 6.35 mm thick Ti-6al-4V plate at 183 m/min cutting speed, 156 mm^3/s material removal rate (MRR) using double flute, 4 mm size WC-Co twist, WC-Co spiral point drill, and HSS twist drill under dry conditions, internal and external cutting fluid supply. The 5% CIMTECH 500 synthetic MWF was used. The thrust force and torque were measured by a Kistler 9272 dynamometer. Figure 1 shows the thrust force and torque of WC-Co drills at 1470 rpm and 0.051 mm/rev feed (Li et al., 2007). The author concluded that:

- Cutting force

  Feed rate was indicated as the most important parameter impacting the cutting force in drilling Ti alloys. The thrust force and torque increased by 27% and 20% respectively when the feed rate was doubled. 64% decrease in the thrust force and 23% decrease in the torque was noted when the cutting speed was doubled. The larger cutting edge angle and smaller helix angle of the drill resulted in reduced thrust force and torque. Cutting temperature also increased with the cutting speed in drilling.

3
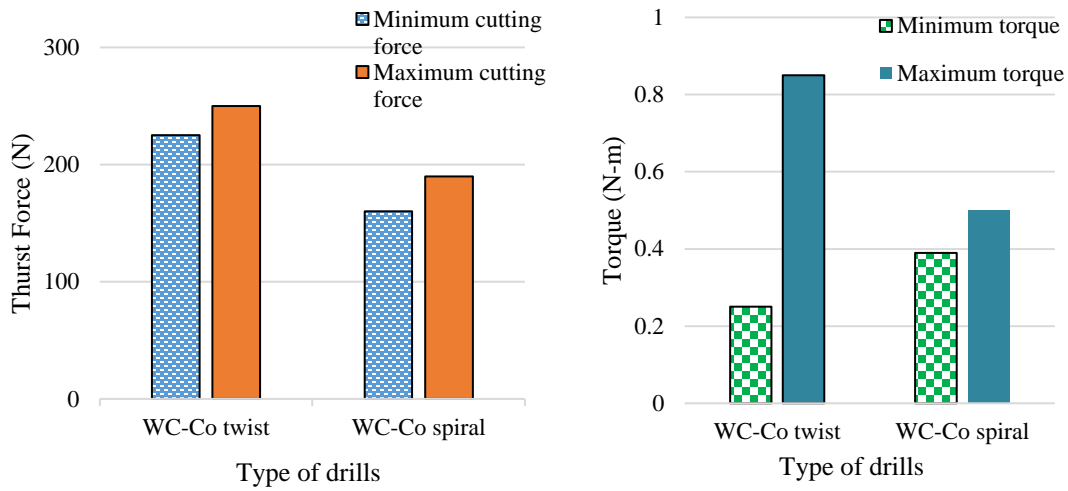
Figure 1. Thrust force and torque with different drills when drilling Ti alloys [Adapted from Zhang et al., 2008]

- Tool wear

  The author stated that the tool wear increased with the feed rate when drilling Ti alloys with a tungsten carbide drill. Tool wear increased by 0.2 mm with 10 m/min increase in cutting speed (Rahim and Sharif, 2006). The larger helix angle of the drill resulted in decreased thrust force and torque, which improved the tool life.

- Hole quality

  The cylindricity of drilled holes increased with cutting speed and feed rate. These two parameters also affected the surface roughness of the drilled holes. Higher feed rate and higher spindle speed resulted in higher surface roughness values. The surface roughness decreased from 1.75 µm to 1.2 µm with increase in cutting speed from 25 m/min to 45 m/min when using tungsten carbide drills in drilling Ti alloys (Rahim & Sharif, 2006).

The work-hardened material affixed to the rake face of the cutting tool during machining is termed as the built-up edge (BUE). The BUE formation is attributed to the high friction and affinity of the tool material and the chip. It can result in chipping and premature failure of the cutting tool (Zhang et al., 2008).

Wang et al. (2016) studied the effects of BUE formation on surface finish when micromilling 316L stainless steel plates with MQL application. The study included $30\times40\times0.5$ mm steel plates. Performance Micro Tools' double flute uncoated tungsten carbide micromills were used. These micromills were flat end tools with 0.406 mm tool diameter, 5 µm tool edge radius, and 1.220 mm flute length. The variable cutting speed of 10, 27, 44, 60 m/min and the variable chip load of 0.05, 0.20, 0.50, 1.00 µm/tooth were utilized for the milling process. The depth of cut was 30 µm. In addition, the conventional milling was performed on the titanium workpiece with a single flute AlTiN coated WC tool (0.8 mm diameter, 5.2° concavity angle), 10 m/min speed, 30 µm depth, 2-8 µm/tooth chip load range, and without lubricants. Another conventional milling experiment was performed on a 6061-T6 aluminium with a double flute uncoated HSS tool (3.175 mm diameter, 3.5° concavity angle), 60 m/min speed, 100 µm depth, 12.7-101.6 µm/tooth chip load range, and without lubricants. The surface roughness study was conducted with Zygo Zegage optical interference microscope, Olympus STM6 microscope, TESCAN Vega LM3 scanning electron microscope (SEM). BUE density was quantified as number of BUE residues per sample image area. Another metric was BUE entropy which considered the dispersion of BUE on the surface. The BUE volume and entropy was the largest at the low cutting speed of 10 m/min (Figure 2). BUE density and volume were identified as

5

important predictors for the surface roughness estimation model with p-values lower than 0.05 in statistical t-test.
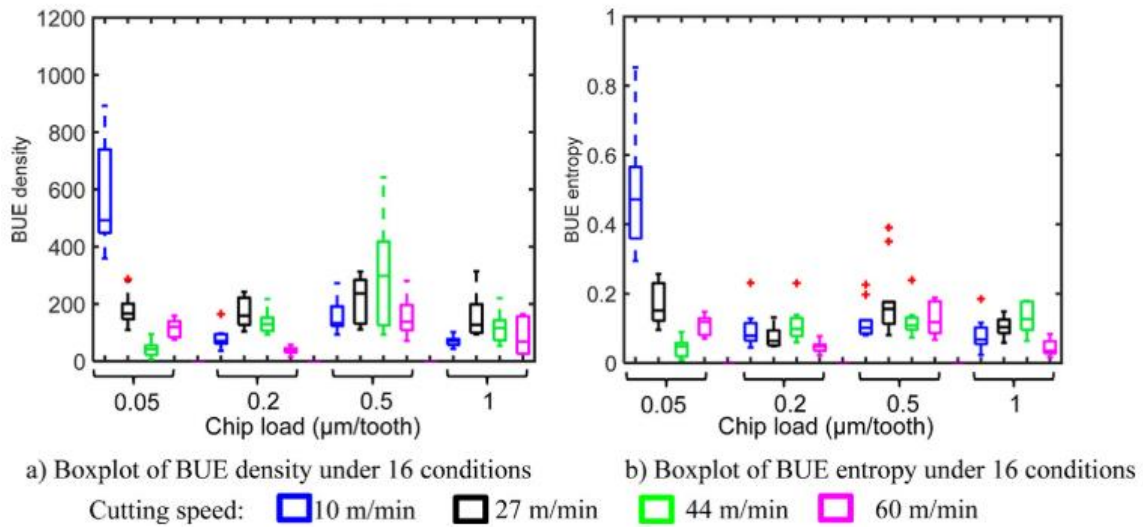
Figure 2. BUE variation with the cutting speed and the chip load [Reprinted from Wang et al., 2016]

Venkatesh and Xue (1996) studied BUE formation on indexable coated carbide inserts when drilling SAE 1018 steel. The Fadal 5 axis CNC machining center was used to drill 10 mm deep holes with the cutting speed of 71 m/min and feed 0.06 mm/rev at 1186 rpm. A quick stop device was used to acquire the real-time data in drilling. Three different inserts with coatings of TiC chemical vapour deposition (CVD), Al_2O_3, TiN physical vapour deposition (PVD), and one insert without coating was used for drilling tests. The hole quality was determined based on the surface roughness, roundness, and waviness of drilled holes. The smallest BUE was observed on the insert with TiC coating. The drilled hole quality was better and tool wear was the highest (0.17 mm) when TiC

coated insert was used. The largest BUE formation was observed with the insert without

coating due to the high friction between the chip and the rake face of the tool.
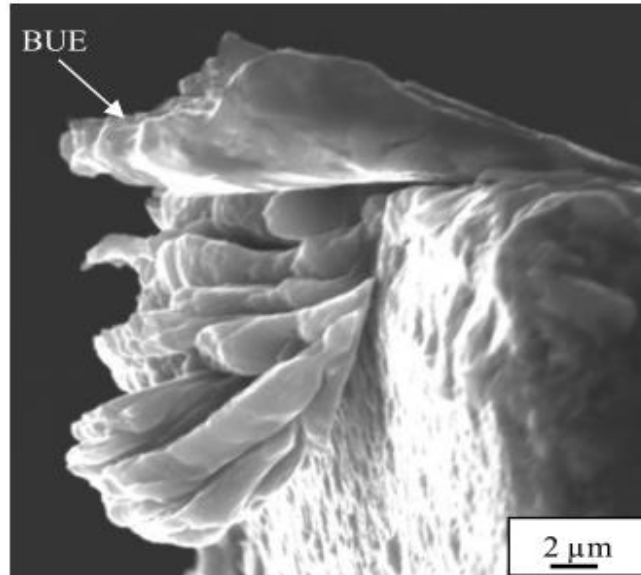
Figure 3. Scanning electron image of typical built-up-edges on a micromilling tool. Micromilling commercially pure titanium with ø0.406 mm tool, 10 m/min speed, 2 µm/tooth chip load, 30 µm depth, MQL. [Reprinted from Kovvuri et al., 2015]
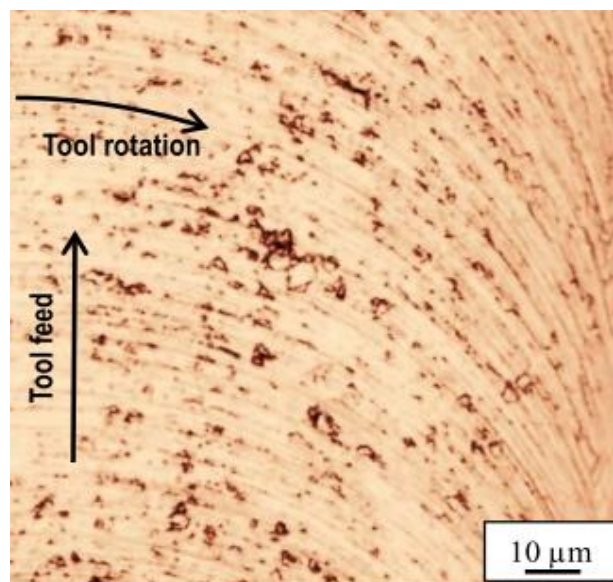
Figure 4. Optical image of typical micromilled surface and embedded built-up-edges. Micromilling with ø0.406 mm tool, 27 m/min speed, 0.10 µm/tooth chip load, 30 µm depth, MQL. [Reprinted from Kovvuri et al., 2015]

7
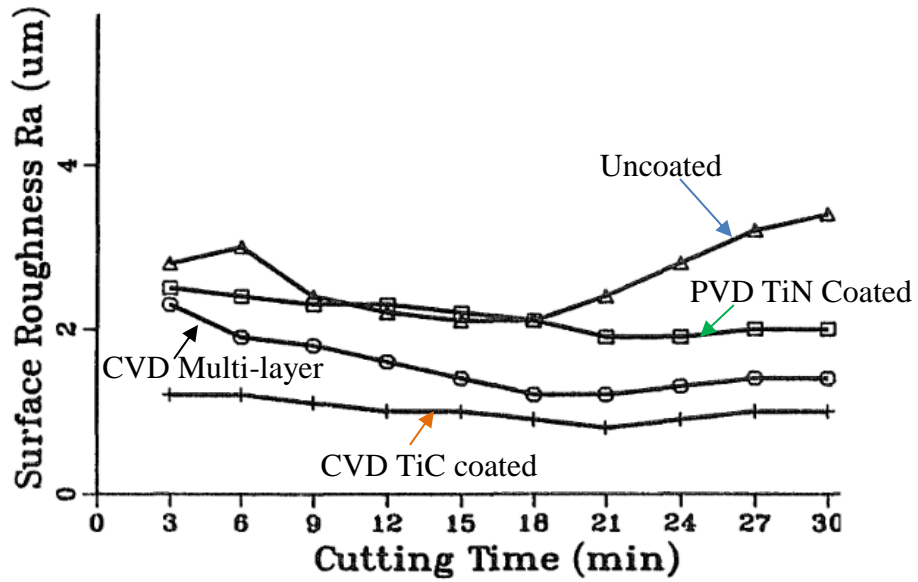
(a) Surface roughness
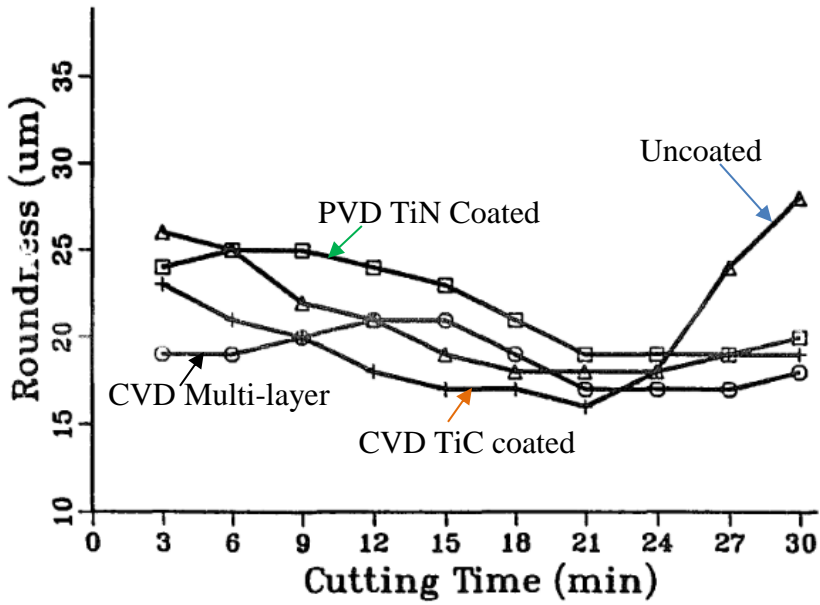
(b) Roundness

Figure 5. (a) **Surface roughness; (b) Roundness of drilled holes with different drill inserts [Adapted from Venkatesh and Xue, 1996]**

Kumar et al. (2013) studied tool wear when drilling Carbon Fiber Reinforced Polymer (CFRP)/ Titanium Alloy (Ti6Al4V) stacks. This study mentioned that the CFRP result in chipping of the tool and the low thermal conductivity of Ti alloy results in BUE. The experiments utilized the Deckel Maho 835 Vertical Machining centre and the Syscon two-component tube type strain gauge drilling dynamometer with Syscon charge amplifier to measure the thrust force and the torque. Tektronix TDS210 digital storage oscilloscope was used to store the variations in the forces and torque. Drilling tests for 100 holes were performed with two drills having 118˚ and 130˚ lip angle. Helix angle was 20˚ for the drill with the 118˚ point angle and 30˚ for the other drill. Chisel edge thicknesses were 1.215 and 0.450 mm for 118˚ and 130˚ point angle drills respectively. Mitutoyo tool makers microscope was used to measure the flank wear and the chisel edge wear. Tool wear was measured with Mitutoyo stereo microscope after drilling 10 holes. The optimized values for the spindle speed and feed were determined using the genetic algorithm. The spindle speed was 859 rpm and feed was 0.0581 mm/rev. Flank wear measured after drilling 100 holes was 0.352 mm for 118˚ point angle drill and 0.138 mm for 130˚ point angle drill. It was concluded that the chisel edge wear is highly impacted by the thrust force with both drills.
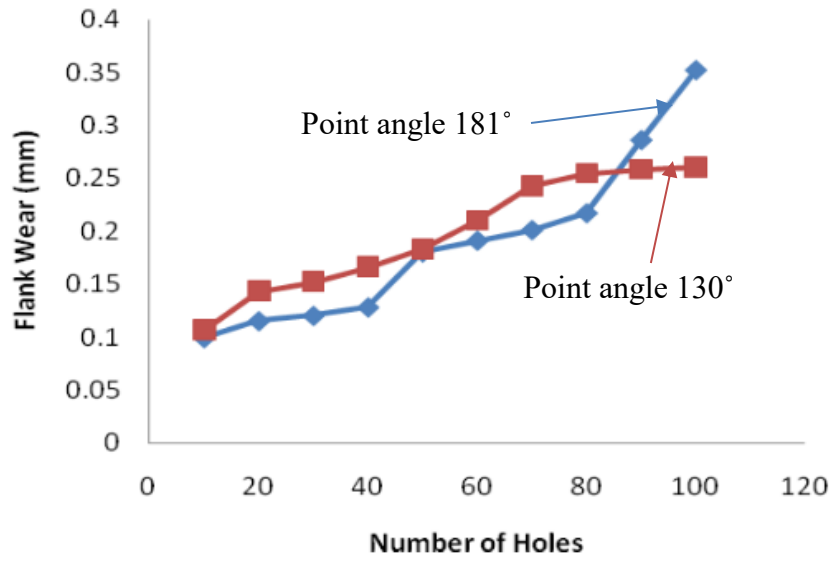
(a)
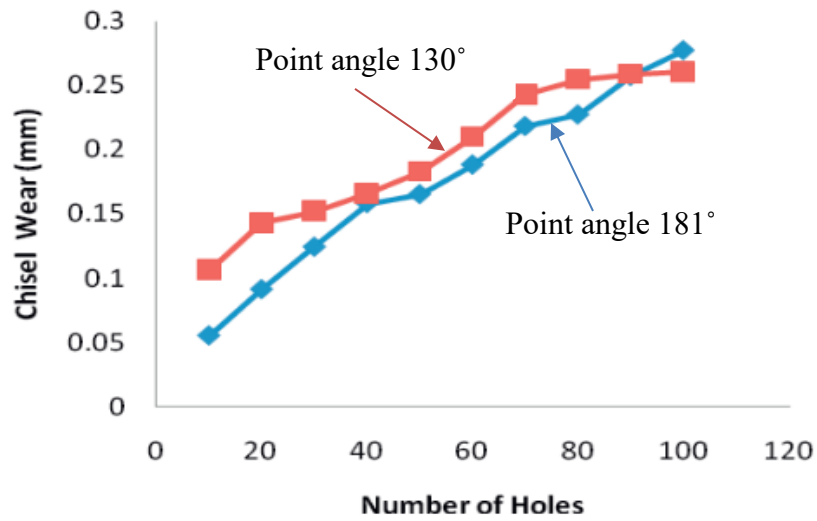
(b)
Figure 6. (a) Flank wear; (b) Chisel wear with different drills with different point angles [Adapted from Kumar et al., 2013]

Ramulu et al. (2001) studied the effect of tool materials when drilling composite and titanium stacks. A 7.62 mm thick multidirectional Gr/Bi composite Fiber-Reinforced Plastic (FRP) with 0.2 mm ply thickness was used for this study. Ti6Al-4V alloy sheet with 3.1 mm thickness was used. The FRP composite was stacked on top of the Ti alloy. A commercial mill with a CNC control and a drive unit was used for drilling. High-speed steel (HSS), high-speed cobalt (HSS-Co), and carbide drills were used. Spindle speed was varied as 325, 660, 1115, 1750, and 2750 rpm. A dynamometer was used to measure the thrust force and torque and a data acquisition system with an amplifier, an oscilloscope and a personal computer was used to record the voltage data. Hole quality was assessed with optical and SEM based on the surface finish and the burr produced. It was observed that the tool wear was more at the outer cutting edges of the tool. This was attributed to the maximum cutting velocity and greater friction at the outer diameter of the drill. The tool wear for HSS drills increased with speed when drilling Ti alloy. Tool wear increased substantially at 1750 rpm with a feed greater than the ply thickness when drilling Gr/Bi-Ti stacks.

2.2. Types of MQL

A suitable lubricant must be used for optimal machining depending on the physical and chemical characteristics of the workpiece and tool materials involved. Sultana et al. (2019) reviewed the effect of different lubrication methods on machining processes. It was concluded that the method of lubrication significantly affects cutting forces, tool-workpiece temperature, tool wear, and surface roughness of the machined part. Traditional flood cooling method used about 20 L/min of lubricant with at least 300 kPa pressure for

effective lubrication. This resulted in safety and health concerns of operators and increased machining cost. Other conventional method, including mist cooling and high pressure cooling (HPC) were discussed in this study. Mist cooling method used water based lubricants with pressurized air for lubrication. As compared to flood cooling method, mist cooling required less lubricant and was more efficient. HPC supplied the coolant to the cutting zone at a pressure of about 5.5 to 35 MPa. Apart from the coolant pressure, tool geometry also affected the lubrication in this method. HPC was mainly used for difficult-to-cut materials due to its cost. Various lubrication methods were proposed as an alternative to traditional cooling methods. Dry machining method did not result into any health hazards for the operators; however, it severely affected the tool wear and tool life due to the high heat generated during machining processes. This restricted the surface finish of the product and also resulted in BUE formation.

Minimum quantity lubrication is a near-dry machining process which can overcome the limitations of dry machining. In MQL, coolant with 10-100 mL/hr flow is delivered with compressed air. Compressed air atomizes the coolant, and the micromist formed is supplied to the cutting zone. Effectiveness of MQL in chip extraction and its positive impact on tool life and surface roughness proposes it as an efficient lubrication technique. The effects of different lubricants on MQL cooling have been reviewed in this study.

Impacts of applying MQL with vegetable based oils, solid lubricants, nanofluids, and ionic liquids are mentioned in the review paper by Sultana et al. (2019).

1. Vegetable oil based MQL

   According to Sultana et al. (2019), vegetable based oils had high heat conductivity of about 0.17 W/mK, which made these suitable for lubrication. In addition, these were renewable and nontoxic, but expensive. These formed a lubricant film because of their triglycerides structures, which eventually reduced friction and heat generated at the cutting zone.

2. MQL with solid lubricants

   Micromist particles generated during MQL method can vaporize before properly lubricating the tool-workpiece interface. Thus, it is challenging to use MQL at higher cutting speeds. Some researchers have studied the effect of solid lubricants, including Molybdenum disulphide, tungsten sulphide, titanium carbide, titanium nitride, titanium diboride, graphite, hexagonal boron nitride, boron oxide, polytetrafluoroethylene, etc. on MQL. It was concluded that solid lubricants can reduce friction at the cutting zone due to the formation of tribofilm, minimize tool wear, and improve material removal rate and surface roughness even at higher cutting speeds. However, their high cost and dependency on an additional coolant limits their application. In addition, this method potentially raises the health and safety concern due to small particle sizes (Sultana et al., 2019).

3. MQL with nanoparticles

   To overcome the thermal instability of conventional lubricants, nanoparticles were proposed as an additive to cutting fluids. Nanoparticles can improve wettability, viscosity, and conductivity of the base cutting oil. These can

form a tribofilm between the tool-workpiece interfaces and reduce the frictional forces. Many researchers have studied the impact of nanoparticles in metal cutting parameters. It has been observed that nanoparticles can reduce the surface roughness by 22% and tool wear by 20% (Sultana et al., 2019). Their higher cost restricts their application in MQL.

4. MQL with ionic liquids

According to Sultana et al. (2019), ionic liquids were liquid salts at less than 100˚C temperature with organic cation and inorganic anion. The base cutting fluid was mixed with ionic liquids to improve their cooling properties. These liquids accelerated tribo-chemical reaction between the lubricant and the cutting zone, which resulted in reduction of tool wear and friction. This novel technique requires more research towards the combination of ionic liquids with base oils.

5. Other techniques

Other innovative lubrication methods, such as, electrostatic MQL, contact charged electrostatic spray lubrication, etc. are proposed in the review by Sultana et al. (2019).

Cryogenic cooling is an environment-friendly method, which involves liquid nitrogen at -196˚C or dry ice at -78.5˚C as coolants. This method facilitates cooling rather than lubrication. It is costly and highly dependent on supply of coolant. Its performance can vary based on workpiece and tool material. Liquid nitrogen can reduce BUE formation and chemical wear significantly. Reduction in tool wear was observed with the use of dry ice as a coolant (Sultana et al., 2019).

Combining two or more methods of lubrication is proposed by some researches for achieving proper lubrication. Some studies claimed that the efficiency with hybrid lubrication methods will be higher. However, the setup for this technique will be more challenging and costly. Detailed study is necessary for this technique.
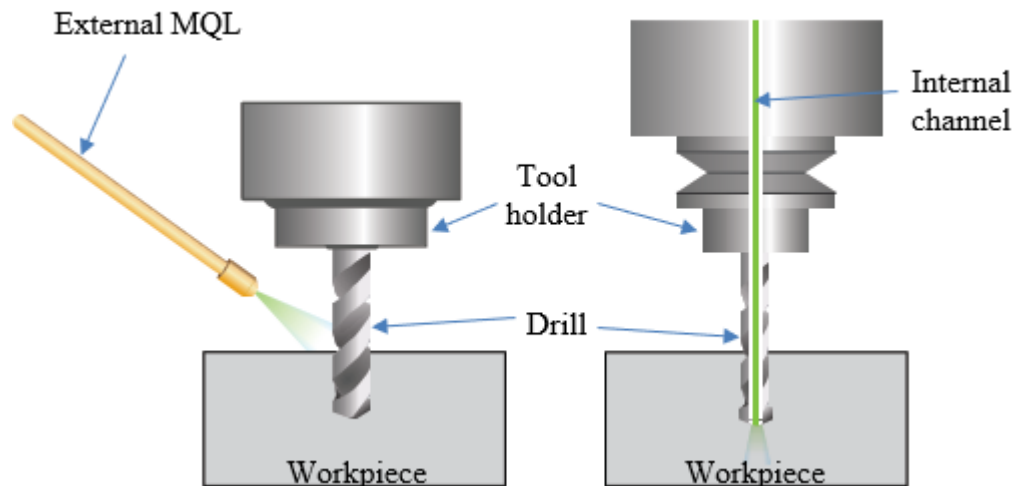
Figure 7. External MQL (left) and internal MQL (right)
[Adapted from Walker, 2013]

Except abrasive processes such as grinding, MQL can be effectively used in cutting operations. In addition, it is a clean, near dry machining process as less than 2 percent of fluid adheres to the metal chips (Dasch & Kurgin, 2010; Walker, 2013). In MQL, cutting fluid can be delivered to the cutting zone externally via one or multiple nozzles or internally via internal channels of a tool (Figure 7).

In an external MQL system, one or more nozzles pointing towards the cutting zone are installed. These nozzles supply the aerosol, formed by the combination of MWF and compressed air, to lubricate the cutting zone. In some cases, one nozzle might not supply the coolant to the complete cutting zone, therefore, more nozzles are used. In this system,

MWF is supplied to the accessible surface of the tool and the workpiece. This system is easier to install and use than internal MQL.

Internal MQL supplies MWF to the cutting zone in the form of micromist through the machine spindle, tool holder, and the tool. In case of deep hole drilling and at high cutting speeds, micromist can be supplied consistently to the cutting zone with internal MQL. As shown in Figure 8, single-channel or dual-channel system can be used in the internal MQL technique. Single-channel system atomized lubricant before it entered the spindle, while for a dual-channel system, the air and oil were carried separately through two coaxial channels and lubricant was atomized at the exit of the spindle or in the tool holder (Walker, 2013). Some authors compared the performance of one and two channel MQL systems. Two-channel system stood out as more advantageous due to the independence of oil quantity with air flow, can sustain at high spindle rotation speed (up to 40,000 rpm), 0.1-0.3 s reaction time, can be operated at lower air pressure (400 kPa), and for highly viscous oils (100 mm^2/s) (Stephenson & Agapiou, 2016).
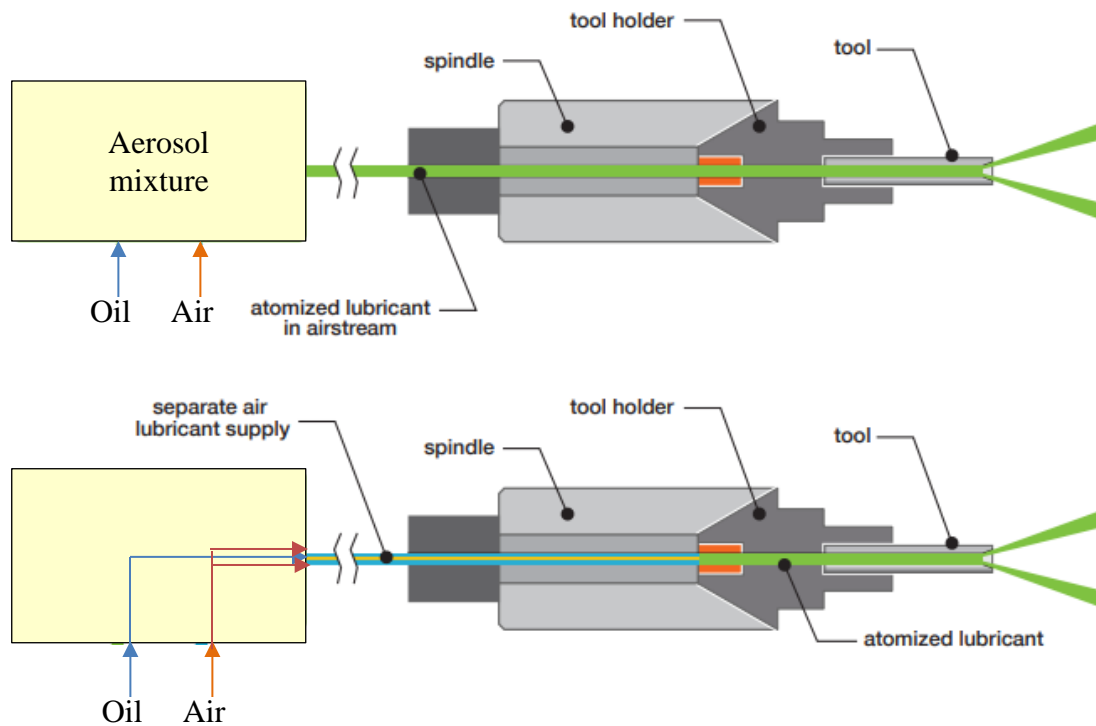
Figure 8. Single and dual-channel internal MQL systems [Adapted from Walker, 2013]

2.3. External MQL

Sivalingam et al. (2020) compared ceramic tool wear with dry cutting and atomized spray of solid lubricants in turning Inconel 718 (In-718). A workpiece of 80 mm diameter and 400 mm length was turned on a PUMA-2000 CNC lathe. WG 300 grade ceramic tool was used for the turning operation. Graphite and molybdenum disulphide were used as solid lubricants with a particle size of 30 to 45 μm and 10 to 15 μm respectively as atomization-based cutting fluid (ACF). These solid lubricants 0.2wt% by weight were mixed with acetone and then mixed with the vegetable-based oil with a concentration 10:90. Lubricant flow rate was kept constant at 50 mL/hr. Cutting speeds

were varied as 250, 300, 350 m/min. The feed was 0.1 mm/rev and the depth of cut was 0.1 or 0.3 mm. Vibration sensors were mounted at the tool holder and spindle head. The TR200 surface roughness tester was used to measure the surface roughness of the workpiece. SEM images were captured to study the tool wear. In case of solid lubricants, the flank wear rate was reduced by 37%, 34%, and 38% at 560 mm cutting length for 250, 300, 350 m/min cutting speed respectively (Figure 9). Overall, the surface roughness reduced by 39-51% (Figure 10) and vibration acceleration by 23-44% with solid lubricants as compared to dry cutting.
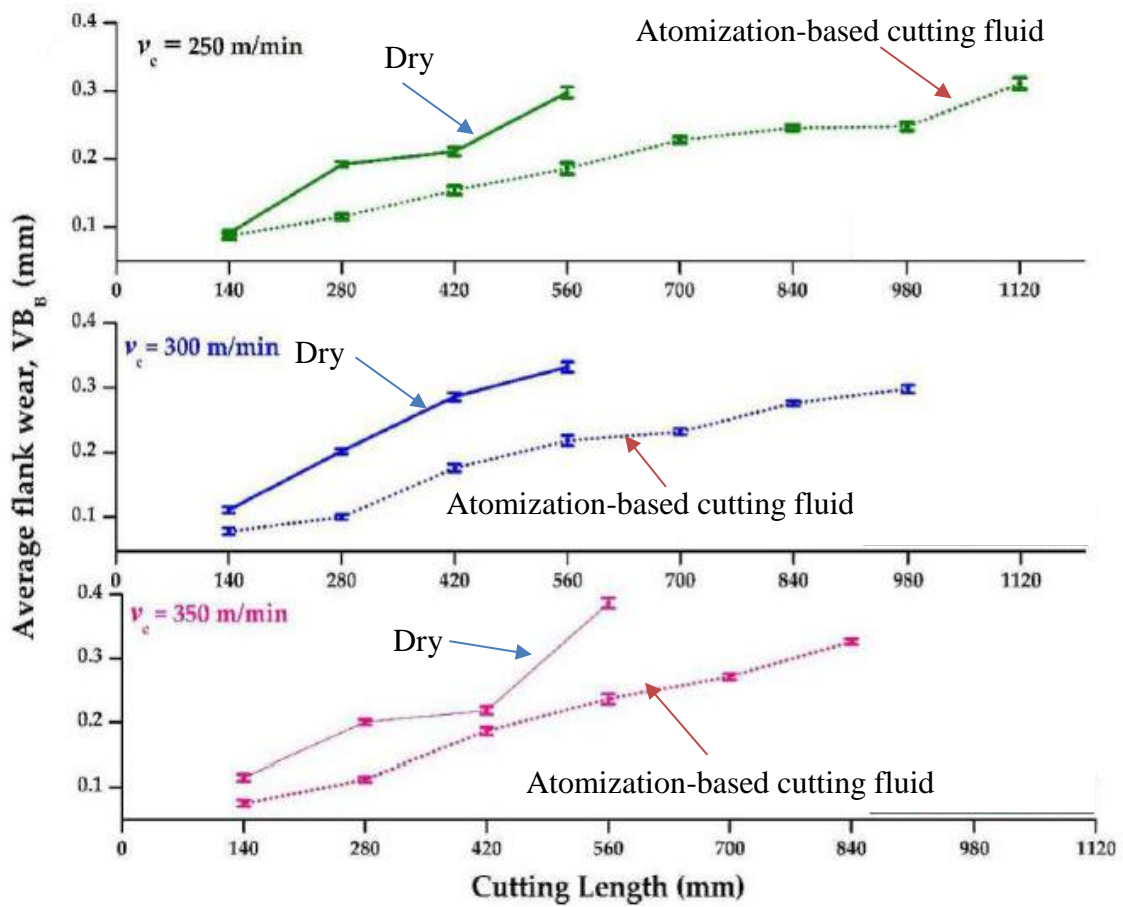
Figure 9. Flank wear with dry cutting and application of solid lubricants at different cutting speeds and 0.1 mm depth of cut [Adapted from Sivalingam et al., 2020]

19
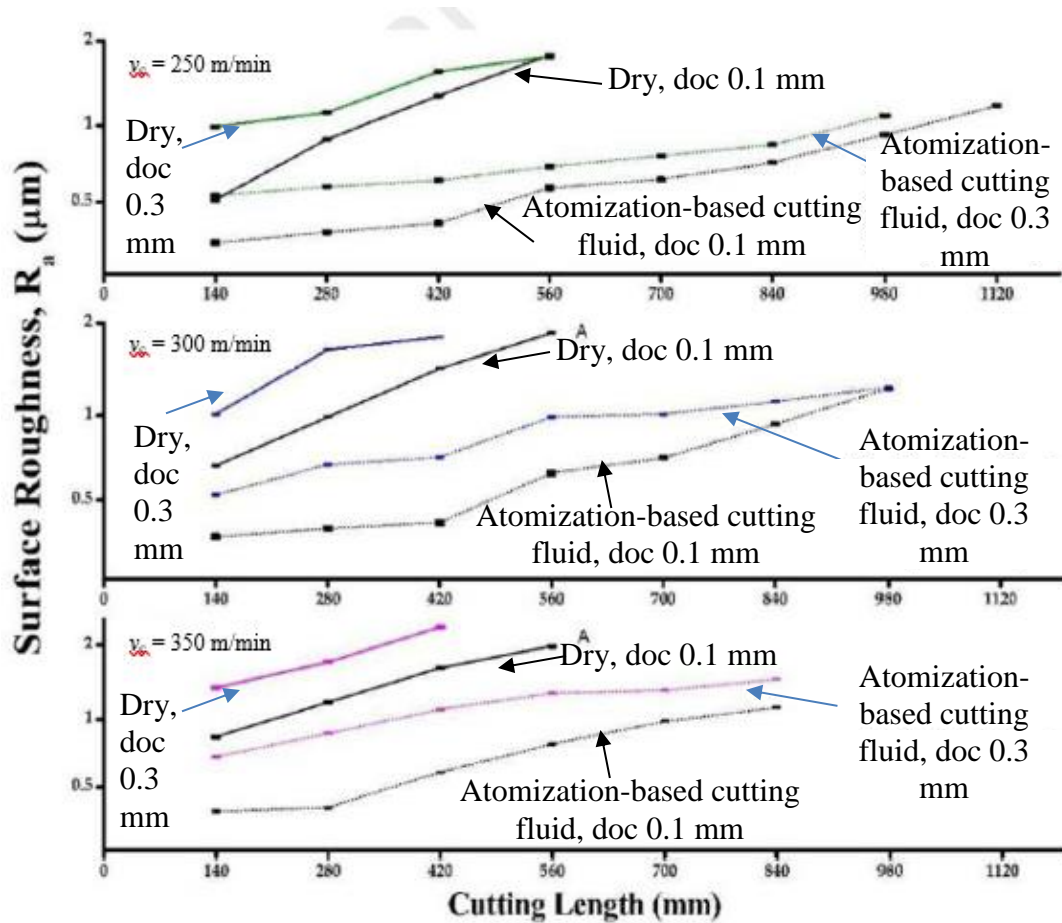
Figure 10. Surface roughness with dry cutting and application of solid lubricants at different cutting speeds (v_c) and depth of cut (doc) [Adapted from Sivalingam et al., 2020]

The performance of MQL with Al_2O_3 nanoparticles in drilling of difficult-to-cut Hardox 500 steel was investigated by Minh Duc et al. (2020). Mazak vertical center smart 530C was used for hard drilling. A MDS127SK carbide drill with TiAlCN coating was used with NOGA MiniCool MC1700 MQL system and Frigid-X Sub-Zero VorteX Tool Cooling Mist System (MQCL). MQL method resulted in low-cooling when machining hard-to-cut materials, while the MQCL method used emulsion-based lubricant to overcome this disadvantage of MQL system. 1.0wt% Al_2O_3 nanoparticles were mixed

with rice bran oil and 5wt% water-based emulsion. The SJ-210 Mitutoyo surface roughness tester was used for surface roughness measurement, the KEYENCE VHX-6000 digital microscope for surface topography, and the Kistler quartz dynamometer 9257BA for the cutting force measurements. Hardox 500 steel workpiece with $150\times100\times15$ mm was drilled with 600 kPa input air pressure and 30 mL/hr oil flow rate. Minitab 18.0 and ANOVA software were used for analyzing the experimental data. Figure 11 shows the effect of input control parameters on drilling thrust force. X1 indicates fluid type (Em: Emulsion, RO: Rice bran oil), X2 cooling method (MQL, MQCL), X3 presence of nanoparticles, X4 cutting speed (m/min), and X5 feed rate (mm/rev). Thus, the emulsion fluid with MQCL and Al_2O_3 nanoparticles at a cutting speed of 15 m/min and feed rate 0.02 mm/rev would result in least drilling thrust force. From Figure 12, it was concluded that MQCL at 15 m/min cutting speed and 0.02 mm/rev feed rate would give better result for surface roughness of the machined component. In addition, tool life increased by 4.5 times with MQCL and nanoparticles, 20 m/min cutting speed, and 0.04 mm/rev feed rate as compared to dry cutting.
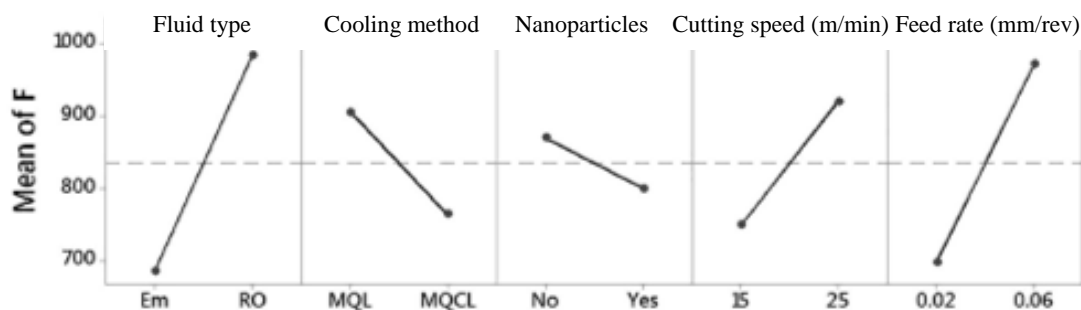
Figure 11. Effects of input variables on the drilling thrust force [Adapted from Minh Duc et al., 2020]
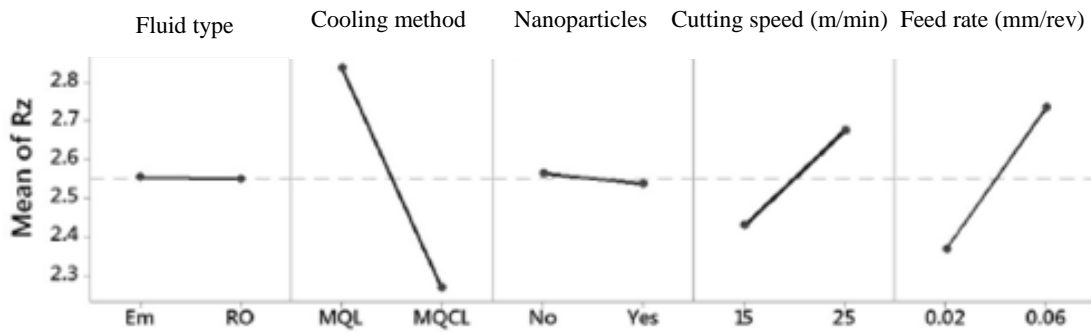
Figure 12. Effect of input variables on the surface roughness [Adapted from Minh Duc et al., 2020]

The effect of viscosity and thermal conductivity of vegetable oils in MQL for machining hard-to-cut materials was investigated by Okafor and Nwoguh (2020). Three vegetable oils, including modified high oleic soyabean oil (HOSO), refined low oleic soybean oil (LOSO), acculube LB2000 oil, and mineral oil-based emulsion (EC) were studied at 25 to 70˚C with MQL. Rheological tests and thermal conductivity tests were carried out for all the lubricants to study the shear rate and thermal conductivity change with temperature. The Brookfield DV-III rheometer was used with a spindle CP40 and a water bath, which controlled the temperature of the sample between 25 to 70˚C. For each lubricant, 0.5 ml sample was used for the test and repeated twice. Thermal conductivity tests were performed with a Thermtest TLS-100 portable thermal conductivity meter. The 100 mm needle sensor of the transient line source meter was inserted in the sample, which was placed in the water bath. The constant current source supplied heat to the sample. The dynamic viscosity was calculated from equation (1) and the shear stress-shear rate graph obtained from the tests. The viscosity of all vegetable oils decreased exponentially with the increase in temperature as shown in Figure 13.

22

$$\sigma = \mu\gamma \qquad\qquad (1)$$

Where,

σ: Shear stress of lubricant (dyne/cm^2)

μ: Dynamic viscosity of lubricant (dyne·s/cm^2)

γ: Shear rate for lubricant (s^{-1})
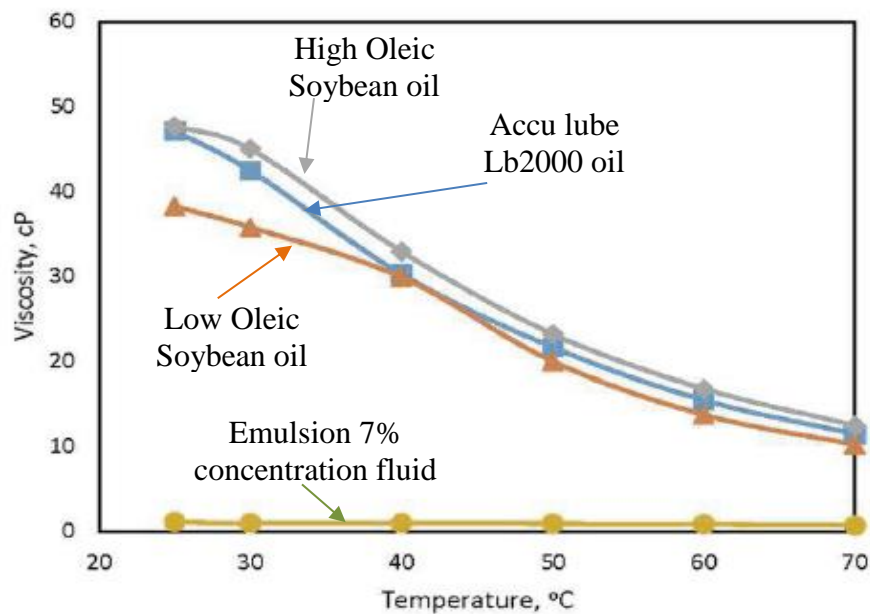
Figure 13. Viscosity against the temperature for different cutting fluids [Adapted from Okafor and Nwoguh, 2020]

Thermal conductivity was calculated based on constant current source and the slope of temperature plot against logarithm of time as shown in equation (2). Thermal conductivity of vegetable oils decreased slightly with increase in temperature as shown in Figure 14. Thermal conductivity HOSO showed better viscosity results and oxidation stability as compared to other vegetable oils and conventional EC.

23

$$k = \frac{q}{4\pi a} \tag{2}$$

Where,

k: Thermal conductivity (W/mK)

q: Heat flux (W/m^2)

a: Temperature gradient (K/m)
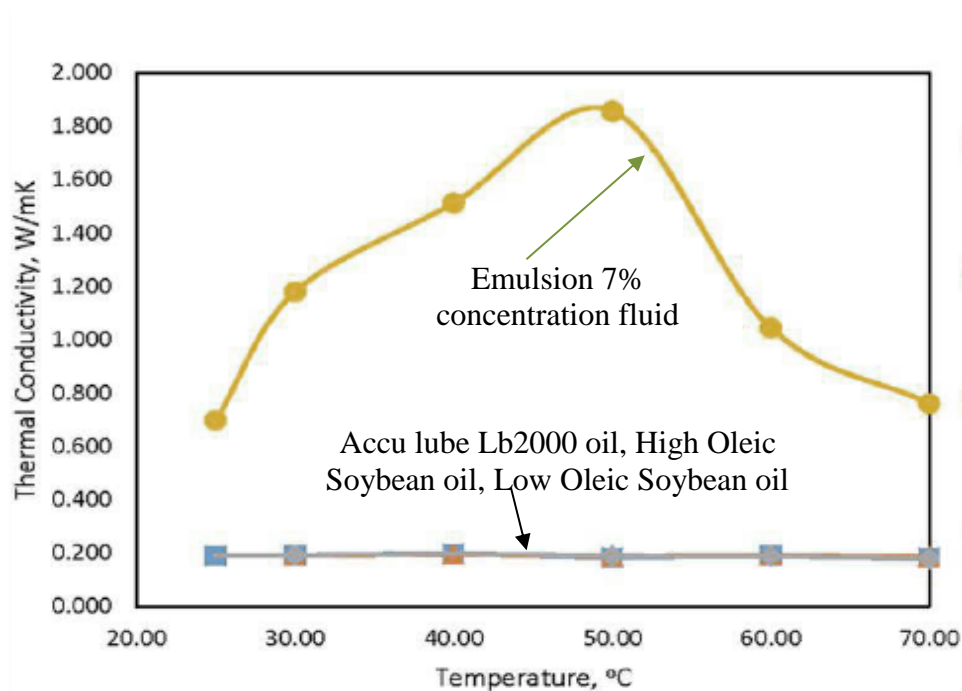
Figure 14. Thermal conductivity against the temperature for different cutting fluids [Adapted from Okafor and Nwoguh (2020)]

2.4. Internal MQL

Khan et al. (2018) simulated through-tool MQL to study the impact of input air pressure on micromist droplet sizes and investigated the effect of MQL on surface finish

24

and tool wear when micromilling selective laser melted In-718. A 3D printed ABS nozzle with 16.8 μm surface roughness R_a was used for this study. It was polished later with acetone to achieve 3.2 μm surface roughness R_a. The author included the effect of nozzle surface roughness on mist drop sizes. The HAAS OM2 CNC milling system was used for milling. Coolube 2210 EP was used as a coolant in the simulated MQL system. Input air pressure of the MQL system was varied as 275, 415, and 550 kPa. Milling parameters were kept constant as 13.6 m/min speed, 1.8 μm/tooth chip load, and 20 μm depth of cut. The flow velocity of compressed air was measured with the Kanomax Climomaster 6501 anemometer. Higher air pressure of 550 kPa generated smaller airborne droplets of about 5 μm and improved surface finish of the workpiece by about 1 μm. As compared to the smooth nozzle (3.2 μm surface roughness), a rough nozzle surface (16.8 μm surface roughness) reduced the airborne diameter of micromist droplets. The airborne diameters with rough nozzle were 9.20, 7.25 and 4.69 μm, and 11.42, 9.31, 7.60 μm with smooth nozzle at 275, 415, and 550 kPa respectively (Figure 15).
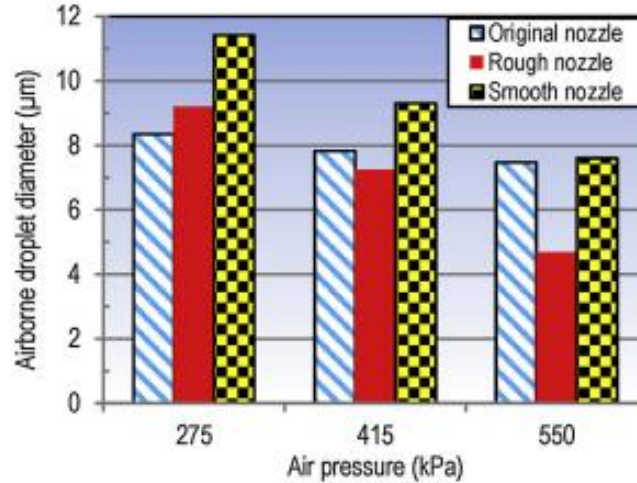
Figure 15. Effect of air pressure and nozzle surface on airborne droplet diameters in MQL [Reprinted from Khan et al., 2018]

Kao et al. (2017) studied the effect of coolant channel sizes and shapes on the mist flow in through-tool MQL drilling. Mist flow was analysed experimentally and analytically for circular and triangular coolant channels of four identical drills. Experiments were conducted on two channels with circular cross-section of radii 0.8 and 0.5 mm; other two channels had an equilateral triangle cross-section with side lengths of 2.15 and 1.35 mm. The air pressure and the oil flow rate were 5 bars and 45 mL/hr respectively. A high speed camera was used to capture the mist flow at the drill tip and an anemometer was used to measure the airspeed of the resultant micromist. The Darcy-Weisbach equation (3) was used to justify the results obtained.

$$\Delta P = f_D \frac{L}{D} \frac{\rho V^2}{2} \tag{3}$$

Where,

ΔP: Pressure drop (Pa)

f_D: Darcy friction factor (constant)

L: Length of the channel (m)

D: Hydraulic diameter of the channel (mm)

ρ: Density of the fluid (kg/m^3)

V: Mean velocity of the fluid (m/s)

Kao et al. (2017) observed that the air flow rate of the mist varied according to the coolant channel size and shape. For larger channel sizes, airspeed was higher than that of smaller channel sizes. Thus, for smaller circular channel, lubricant droplets were found to coalesce with each other as shown in Figure 16 and Figure 17. Circular channels exhibit higher airspeed of mist than those of triangular channels. In addition, lubricant accumulated more near the drill centre point for circular channels.
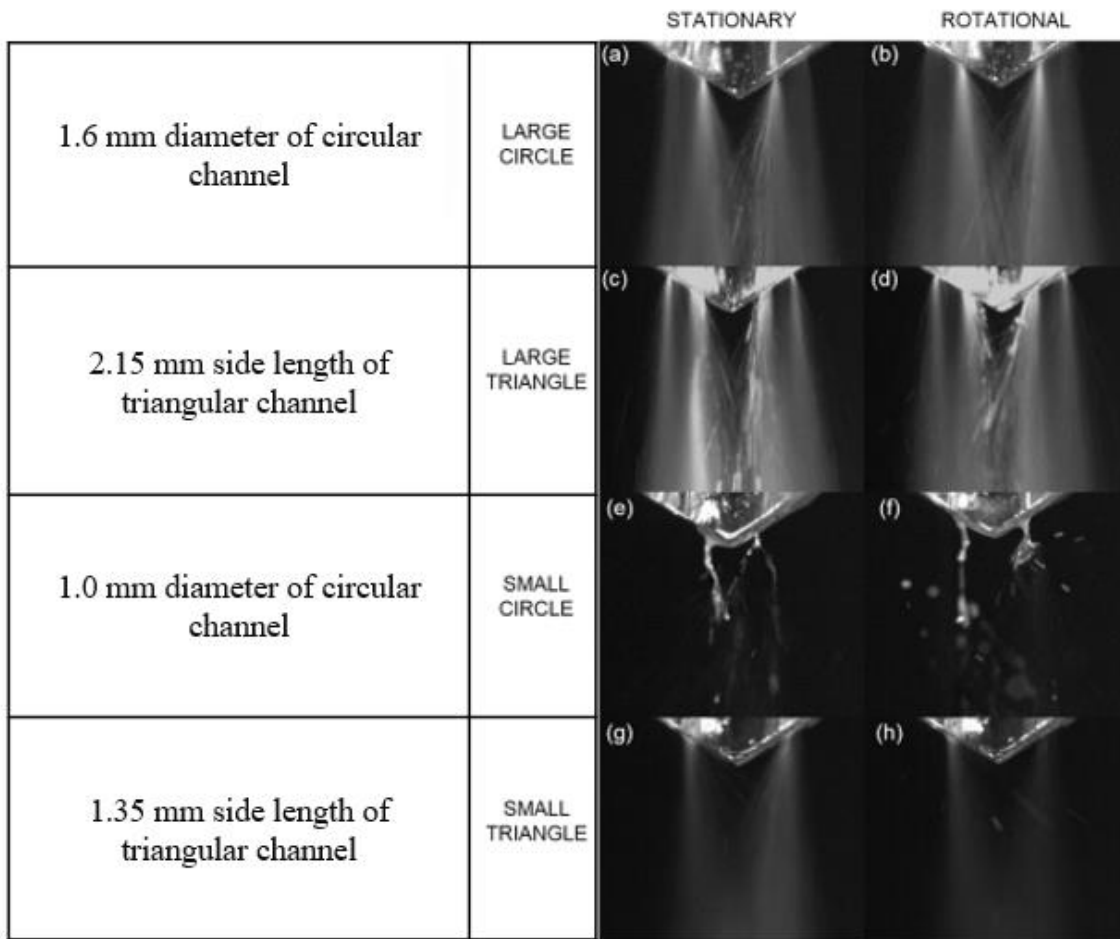
Figure 16. Mist flow for different coolant channel shapes and sizes [Adapted from Kao et al., 2017]
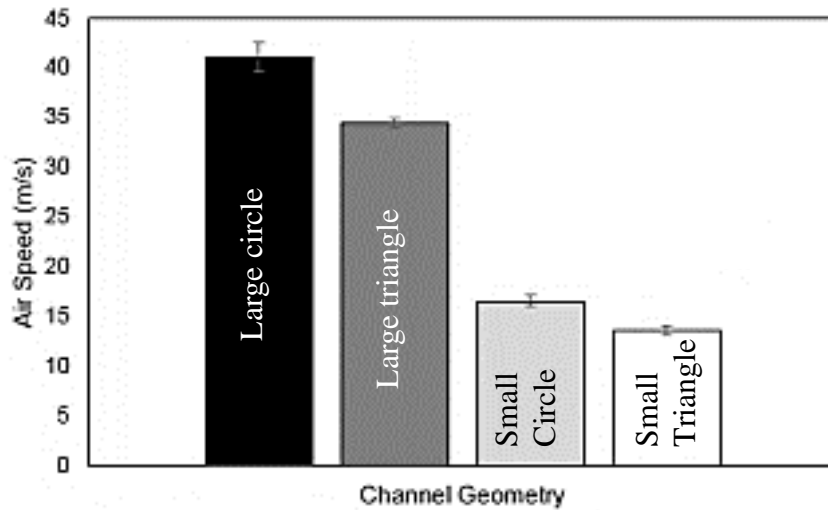
Figure 17. Airspeed comparison for varied channel sizes and shapes [Adapted from Kao et al., 2017]

Raval et al. (2019) characterized micromist distribution in 3D printed through-tool coolant drills in MQL. A Unist dual channel MQL system with a rotary union and an atomizing chamber was used. The Phantom MiroLab 310 high speed camera was used to capture the mist flow at the drill tip. Frame rate was constant at 1000 fps with a resolution of 512×512. Axial velocity component of the drill was considered negligible. Unist Coolube 2210 was used as the coolant. Oil flow rate was maintained at 40 mL/hr for all the experiments. 3D printed transparent drills of clear resin were manufactured with stereolithography technique to achieve a good surface finish and high-dimensional accuracy. Drills having circular and triangular coolant channels with varying helix angles of 0, 30, and 45 degree were used. Circular coolant channels had 1.6 mm diameter and equilateral triangular channels had 2.15 mm side length, such that the cross-sectional area of the coolant channel was same in both the cases. Numerical analysis was performed with ANSYS-FLUENT version 16.2. A single-phase simulation was carried out. 300 m/s

constant flow velocity was considered as an inlet boundary condition and a two-equation turbulence model was used for analysis. Figure 18 shows the combined results for experimental and numerical analysis. In case of 0˚ helix angle, high flow velocity region appeared at the centre of the channel. For 30˚ and 45˚ helix angle, circular channel showed high velocity region away from the chisel edge, because of the centrifugal forces generated from the fluid motion in the channel. Thus, it was concluded that the coolant channel geometry and helix angle affect the mist flow distribution. Also, high velocity regions showed low mist concentration and vice versa.
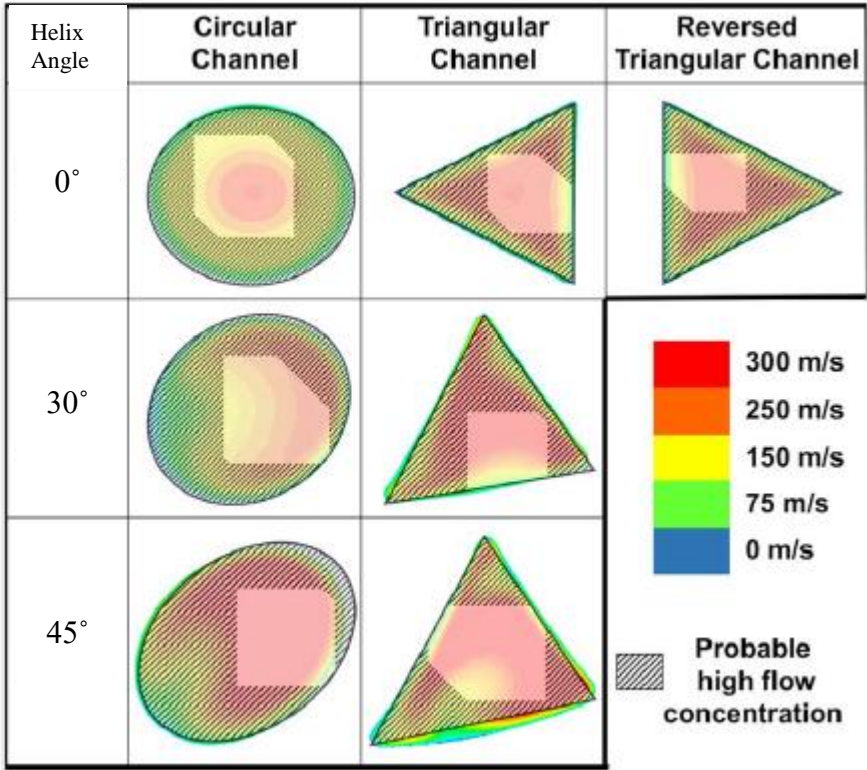
Figure 18. Superimposed experimental and numerical results [Adapted from Raval et al., 2019]

The MWF emissions produced in drilling of steel, aluminium and cast materials were investigated by the committee of experts (Fachausschuss Maschinenbau, Fertigungssysteme, Stahlbau, 2005) of German government. For this study, twist drills with two internal cooling channels were used. Pure synthetic esters of varying viscosities (Figure 19) were used as lubricants. Figure 19 shows MWF emissions captured for 15 minutes at the cutting zone and at the extraction point on a drill with the feed rate of 800 mm/min in drilling carbon steel. Lesser emissions were observed for esters having kinematic viscosity values more than 20 mm^2/s at 40˚C, than those with smaller viscosity. This study also concluded that for low emissions of aerosol in MQL, the lubricant should have at least 10 mm^2/s kinematic viscosity at 40˚C, flash point of at least 150˚C, and evaporation loss of maximum 65% at 250˚C as stipulated by the German standard DIN EN ISO 2592 (Fachausschuss Information Sheet No. 006, 2005).

Cooling lubricant emissions ;F_r = 800 mm/min , Jel drill
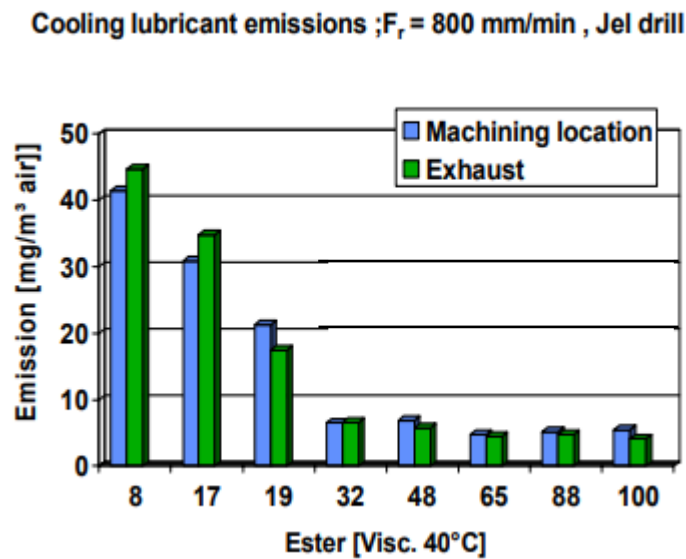
Figure 19. Aerosol and vapour emissions at the cutting location. Workpiece Ck 45k, Feed 800 mm/min, Ester lubricant [Adapted from Fachausschuss Information Sheet No. 006, 2005]

2.5. Contact angle and wettability

Contact angle between a solid and liquid interface can directly affect the wettability of the liquid. A low contact angle between a solid and liquid interface results in liquid spreading over more area on the solid surface, improving the wettability of the liquid. For proper lubrication, higher wettability is necessary.

Li et al. (2015) characterized micromist for a Unist MQL system with four lubricants, viz., Coolube 2210, 2210EP, 2300HD, and 2200. These oils were tested on 316L stainless steel, titanium, and tungsten carbide to measure contact angles (Figure 20). Input air pressure was varied from 200 to 600 kPa, and lubricant flow rate was maintained at 1.32 mL/hr. Micromist flow was captured using particle image velocimetry (PIV) and a Hi-Sense MKII CCD camera. The distance between the nozzle and the glass plate was 130 or 150 mm. The Olympus STM6 microscope was used for droplet size measurement and contact angle measurements. Airspeed of the micromist was measured using a 1 mm diameter needle probe of Kanomax Climomaster 6501 anemometer. It was concluded that at high airspeed, smaller droplets were produced at the nozzle tip (Figure 21). Furthermore, contact angle was proved to be an important factor to decide wettability of lubricants on various materials. In this study, negligible effect of gravity, no evaporation of droplets, and spherical shape of droplets were assumed. The sessile drop technique was used to calculate contact angles and projected diameter of droplets with following equations (4) and (5) (Kajaria, 2009):

$$\frac{P}{V''^{\frac{1}{3}}}(\theta) = \left[\left(\frac{24}{\pi}\right)\left(\frac{(1 - K'cos^2\theta)^{3/2}}{2 - 3cos\theta + cos^3\theta}\right)\right]^{1/3} \tag{4}$$

$$d = \left(\frac{6V'''}{\pi}\right)^{1/3}$$

(5)

Where,

P: Projected droplet diameter (mm)

V'': Volume of droplet for contact angle measurement (mm^3)

V''': Volume of droplet on glass plate by Unist system (mm^3)

θ: Contact angle (°)

d: Airborne drop diameter (mm)

K': 1 for $\theta<90°$; K'=0 for $\theta>90°$
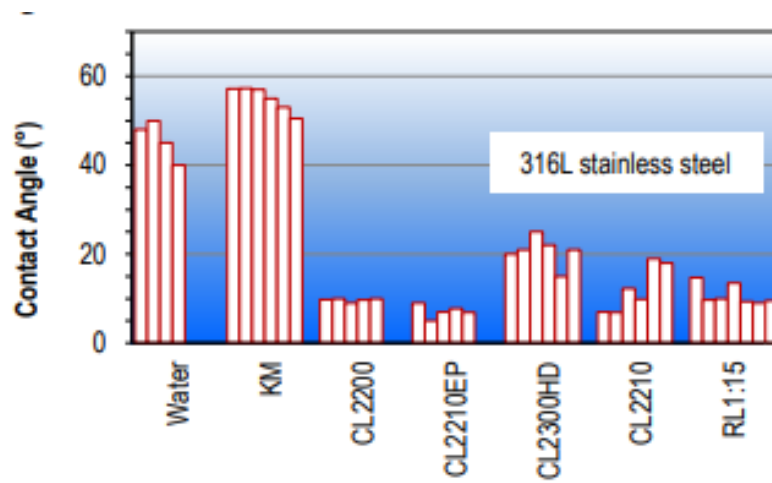
Figure 20. Contact angle of different cutting fluids on 316L stainless steel. Each bar in a group represents the repeated result for the specific fluid [Reprinted from Li et al., 2015]
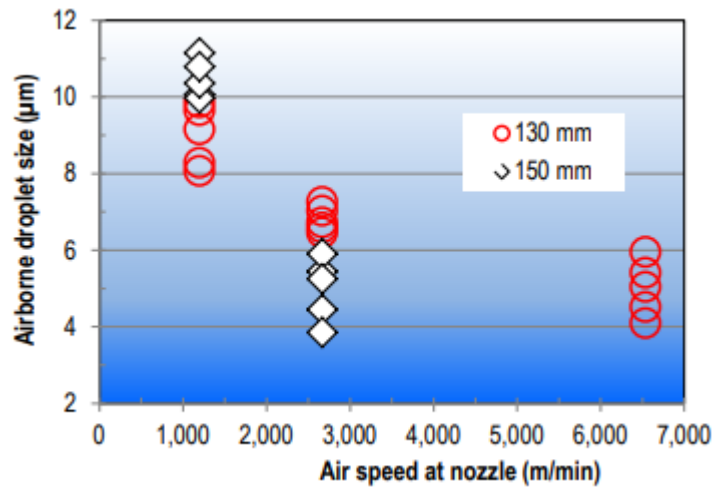
Figure 21. Effect of nozzle air speed and distance from nozzle on airborne drop size of Coolube 2210EP [Reprinted from Li et al., 2015]

Tai et al. (2011) studied nine commercial MQL fluids (Table 1), including biodegraded esters, renewable acid esters, synthetic esters, etc., and compared their thermal conductivities, wettabilities, lubricities, machinabilities and mist generation properties. It was observed that in case of MQL fluids, wettabilities and lubricities improved, however, heat removal property was relatively weak. Wettability was better for MQL fluids as those had smaller contact angles of about 8˚ to 27˚ on polished aluminium and tungsten carbide. However, the water-based fluid Trimsol with 5% concentration, showed contact angle of about 35˚ on the same polished solids (Figure 22).

Table 1. Tested MQL lubricants [Adapted from Tai et al., 2011]

Fluid	Density (g/mL)	Viscosity (cSt, 40˚C)	Flash point (˚C)
A: Biodegraded esters	0.87	8.8	200
B: Renewable acid esters	0.93	8.9	214
C: Naturally derived synthetic	0.90	10.0	182
D: Vegetable based	0.93	10.0	204
E: Vegetable based + EP	0.89	10.0	204
F: Biodegraded esters	0.93	28.0	280
G: Naturally occurring fatty oils	0.91	40.0	231
H: Synthetic ester	0.93	52.0	228
I: Vegetable based + EP	0.94	69.0	196
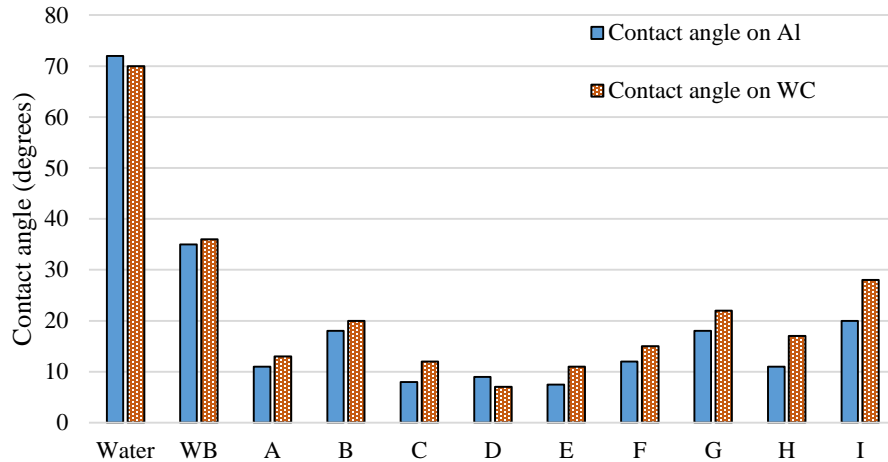
Figure 22. Contact angle measurement of selected MQL fluids [Adapted from Tai et al., 2011]

2.6. Machining with MQL

Kovvuri et al. (2015) studied BUE formation in micromilling of stainless steel. Micromilling was performed with the Haas OM2 CNC milling machine with air spindle bearing; lubricant Coolube 2210EP oil was delivered with Unist MQL system. Tools of diameters 100 to 400 μm were used for micromilling, at cutting speed of 10-60 m/min and chip load of 0.05-1 μm/flute. The input air pressure was kept constant at 400 kPa and oil consumption rate at 1.32 mL/hr. BUE on the workpiece and the tool were studied by scanning electron microscopy and energy dispersive spectroscopy. BUE density was studied with optical microscopy or interferometry. BUE density was quantified as the number of BUE per mm^2 area. Image Pro software was used to count the number of BUEs. It was concluded that BUE density and surface finish increased with decrease in cutting

speed as shown in Figure 23 and Figure 24. BUE density was higher for down milling as compared to up milling cycle, because of the position of nozzle of the MQL system. The mist from the nozzle was lubricating one side of the tool effectively in the up milling cycles. Hence, the reasons for BUE formation were improper lubrication and high temperature at the tool/workpiece interface.
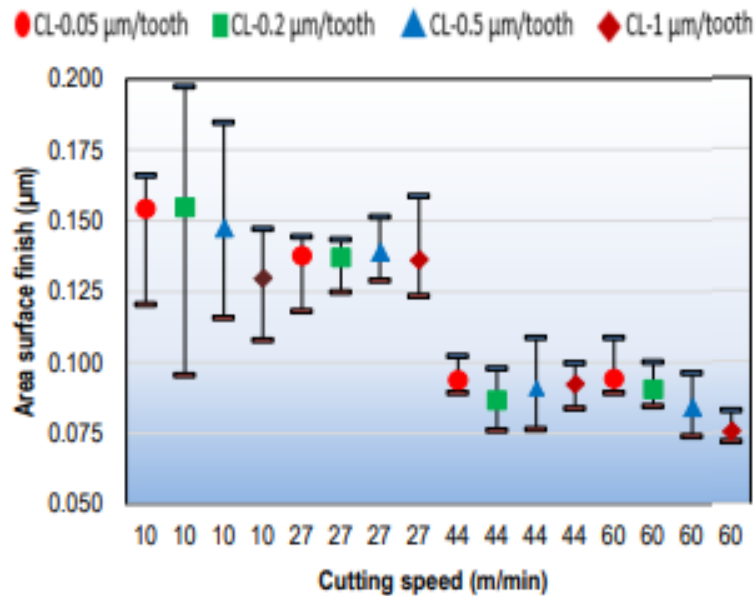
**Figure 23. Effect of cutting speed and chip load on area surfacae roughness S_a.
Each range plot shows maximum, minimum, average of 15 measurements
[Reprinted from Kovvuri et al., 2015]**
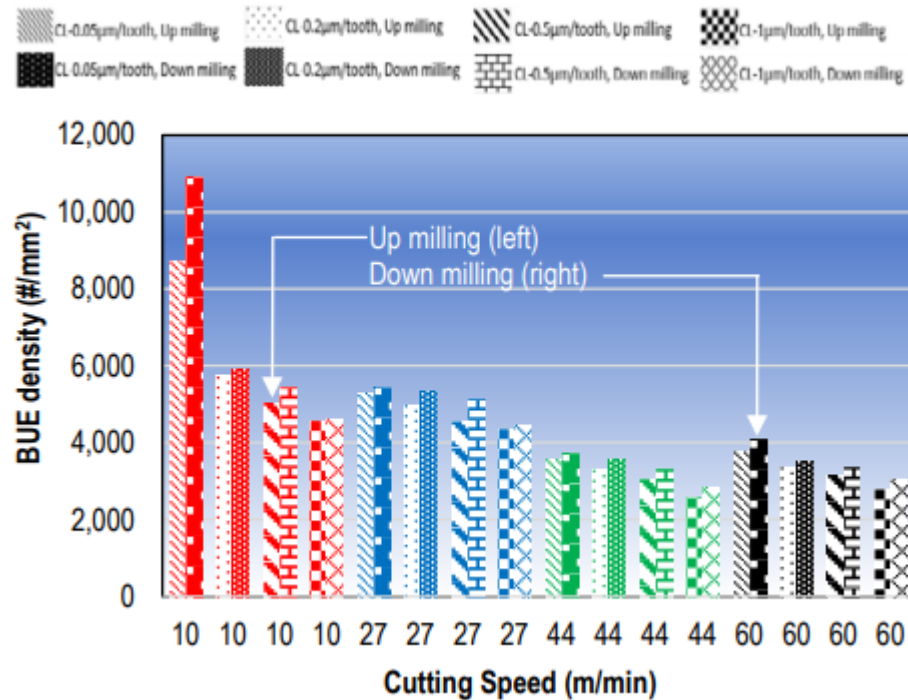
Figure 24. Effect of cutting speed and chip load on BUE density. Average of 20 samples per slot [Reprinted from Kovvuri et al., 2015]

The study by Braga et al. (2002) investigated the performance uncoated and diamond coated carbide drills in the drilling of A356 aluminium-silicon alloys using MQL and flood of soluble oil (FSO). Drilling was performed with a CNC machine with 22 kW power and 12,000 rpm maximum rotation speed. Uncoated K10 carbide drill and diamond coated carbide drills were used. The average diameters of K10 carbide drills and diamond drills were 9.986 and 9.992 mm respectively. The MQL system used had mineral oil flow rate as 10 mL/hr, 72 m^3/h air flow and 450 kPa input air pressure. Flood cooling setup used soluble oil with concentration of 1 part as oil for 25 parts of water and 2.4 m^3/h oil flow rate. The cutting speed was 300 m/min and the feed was 0.1 or 0.2 mm per revolution. To measure the feed force and torque exerted, a dynamometer was used with an amplifier

and an A/D board. Sampling time was kept constant as 2 seconds. With the MQL system, flank wear increase rate was constant, but it showed a greater value than that of flood cooling case as shown in Figure 25. Drilled hole diameters were close to the actual drill diameter, when uncoated drill was used, irrespective of cooling system used (Figure 26). However, with MQL system, diamond coated tools showed better results for hole diameters than those with the flood cooling. In addition, this study also showed that the chip stuck to the tool tip increased the feed force in case of the MQL and the diamond coated tool. From Figure 27, it can be concluded that with MQL and diamond coated tool setup, drilled hole roundness dropped significantly, unlike K10 tools. With feed as 0.2 mm per revolution, roundness values and average hole diameters for drilled holes were higher than those obtained with 0.1 mm per revolution feed.
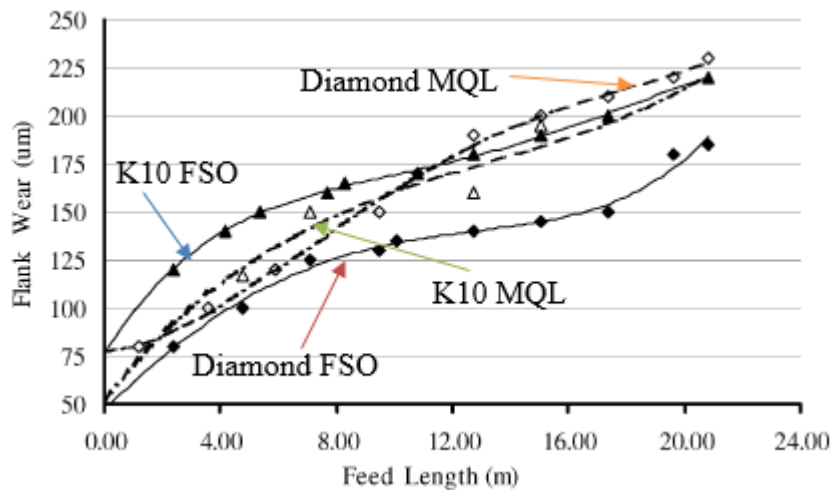
Figure 25. Flank wear against feed length for MQL and flood cooling systems and tool materials. 300 m/min cutting speed, 9950 rpm spindle speed, 0.1 mm/rev feed, 995 mm/min feed rate, 10 mm tool diameter [Adapted from Braga et al., 2002]
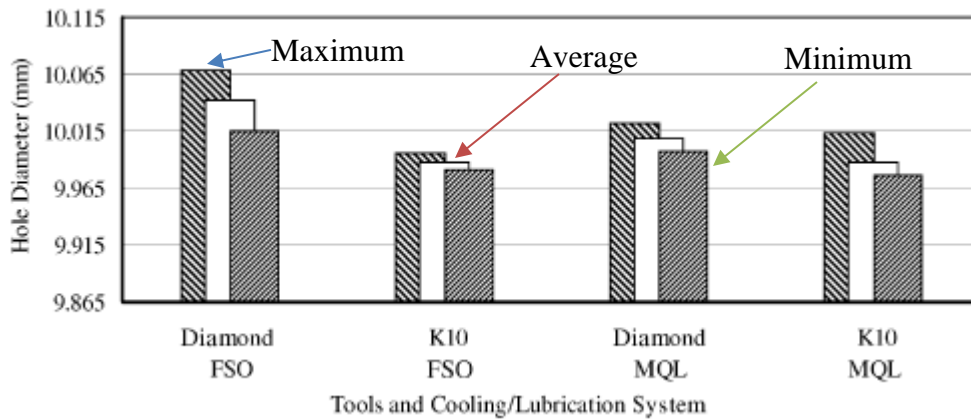
Figure 26. Average diameter and its dispersion for both cooling systems and tool materials. 300 m/min cutting speed, 9950 rpm spindle speed, 0.1 mm/rev feed, 995 mm/min feed rate, 10 mm tool diameter [Adapted from Braga et al., 2002]
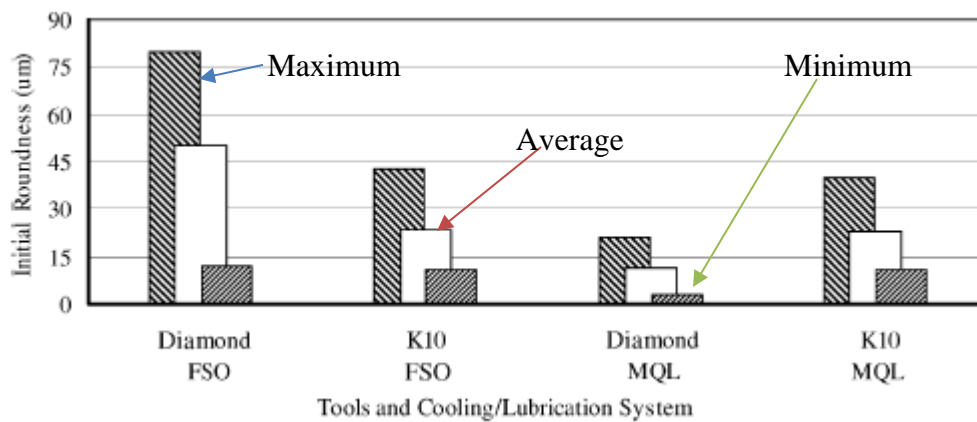
Figure 27. Roundness and its dispersion for both cooling systems and tool materials. 300 m/min cutting speed, 9950 rpm spindle speed, 0.1 mm/rev feed, 995 mm/min feed rate, 10 mm tool diameter [Adapted from Braga et al., 2002]

Ford Motor Company used MQL system for machining intricate transmission components. The effect of MQL deep hole drilling on steel and cast iron crankshafts was studied (Figure 28). The length to diameter ratio of these crankshafts was about 20. It was observed that the feed rate for solid carbide twist drills with MQL application can be raised

40

over 660 mm/min, whereas with traditional cooling method it was about 125 mm/min (Furness et al., 2006).
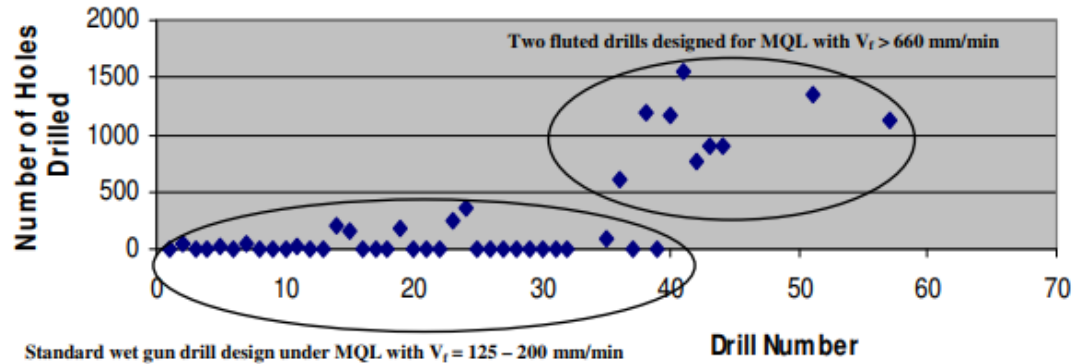
**Figure 28. Comparison of standard and MQL drill performance.
Drill length/diameter= 20 [Adapted from Furness et al., 2006]**

Sun et al. (2006) investigated the effects of dry cutting, flood cooling, and MQL on tool life and cutting force in milling of Ti-6Al-4V alloy (Figure 29). The insert used for the carbide tool was Sumitomo CHE 2000 type of material H1 and edge shape A. For flood cooling, a fully synthetic water soluble coolant EcoCool S-CO5 was used with volumetric concentration 1:20. The Ebara atomizer along with the vegetable oil was used to generate fine oil mist in MQL. The authors measured the tool life based on the machining time and the material removed in the machining process. Using 0.5 mm axial depth of cut, 2 mm radial depth of cut, 0.1 mm/tooth feed, tool life was measured at different cutting speeds from 40 m/min to 140 m/min. The longest tool life of about 800 min was observed with MQL at cutting speed of 40 m/min, whereas, the shortest tool life of about 6 min was obtained with flood cooling at cutting speed of 140 m/min. Furthermore, the cutting force components in horizontal, normal and vertical direction,

measured with a Kistler quantz 3-component dynamometer (Type 9253A), were compared for 0.12 mm/tooth and 0.05 mm/tooth chip load (feed). For both the feeds, cutting force components for MQL were about 50% to 80% less than those in dry cutting. In case of flood cooling, cutting forces were at most 30% less as compared to dry cutting.
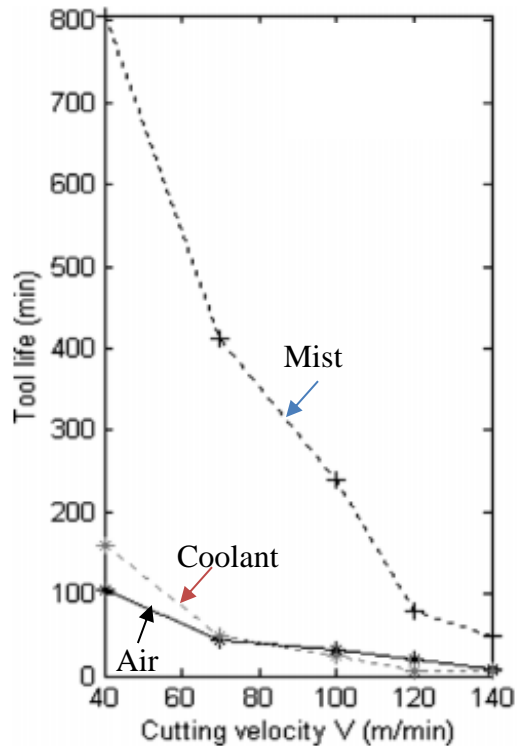
Figure 29. Effect of coolant type on tool life in milling Ti6Al4V [Adapted from Sun et al., 2006]

Barnes and Pashby (2000) studied the effect of dry cooling, conventional cooling and through-tool cooling methods when drilling aluminium/SiC metal matrix composite. Vertical machining centre was used for drilling tests. TiN coated K10 solid carbide drills with 8 mm diameter were used. Coolant was supplied at a pressure of 450 kPa. The cutting speed 30 m/min and the feed rate 0.15 mm/rev were kept constant. The cutting forces were

measured with a Kistler 9271A dynamometer. For measuring the drill wear, reference points produced by electrical discharge machining (EDM) were used. The drill wear was measured for 100 holes with respect to those reference points. Drill wear, cutting forces, burr height, drilled hole diameter, and surface roughness of drilled holes were compared in all three cases. It was observed in case of dry and conventional cooling, that highly strained BUE flowed over wear lands, unlike through-tool cooling method. Figure 30 shows the trends of thrust forces and burr height with different cooling methods. The thrust forces generated by through-tool cooled drill was on an average 74% less than that of dry and conventional cooling method. A 25% and 38% reduction was observed in burr height produced by through-tool cooling, as compared to conventional cooling and dry cooling respectively. Hole diameters produced by dry and conventional methods was larger than expected, i.e. more than 8 mm. This could be because BUEs were able to act as the extended portions of cutting edges. Average surface roughness value for dry and conventional methods was about 0.12 µm and only 0.09 µm for through-tool lubrication.
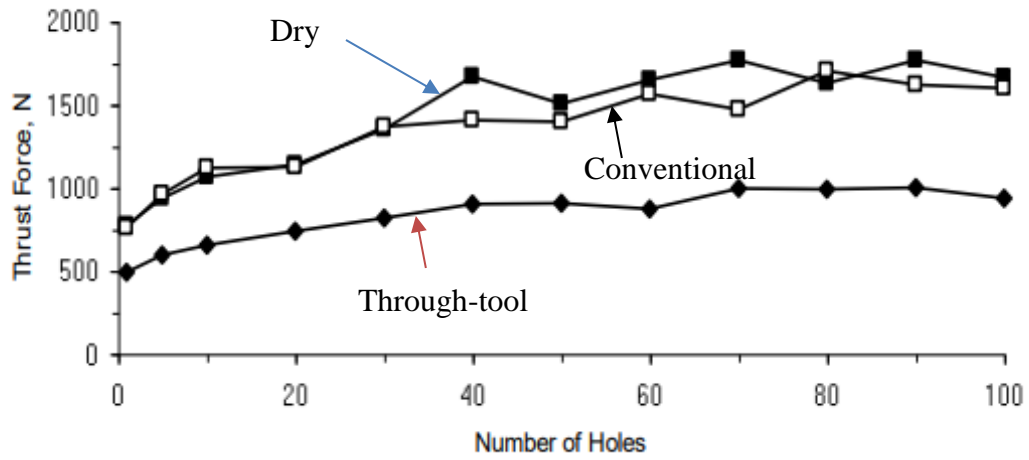
(a)
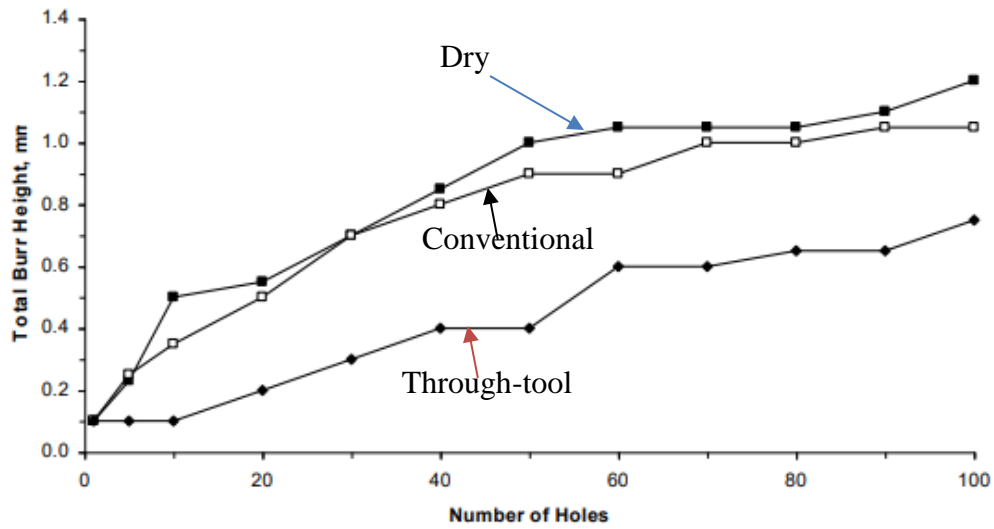
(b)

Figure 30. Variation in (a) thrust force (b) burr height, with the number of holes produced [Adapted from Barnes and Pashby, 2000]

Tai et al. (2012) studied the effect of thermal distortion of the workpiece in deep-hole drilling with MQL. The results were compared with finite element analysis (FEA) and experimental study on an aluminium 6061-T6 workpiece. For FEA, drill diameter 10 mm, depth of holes 200 mm was considered. The author proposed a heat carrier model

with 3-D FEA. In FEA analysis, two types of heat fluxes, viz., hole wall surface and hole bottom surface were taken into account. Hole bottom surface heat flux was assumed to be steady with constant feed rate and speed. Whereas, the heat flux associated with the hole wall surface was considered to be dependent on the depth of the drill and resultant chip removal. These heat fluxes were calculated based on inverse heat transfer model. Temperature distribution in workpiece when drilling a deep-hole was predicted using a 3-D FEA model. To avoid failure of FEA model, the mesh was developed with a gap of about 1% of drill diameter between the heat carrier and the surface of the deep-hole. The conductance value for these gaps were set to 10^6 W/m^{2}K in ABAQUS to allow the heat transfer. A thermal-elastic FEA was used to predict the temperature distribution of the workpiece. In actual experimental setup, Fadal vertical machining center (Model VMC 4020), 0.2 mm/rev feed rate, and 2100 rpm spindle speed were used. A 220 mm long, 10 mm diameter solid carbide drill with through-tool holes was utilized. The input air pressure of 500 kPa and oil flow rate 60 mL/hr were set for the MQL system with Milacron CIMFREE fluid. Five E thermocouples OMEGA Model 5TC-TT-E-36-72 were installed in the Al 6061-T6 workpiece at a distance of 3.4 mm from the hole wall surface and 30 mm from the consecutive thermocouple(s). Total drilling time was 21.7 s and sampling rate for temperatures was 10 Hz. A 50.8×152×152 mm aluminium block with four 152 mm deep sequentially drilled holes was used to verify the thermal distortion results obtained from the FEA model. The positions of four reference holes were measured with a dial indicator of 5 μm resolution. Three thermocouples were also installed to validate

45

the temperature distribution from FEA. The experimental distortion value obtained was 61 μm and 51 μm from the FEA model.

Bono and Ni (2001) studied the effects of thermal distortions of the drill and the workpiece on the quality of drilled holes. A developed 3D FEA model predicted the thermal distortion of the drill and the workpiece. The model anticipated that the thermal expansion of the drill can significantly affect the drilled hole size and depth. Mori Seiki TV-30 CNC drilling machine was used for drilling in actual experimentation. HSS drill with 125˚ included angle and 39˚ helix angle was used to drill 25 mm deep and 9.92 mm diameter holes in A319. A Kistler piezoelectric dynamometer was used to measure the thrust force and toque during drilling. A type K thermocouple was installed in the drill with 127 μm wire diameter. 3000 to 700 rpm speed and 127 to 381 μm/rev feed was provided. It was concluded that the resultant heat flow into the drill and the workpiece led to oversized holes and increase in depth. It was observed that the hole diameter at the top of the drilled hole is smaller than than that at the bottom (Figure 31). Thermal distortions resulted in deviations up to 26 μm for hole diameter values (Figure 32).
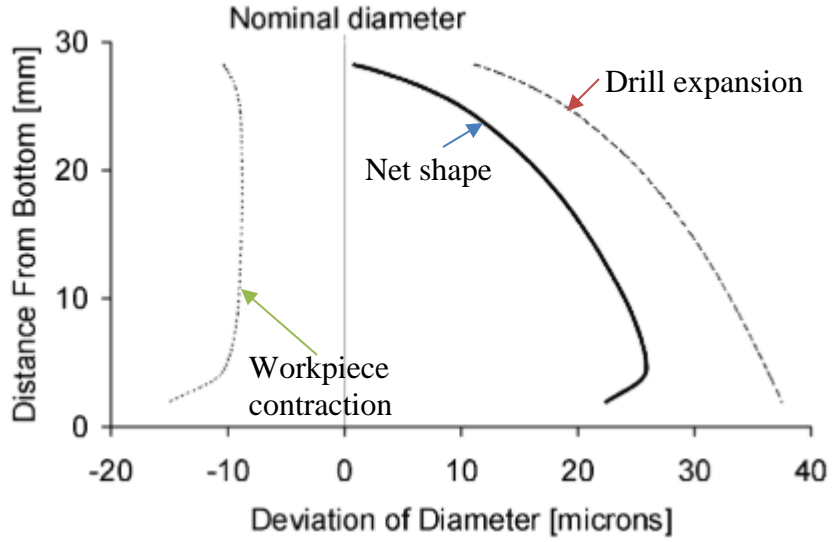
Figure 31. Estimated shape of the drilled hole at 7000 rpm speed and 381 μm/rev feed [Adapted from Bono and Ni, 2001]
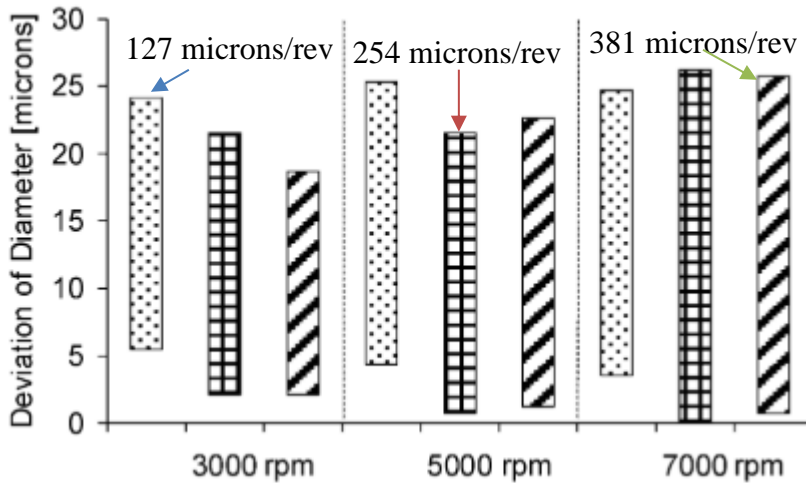
Figure 32. Diametral deviations predicted from the measured drilling forces at different feed (Actual diameter of the drill at room temperature: 9.922 mm) [Adapted from Bono and Ni, 2001]

K-means clustering method is an unsupervised learning method for statistical analysis of the data. Some datasets with undefined categories or groups cannot be

47

successfully analyzed with supervised learning methods, such as linear or logistic regression. However, K-means clustering can form different groups or clusters in the given data based on similar features or a common baseline metric for datapoints.

According to James et al. (2017), K-means clustering method assigns each data point to exactly one cluster. Initially, it randomly assigns each data point to a cluster. Then, it iterates until there is no change in the clusters formed and the centroid of each cluster is determined (Figure 33). This technique minimizes within-cluster variation, i.e., the amount by which observations within a cluster differ from each other. Commonly, it minimizes the distance between the data points (equation (6)), which is defined by:

$$\sum_{k=1}^{K} \frac{1}{|C_k|} \sum_{i,i' \in C_k} \sum_{j=1}^{p} (x_{ij} - x_{i'j})^2 \tag{6}$$

Where,

K: total number of clusters

C_k: k[th] cluster

$/C_k/$: number of data samples in k[th] cluster

x_{ij}: observation in the cluster

$x_{i'j}$: observation in the cluster other than x_{ij}

The within-cluster-sum of squares is the ratio of total pairwise squared distances in a cluster to the number of observations in that cluster. After the final iteration, each data point gets assigned to the cluster with the nearest centroid, with respect to the Euclidean distance. This method is used with airborne diameter data, as it can find the local mean of the cluster instead of global mean, i.e., the average value of the whole dataset.
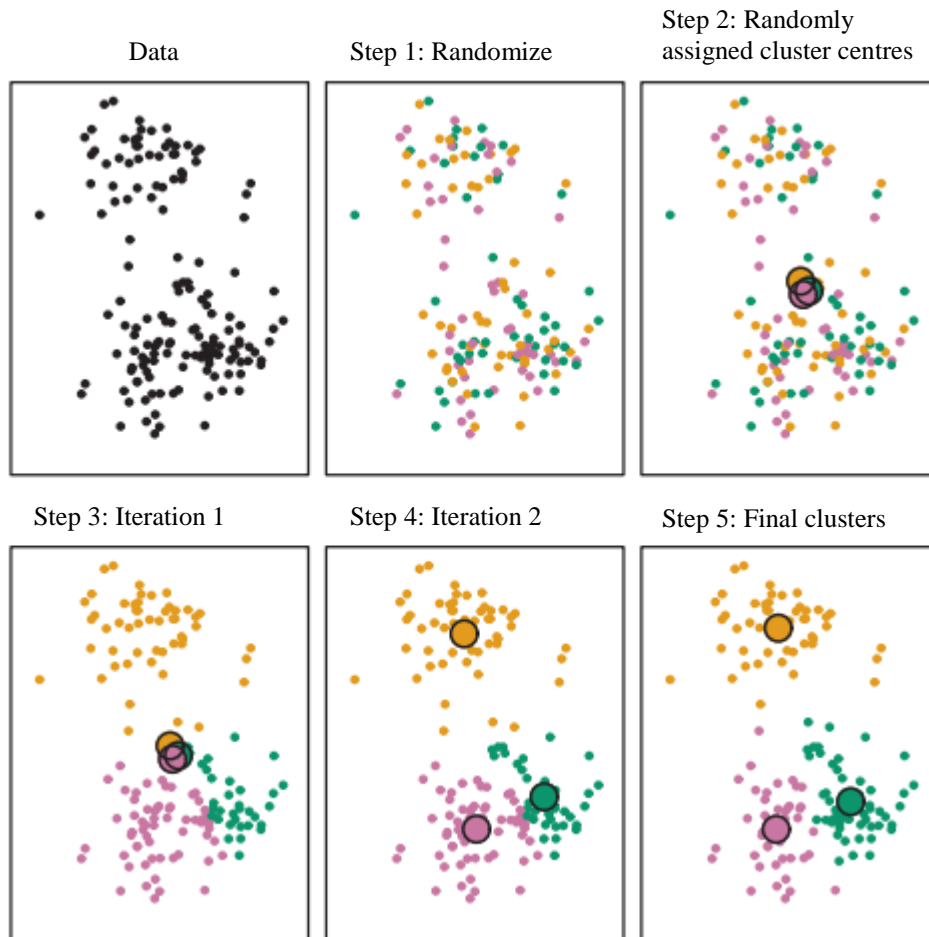
Figure 33. K-means clustering algorithm [Adapted from James et al., 2017]

In this method, the number of clusters 'K' is a crucial parameter. To determine appropriate value of 'K', elbow method was implemented in software RStudio. Elbow method plots the percentage of variance in a dataset as a function of number of clusters, i.e., K (Figure 33). Thus, the suitable value of K is such that, adding a greater number of clusters to K does not affect the percentage of variance significantly. Elbow method serves

as a prerequisite to the K-means clustering method to identify the number of clusters (Marutho et al., 2018).

Many researchers have investigated the topic of MQL, mostly focusing on external MQL systems. However, limited literature has been published for internal MQL systems. This study uses twist drills with twin internal channels for MQL, characterizes and compares resultant droplets for two different lubricants, inspects the droplet formation and flow from drill tip, and studies the effect of the internal MQL, flood cooling, and dry machining on drilling of A380 cast aluminium.

CHAPTER 3

EXPERIMENTS

Three tests were performed to evaluate the effectiveness of through-tool MQL. These include

a.   Droplet characterization for two different lubricants with two different drill sizes

b.   High speed imaging technique to study droplet formation and flow

c.   Drilling tests to study the effect of internal MQL.

3.1. Droplet characterization
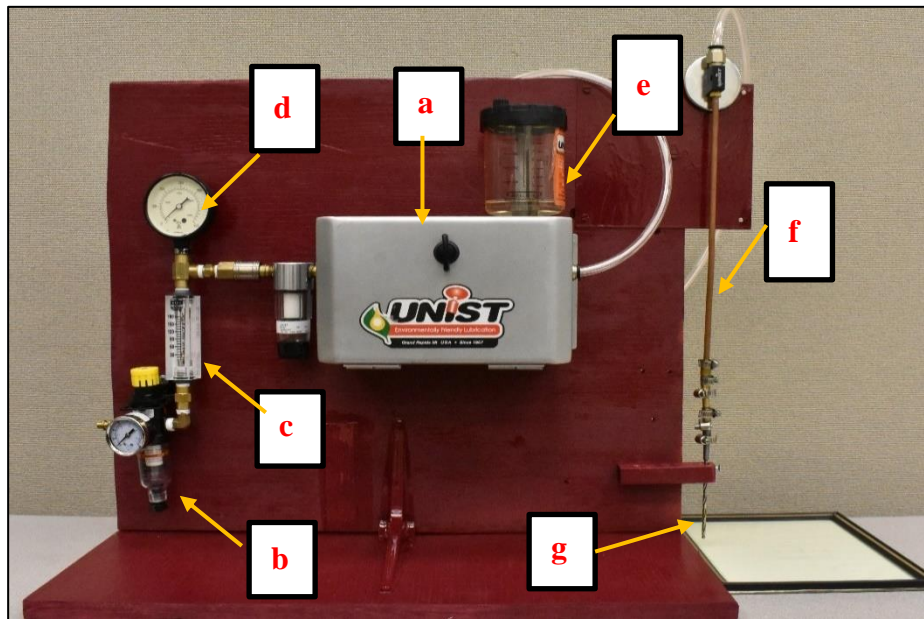
Figure 34. Experimental setup for droplet characterization.
Where, a: Unist Coolubricator system, b: air filter/regulator, c: air flow meter, d: pressure gage, e: lubricant reservoir, f: copper tube, and g: drill with dual internal coolant channels

Figure 34 shows the experimental setup for droplet characterization. Experiments were performed on a Unist Coolubricator system (a). This system uses compressed air to form aerosol with the lubricant fed from the inbuilt reservoir of the system. Air supplied

through the air hose connection was attached to the air filter/regulator unit (b). Air pressure was thus adjusted with the regulator knob. In order to monitor the volume of air flowing through the system, an air flow meter (c) was attached to the air regulator unit. A pressure gauge (d) was connected to the air flow meter to ensure that there was no leak in the system. The Unist coolubricator had an air filter attached to it to avoid contaminates. Thus, filtered air entered the Unist system. The oil reservoir (e) of the system supplied the lubricant to the system. This dual channel MQL system with semi-rigid copper nozzle (f) was attached to the through-tool coolant drill (g) of diameter 4 or 8 mm with a brass hose splicer and vinyl tubing as shown in Figure 35. For 10 mm drill, vinyl tubing and a aluminium hose splicer were used. The aluminium hose splicer was fabricated on a lathe. A brass hose splicer with inside diameter (ID) of 6.35 mm and outside diameter (OD) of 7.23 mm was used for 4 mm drill. One end of this splicer was turned down on a lathe, to achieve an OD of 5.65 mm. A vinyl tubing with ID 6.35 mm, OD 9.52 mm was used as a joiner for the copper nozzle and hose splicer. Other vinyl tubing with ID 4.76 mm, OD 7.93 mm was connected to the hose splicer and shank of the drill. All connections were secured by appropriate steel hose clamps to prevent leakage. To minimize the effect of chemical reaction between lubricant and vinyl tubing due to prolonged contact, vinyl tubing was replaced frequently.
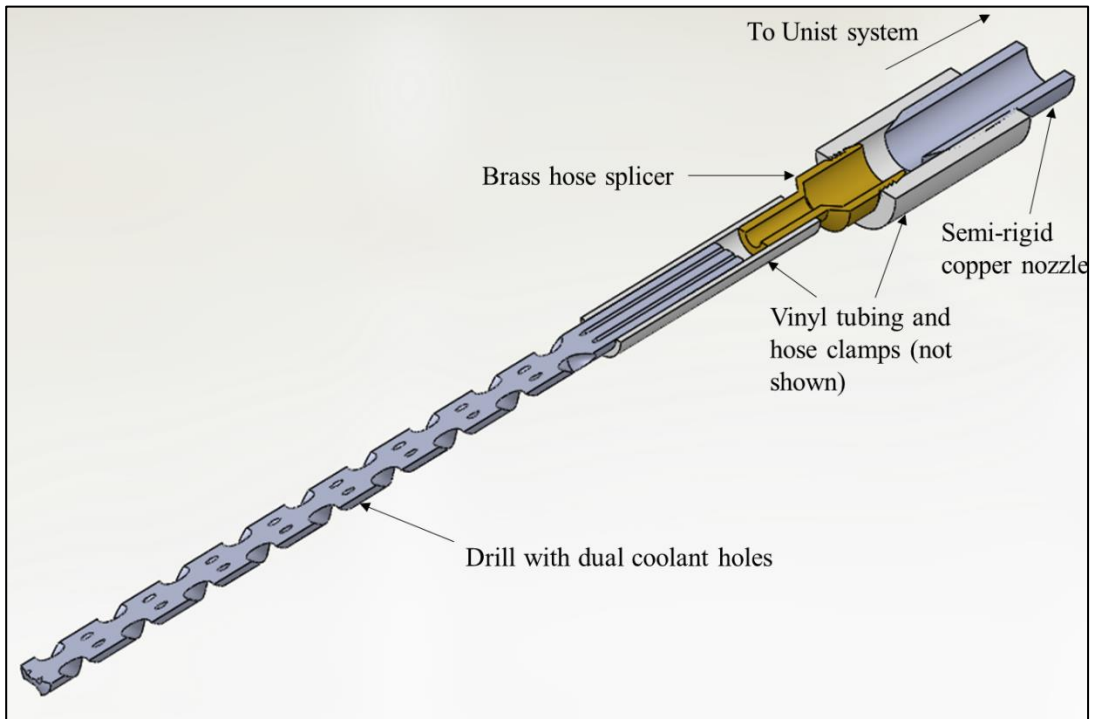
Figure 35. Schematic representation of the assembly in experimental setup

One set of experiments was performed for the characterization of resulting lubricant droplets from 4 and 8 mm twist drills (Figure 36). The effect of varying air pressure on the airborne diameter of lubricant droplets was studied.

Figure 36. Drill (8 mm diameter) with dual coolant holes

3.1.1. Equipment and software

1. Adobe Photoshop version 6.0

2. Air filter/regulator unit: Maximum pressure 1034 kPa, maximum temperature 125°C, 34 m^3/hr (20 scfm)

3. Air flow meter 7510212A11: Maximum pressure 689 kPa (100 psi), maximum temperature limit 37°C, 1.96 m^3/hr (70 scfh) air

4. Autoclavable Pipettor micropipette

5. Hose splicer:

    - Brass: ID 6.35 mm, OD 7.23 mm

    - Aluminium: ID 5.35 mm, OD 6.35 mm

6. Glass cleaner

7. Heat activated wax

8. ImageJ version 1.52a

9. Isopropyl alcohol

10. Lubricants

    - Coolube 2210 Al

    - Castrol Hyspray A 1536

11. NCSS version 20.0.1

12. Olympus STM6 microscope

13. Pressure gauge: Marsh Instrument Company, Range 0-4000 kPa

14. PVC Air hose: Maximum pressure limit 2068 kPa (300 psi), -28°C to 62°C

15. RStudio version 1.1.463

16.   Solid carbide twist drills (4, 8, 10 mm diameter) with through-holes [Table 2]

17.   Unist Coolubricator System with semi-rigid copper nozzle

18.   Vinyl tubing:

- ID 4.76 mm, OD 7.93 mm

- ID 6.35 mm, OD 9.52 mm

- ID 9.52 mm, OD 12.7 mm

19.   Waage Electric Stove (Model D8TFR-15-1): 115 AC, 1 Phase, 1250 Watts, 38-

538˚ C

Table 2. Specifications of tested drills

Specifications	Small drill [Star SU]	Medium drill [Sharon-Cutwell]	Large drill [Kennametal]
Specified drill diameter (mm)	4	8	10
Actual drill diameter (mm)	3.889	7.995	9.957
No. of flutes	2	2	2
Circular coolant channel diameter (mm)	0.7	1	1.5
Distance between coolant holes (mm)	2.4	3.8	4.9
Helix angle (˚)	20	15	30
Included angle (˚)	140	135	140
Total length (mm)	129.6	80	103
Flute length (mm)	89.6	37	61

3.1.2. Experimental procedure for droplet characterization

3.1.2.1. Contact angle

For calculating contact angle of Coolube and Castrol oil, sessile drop technique was used. A small volume of oil is deposited in this technique to minimize the gravitational effects on the measurement. The contact angle measurements for both oils on the glass plate were used to calculate the airborne diameters of mist droplets, whereas, the contact angles measured on the polished A380 block were used to compare the wettability of both oils on die cast A380 aluminium. Following procedure was followed to calculate the contact angles for both oils:

1. Droplets of Coolube and Castrol oil with 0.1 µL volume were deposited on a clean glass plate and polished A380 cast aluminium block using an Autoclavable Pipettor micropipette. To deposit accurate volume of oil on the glass plate or the block, and to avoid excessive deposition of oil, the tip of the micropipette was slid around the container before the deposition of oil on the plate or A380 block.

2. The glass slide or A380 block with deposited droplet was immediately kept under the microscope to minimize evaporation and change in size of the droplet.

3. Projected diameters of these droplets were determined with the caliper function of the software associated with the Olympus microscope.

4. At least 2 measurements were taken for each droplet with caliper function.

5. The glass slide and the block were cleaned with acetone after each measurement and the process was repeated again for 15 measurements of each lubricant.

3.1.2.2. Airborne diameter

Experiments were performed for droplet collection on a glass slide. To minimize evaporation and changes in shapes of the droplets, experimental setup was kept near the Olympus STM6 microscope.

Assumptions:

- A stationary drill was used assuming the negligible effect of drill rotation.

- Experiments were performed in still air, assuming negligible evaporation of airborne droplets.

- There was no leak in the system.

Fixed parameters:

- Air flow rate as 0.566 m^3/hr (20 scfh) for 4 mm drill, 1.7 m^3/hr (60 scfh) for 8 mm drill for all experiments

- Number of fluid strokes per min: 40 strokes/min

- Volume of fluid delivered per stroke: 0.016 mL

- Lubricant flow rate per hour: 38.4 mL/hr

- Distance between the drill tip and glass slide: 355 mm

- Time for collecting the resulting droplets: about 2 sec

Variables:

- Input air pressure: 413 kPa (60 psi, 4.13 bar), 551 kPa (80 psi, 5.51 bar) and 689 kPa (100 psi, 6.89 bar)

- Drill sizes: 4 mm, 8 mm

- Lubricants: Listed in Table 3

Table 3. Characteristics of lubricants

Properties	Coolube 2210Al	Castrol Hyspray A 1536
Kinematic viscosity at 40º C (mm²/s)	14.5	28
Flashpoint (ºC)	93	180
Density (kg/l)	0.82-0.92 at 60ºC	0.838 at 20ºC
Thermal conductivity (W/mK)	Not available	0.1593 at 40˚C
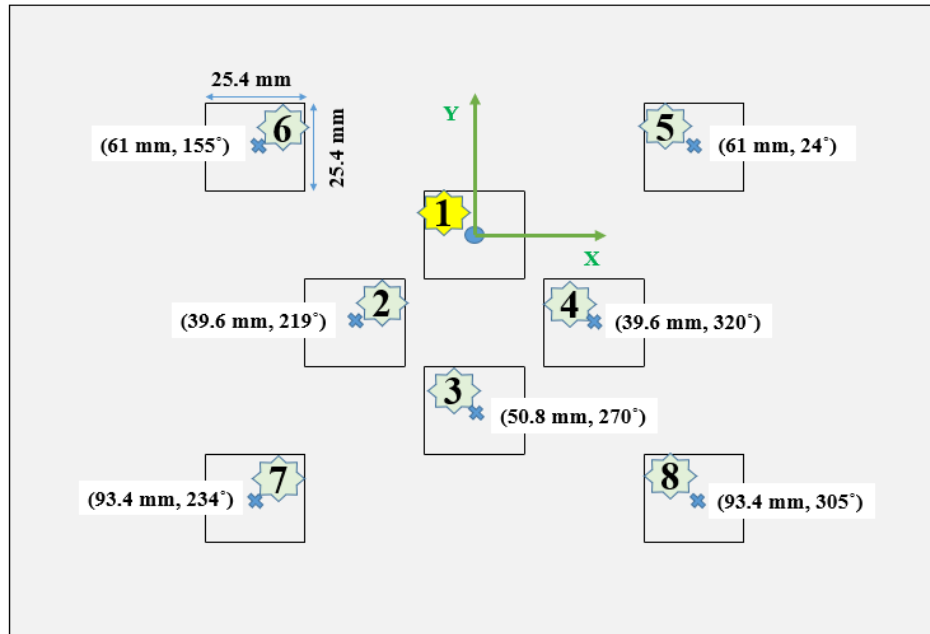
Figure 37. Polar coordinate representation of sections 1-8 on the glass slide with respect to the drill position. The origin is at the centre of the drill projection.

The following steps were followed for droplet collection:

1) Droplets resulting from the drill were collected on a glass plate of size 236 mm × 182 mm (Figure 37). The large sized glass plate was chosen to incorporate the spread of the micromist droplets.

2) Drill location was maintained at the center of location 1 with the help of a laser pointer. By holding the laser pointer close to the periphery of the drill, its position was maintained at the center of location one on the glass plate.

3) The distance between the glass plate and tip of the drill was maintained 355 mm.

4) The glass plate was cleaned with glass cleaner and acetone before each experiment.

5) Initially, a paper diaphragm was used to obstruct droplets and prevent collection of droplets for 15 seconds until system stability was achieved.

59

6) Droplets were collected on the glass plate for a duration of 2 seconds and the flow of mist was blocked again with the paper diaphragm before turning off the system.

7) Images of deposited droplets were captured using the 1.25X objective lens of Olympus STM6 microscope. There were 8 different locations identified on the glass slide to collect droplets. For each location, 5 random images within an area of 25 mm $\times$ 25 mm were captured. Figure 37 shows the glass plate with different locations for which images were taken. While capturing the optical images, light intensity was kept to minimum to reduce the evaporation of droplets.

8) After completion of one set of experiment for both drills using Coolube oil, the system was cleaned with warm water and liquid soap to avoid oil cross-contamination. Warm water was drained through the system first, followed by the mixture of soap and warm water. Finally, warm water was drained through the system again until it showed no oil traces.

9) After cleaning the system, Castrol oil was inserted in the oil reservoir of the system. Same set of experiments was repeated for Castrol oil with both the drills.

Procedure for image processing is enlisted below:

Optical images were further processed with Adobe Photoshop 6.0 and ImageJ 1.52a.

1) Adobe Photoshop 6.0 was used to convert images to grayscale image.

2) Then the brightness and contrast were adjusted such that the resultant droplets can be clearly distinguished from the background of the image.

3) Using the Magic Wand tool, background of images was selected. This selection was inverted using Inverse command, to select the droplets.

4) Identified droplets were filled with black color, using the Fill command. Due to this command, the scale bar present on the images was also blackened.

5) To avoid counting the area covered by the scale bar, images were cropped to a size of 70 cm × 53 cm (1995 pixels × 1503 pixels) such that the scale bar will be omitted.

6) Image processing was further followed by ImageJ 1.52 a. Grayscale images obtained after processing in Photoshop, were converted to 8-bit images by adjusting the threshold. For adjusting the threshold, Default method with B&W option was used.

7) Watershed command in Binary options was used to separate coalesced droplets.

8) Before calculating the droplet areas, the scale was set to microns from pixels. For this conversion, the scale bar distance present on original microscopic images was used as a reference.

9) Using Analyze Particles command, droplet areas were calculated. Droplets on the edges were excluded to minimize the error in the calculation.

Detailed image processing steps are included in Appendix A.

3.1.2.3. Air jet diversion

These experiments were performed for studying the air jet diversion and airborne drop sizes resulting from only one coolant channel. The other coolant channel was blocked with heat activated wax. The distance between the drill centre and coolant hole was measured with the Olympus STM6 microscope, i.e., 2.45 mm.

Fixed parameters:

61

- Air flow rate: 1.7 m^3/hr (60 scfh)

- Input air pressure: 413 kPa (60 psi, 4.13 bar)

- Number of fluid strokes per min: 40 strokes/min

- Volume of fluid delivered per stroke: 0.016 mL

- Lubricant flow rate per hour: 38.4 mL/hr

- Time for collecting the resulting droplets: about 1 sec

- Drill size: 10 mm

- Lubricant: Castrol oil

  Variables:

- Distance between the drill tip and glass slide: 84, 107 mm
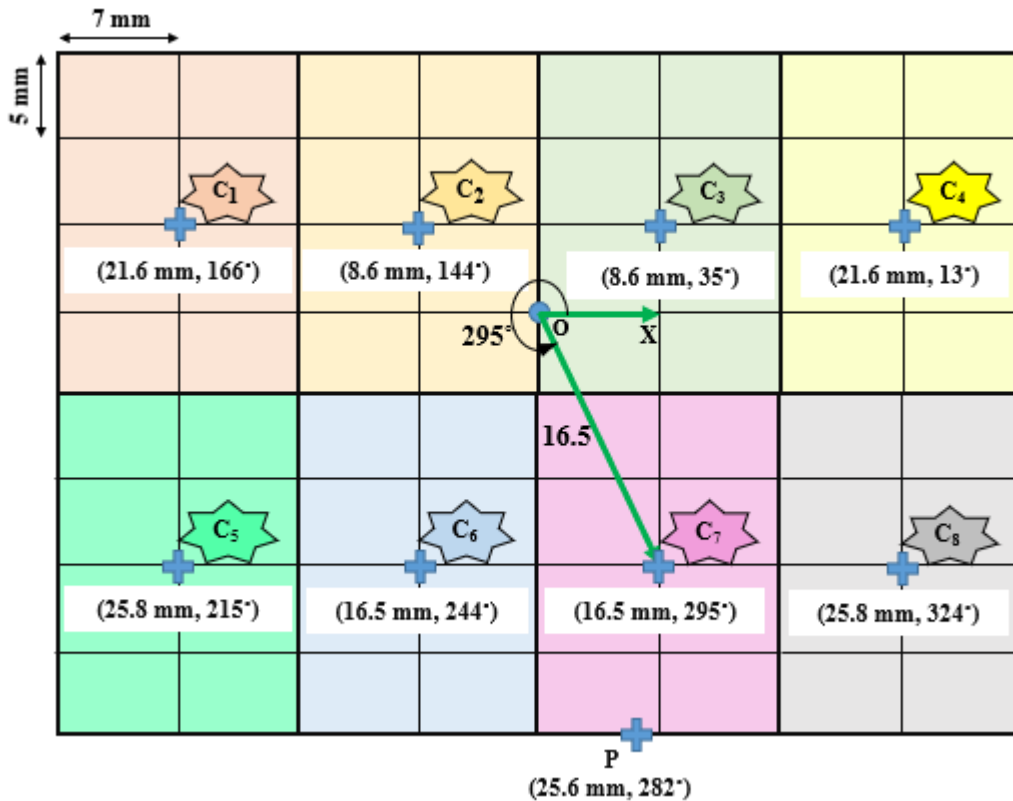
Figure 38. Polar coordinate representation of sections on the glass slide with respect to the centre of the droplet zone. Where, O: centre of the droplet zone, C_1 - C_8: centres of cluster zones, and P: drill projection centre

The following steps were followed for this experiment:

1) The coolant holes of the 10 mm drill were cleaned with isopropyl alcohol and then blew-dried with compressed air.

2) An electric stove was used for inserting the heat activated wax in one of the coolant channels of the drill. The drill was kept on the hot plate after selecting the temperature range of 93° C to 426° C.

3) The timer beeped after about 2 minutes indicating that the selected temperature range was achieved.

4) The wax was inserted in one of the coolant holes, as it easily melted due to the high temperature of the drill. The drill was kept ideal for about 3 minutes to harden the wax.

5) Steps 2 to 4 were repeated three times to ensure complete blockage of the coolant channel. Finally, drill was kept ideal for 5 minutes.

6) The compressed air was blown through the coolant channel to verify its blockage.

7) The drill was then attached to the Unist system to perform droplet collection experiments as mentioned in section 3.1.2.2.

8) The droplets were collected for about 1 second with distance between the drill tip and the glass slide as 84 or 107 mm. Two repetitions were performed for each distance.

9) Figure 38 shows the glass plate locations used for the data collection. Each image was 7 mm $\times$ 5 mm. Such 64 images were captured for each experiment.

10) Images processing steps for droplet diameter calculations were same as section 3.1.2.2 and Appendix A.

3.2. Droplet formation and flow
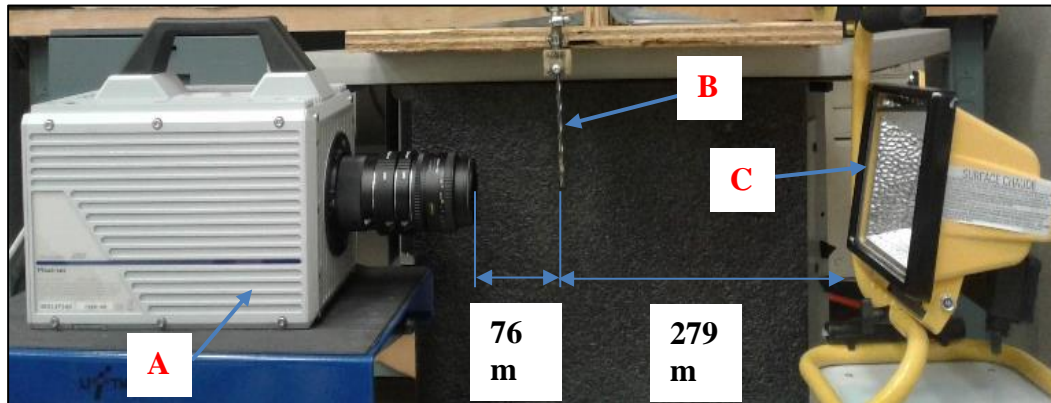
Figure 39. High speed camera setup for droplet formation. Where, A: Photron video camera with extension tubes, B: drill, and C: light source

The second set of experiments was performed for capturing the formation and motion of lubricant flow at the tip of a drill at different air pressures. The purpose of high speed imaging experiments was to study and compare the effect of air pressure on mist formation for both oils. These experiments were performed in two parts. For the first part, droplet flow was captured when the centre axis of the drill is perpendicular to the centre axis of the camera, as shown in Figure 39. In the second part, drill centre axis and camera axis are parallel to each other (Figure 40).

3.2.1. Equipment and software

Part I: Drill axis is perpendicular to the camera axis (Figure 39)

<u>List of equipment:</u>

    1.   Camera Jack

    2.   Drill (4 mm diameter) with dual coolant holes

3.   Extension tubes – 12 mm, 20 mm, 50 mm

4.   Lubricants: Coolube 2210 Al and Castrol Hyspray A 1536

5.   Photron FASTCAM viewer version 4.0

6.   Photron high speed camera FASTCAM SA5

7.   Portable Halogen Work Light E216569

Fixed parameters:

- Drill size – 4 mm

- Number of fluid strokes per min – 40 strokes/min

- Volume of fluid delivered per stroke – 0.016 mL

- Distance between the drill and camera – 76 mm

- Distance between the drill and halogen work light – 279 mm

Variables:

- Input air pressure - 413 kPa (60 psi), 551 kPa (80 psi) and 689 kPa (100 psi)

- Lubricants – Coolube oil, Castrol oil

Part II: Drill axis is parallel to the camera axis (Figure 40)
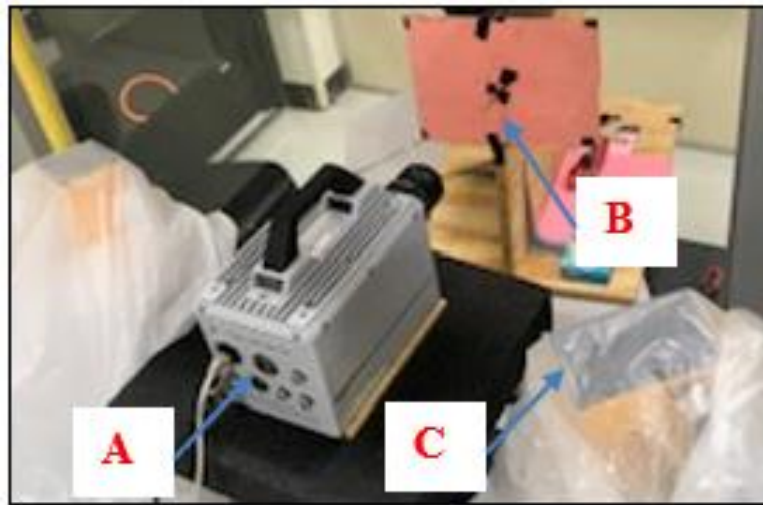
(a)
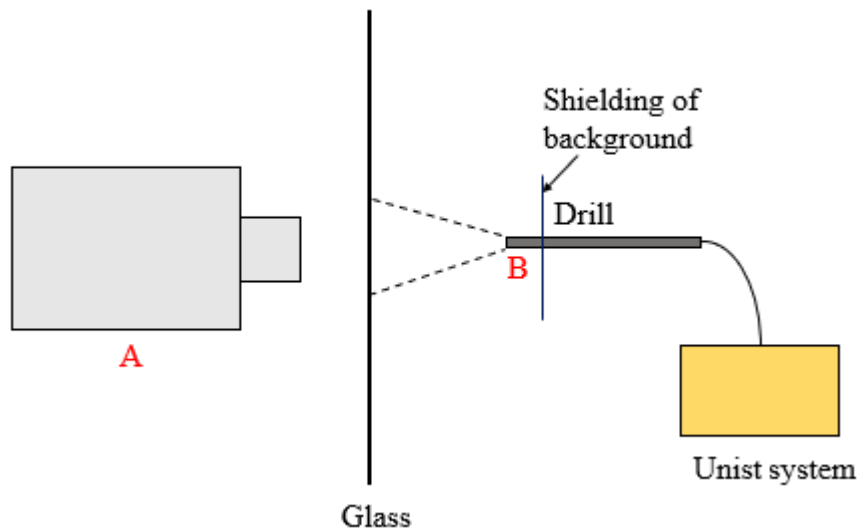
(b)

Figure 40. High speed camera setup for spray pattern. Where, A: high speed camera, B: drill, and C: light source

List of equipment:

1. 2 GS Vitec Multiled LT-V9-15 Lights

2. Drills (4 and 8 mm diameter)

3. Photron high speed camera FASTCAM SA5

4. Extension tube – 36 mm

5. Photron Software PFV4 (x64)

6. Candy Colors Oil based food coloring

7. Camera Jack

8. LED Light stands

Fixed parameters:

- Number of fluid strokes per min – 4 strokes/min

- Volume of fluid delivered per stroke – 0.016 mL

- Lubricant: Coolube 2210 Al

Variables:

- Drill size – 4 and 8 mm

- Distance of the drill from the glass surface – 25, 51, and 76 mm

- Input air pressure - 413 kPa (60 psi), 551 kPa (80 psi) and 689 kPa (100 psi)

3.2.2. Experimental procedure for high speed imaging

Part I:

Experimental setup is shown in Figure 39. Droplet formation and flow for each oil
at the tip of 4 mm drill was captured with a high speed camera (A). Drill (B), high speed
camera and halogen work light (C) were kept in a straight-line arrangement, so that light

from the halogen work light could give a clear contrast to the resultant droplets. Steps followed were:

1) A thin white paper diaphragm was placed in between the halogen project work light and the drill (not shown in Figure 40) to avoid bright background in images that would have caused loss of information and to minimize evaporation of droplets.

2) The extension tubes of 12, 20, and 50 mm were used in tandem for capturing closed-up images.

3) Images and videos were captured after about 15 seconds that allowed the system to stabilize after turning it on.

4) Images were captured at 42,000 frames per second, with shutter speed 1 µs and resolution 512×320 pixels.

5) Overall recording duration for the footage at air pressure 413, 551, and 689 kPa was 0.47 sec.

6) High speed digital images and videos were studied with Photron FASTCAM viewer 4.0.

Part II:

Experimental setup is shown in Figure 40. Droplet formation and flow for Coolube oil was captured with both the drills. After these tests, one coolant hole was plugged and the formation of micromist was investigated when there is no interference of the mist from the other hole. Steps followed were:

1) Coolube oil was poured in the reservoir with 18 drops of red oil-based food colouring and 8 drops of blue oil based food colouring to the reservoir and stirred thoroughly. This is to enhance contrast of droplets on the glass panel.

2) A pink color paper 216 mm × 280 mm with a cardboard backing was used. A small hole of the size of the drill was cut in the centre of the paper. The drill bit was inserted in this hole as shown in Figure 40.

3) The camera needed to be able to see the full spread of the micro mist on the glass surface. Therefore, the drill bit needed to be centered on the camera's lens so that the camera can capture the spread of the mist. To get the correct height vertically the camera was positioned on camera jack so that the drill bit is vertically centered on the lens.

4) The drill tip was aligned perpendicular to the glass surface.

5) A camera jack was used to place the camera in front of the glass plate as shown in the setup.

6) LED light poles were set on both sides of the camera. These lights were kept pointing towards the drill.

7) A 36 mm extension tube was used for the high-speed camera.

8) The focus of the camera was adjusted until the liquid on the glass plate was clearly seen.

9) The position of the LED lights was adjusted, and opaque plastic bags were used to obtain the best contrast between the liquid and the background.

10) Black electrical tape was placed around the drill bit so that the mist sprayed can appear more clearly in the videos.

11) A ruler was used to change the distance as 25, 51, and 76 mm between the drill and the glass surface.

12) A picture frame glass was used initially to block the flow of the mist on the glass plate. Once the system was stabilized after 15 seconds, the picture frame was removed.

13) The camera captured 7000 frames per second with the resolution 1024×1024 and shutter speed 1 µs. Total duration recorded by the camera was 3.12 seconds.

14) The images captured were processed for brightness and contrast with LUT command in PFV software.

15) After each test, the glass plate was cleaned with glass cleaner and acetone.

16) After these iterations of tests, one coolant hole of the drill was plugged with a toothpick.

17) With distance 76 mm and at air pressure 413 kPa, steps 11 to 15 were repeated for droplet collection on the glass plate.

3.3. Drilling tests

Drilling tests were conducted to investigate and compare the effect of both MQL oils and flood coolant in drilling of A380 die cast aluminium. The 8 mm diameter drill was used for drilling tests. A two levels factorial experiment was proposed to assess the

effect of air pressure and oil quantity on hole quality. Total of 80 holes were drilled on the aluminium plate using both the lubricants. A new drill was used for each set of experiment.

3.3.1. Equipment and software

1. A380 die cast aluminium plate (420 x 175 x 24 mm)

2. CNC mills with through-tool coolant capability

- HAAS VF2, 15,000 rpm max for Coolube oil

- GROB 515 5-axis (B/A) 16,000 rpm max for Castrol oil

- FANUC Robodrill, α – D21LiB5, 10,000 rpm max for flood coolant

3. Lubricants: Coolube 2210 Al, Castrol Hyspray A 1536, and TRIM MicroSol 585XT non-chlorinated semisynthetic water-based microemulsion

4. Mitutoyo digital micrometer

5. Mitutoyo Vision System QS-E 2010 B

6. Olympus STM6 measuring microscope

7. Drills with dual coolant holes (8 mm diameter)

8. Unist Infinitive system

Assumptions:

1. Carbide tool wear is insignificant when drilling A380 die cast aluminium.

2. Porosity is evenly distributed in the cast volume and it does not affect the drilling process and chip evacuation while machining.

3. Work hardening on one drilled hole does not affect the adjacent hole since the edges are at least 2 mm apart.

4. Spindle/drill runout on each machine are insignificant.

Fixed parameters:

1.   Spindle speed = 9950 rpm (250 m/min cutting speed)

2.   Feed rate = 3980 mm/min (0.20 mm/flute chip load)

3.   Drilling time = 0.40 sec to drill a through hole on 24 mm plate thickness

4.   Drill size (8 mm diameter)

Variables:

1.   MQL air pressure – 413 kPa (60 psi) and 620 kPa (90 psi)

2.   MQL oil quantity – 40, 60, 100 and 400 mL/hr

3.   Flood coolant flow – 340 L/hr and 5678 L/hr

4.   Flood coolant concentration in water – 5% and 10%

5.   Nozzle diameter (flood coolant supply) – 3.17 mm for 340 L/hr flow rate, 12.70 mm for 5678 L/hr flow rate

6.   Lubricants – Coolube oil, Castrol oil, and TRIM MicroSol 585XT

3.3.2. Experimental procedure for drilling

The actual diameters of the 8 mm drills were measured with the Mitutoyo digital micrometer. The steps followed are enlisted below:

1) A micrometer stand was used to ensure repeatability and to minimize the human errors.

2) The micrometer was mounted on the micrometer stand. The anvil and the spindle were used to zero it.

3) The drill was placed between the anvil and the spindle such that the shank just above the flute of the drill was measured.

4) The process was repeated for 5 measurements of each drill.

Drilling was performed on the aluminium plate based on chosen parameters and variables. The drilling test involved following steps:

1) A Unist Infinitive system was used to supply a constant flow of lubricant.

2) For every 25 mm wide section of aluminium plate, there were two rows of drilled holes. The distance between centres of two consecutive circles was 10 mm and the distance between the centre lines of two rows was 10 mm. Figure 41 details the hole layout followed for drilling.

Test matrices with randomized sequence for both lubricants and flood coolant are shown in Table 4 and Table 5 respectively, with 5 repeats each. Each row had 40 drilled holes for each lubricant. The equivalent fluid pressure for flood coolant shown in Table 5 was calculated by equation (7)[1].

$$P' = K'' \left(\frac{Q_n}{D_n{}^2} \right)^2 \tag{7}$$

Where,

[1] http://irrigation.wsu.edu/Content/Calculators/Sprinkler/Nozzle-Requirements.php

P': Pressure at nozzle (kPa, psi)

Q_n: Flow rate of water from nozzle (m³/hr, gpm)

D_n: Nozzle diameter (mm, in)

$K''=6.6\times10^4$ when P':kPa, Q_n: m³/hr, D_n:mm

$K''=1.2\times10^{-3}$ when P':psi, Q_n:gpm, D_n:in

3) CNC mills with through-tool coolant system were used to drill through the 24 mm

plate thickness.
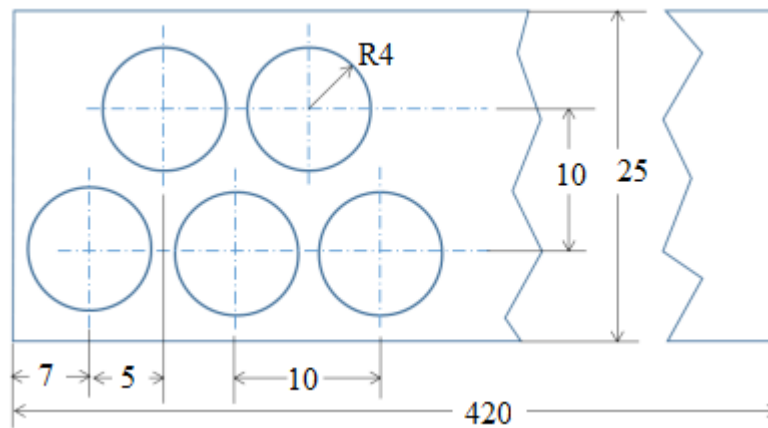
Figure 41. Hole layout. Unit: mm.

Table 4. Test matrix for MQL drilling

Test No.	Air pressure (kPa)	Oil quantity (mL/hr)
1	413	40
2		60
3	620	40
4		60
5	413	100
6		400
7	620	100
8		400

Table 5. Test matrix for flood-coolant drilling

Equivalent fluid pressure (kPa)	Flood coolant flow (L/hr)	Coolant concentration in water (%)
76	340	5
		10
83	5678	5
		10

3.4. Drilled hole quality

3.4.1. Equipment and software

1. A380 die cast aluminium plate (420 x 175 x 24 mm)

2. MCOSMOS-3 version 3.2 R6 Edition 6

3. Mitutoyo Strato-Apex 7106 CMM

3.4.2. Experimental procedure for metrology
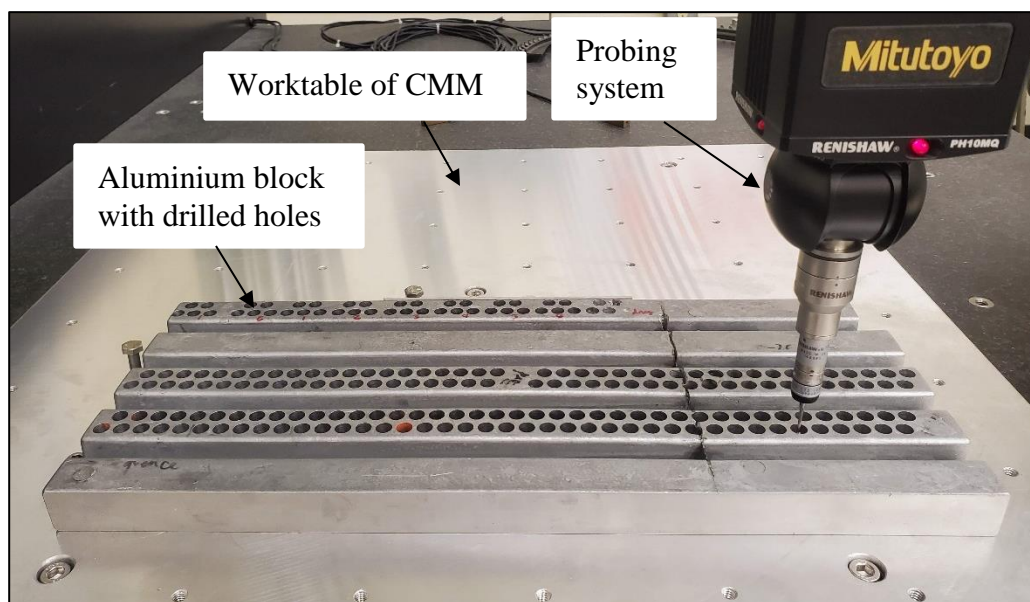
Figure 42. Experimental setup on CMM for hole quality assessment.

Hole quality for each hole was evaluated with Mitutoyo Strato-Apex 7106 CMM and its modular software MCOSMOS-3 for cylindricity and hole diameter.

1) The aluminium block was cleaned by blowing compressed air through each drilled hole to blow chips generated during machining.

2) The aluminium plate was kept on the worktable of CMM. It was supported by two brackets on sides.

3) After turning on the CMM and air supply at 413 kPa, it was made sure that it starts from its home position by pressing the Start button on the double joystick.

4) Alignment was a necessary step to the specify datum for accurate measurements. 'Plane, line and line' type of alignment was followed because of the aluminium plate geometry.

5) For cylindricity measurement, method of parallel circles was used. Three circles with equidistant depths of 6 mm were used for the measurement having initial distance of 3 mm as shown in Figure 43. For each circle, 5 data points were sampled. Once the data points for one circle were sampled, the stylus moved in vertical axis to the prescribed measurement depth and measured the data points for the next circle.

6) The measurement procedure was set up in a loop which was repeated for all the measurements. Detail alignment and measurement procedure is mentioned in Appendix B.

7) The MCOSMOS software displayed the measurements and graphical image on its interface, which were saved later in an output file.
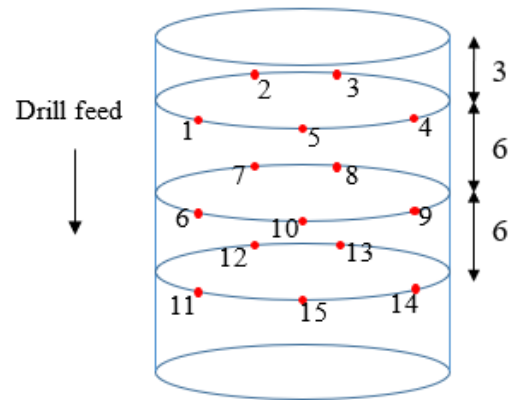
Figure 43. Schematic of cylindricity measurement for drilled holes. The typical numbers (1-5) represent probed points on a circle 3 mm below the drilled hole entrance. Unit: mm

CHAPTER 4

RESULTS AND DISCUSSIONS

4.1. Contact angle measurement

Contact angles for Coolube and Castrol oils on polished A380 aluminium block and glass plate with 0.1 µL volume were measured. The measurements were taken for droplets not covering pores on A380 Al plate (Figure 44). The average of 15 contact angle measurements for each oil on glass and on polished A380 Al block is listed in Table 6. The contact angles for both oils on glass were considered when calculating the airborne sizes of micromist droplets. However, the contact angles measured on A380 block implied the wettability of each oil on die cast A380 aluminium, which was used for drilling tests. Equation (4) was used to calculate the contact angles based on known volume of the lubricant and its projected diameter. Assumptions associated with this equation, including no evaporation of droplets, negligible gravity effect due to small volume, and perfect spherical shape were considered to be true in this calculation.
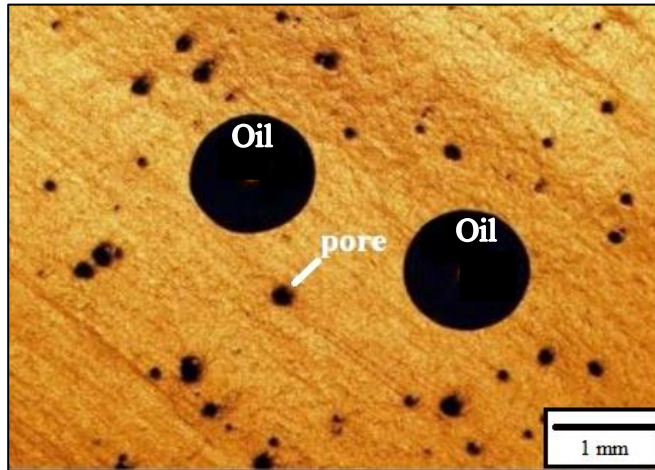
Figure 44. Oil droplets on polished A380 Aluminium plate

The contact angles for Castrol oil on glass and on polished A380 block were greater than those of Coolube oil. Coolube oil resulted in smaller contact angles of about 6˚ on glass and 22˚ on the polished A380 block. For Castrol oil, contact angles were about 22˚ on glass and 33˚ on the polished A380 block. Coolube oil easily spreads on the glass and on the A380 block, due to lower surface energy. In other words, the adhesive forces between the oil and these solid surfaces were stronger than the cohesive forces within the oil.

The Coolube oil, having smaller contact angle, would have better wetting characteristic due to its lower surface energy and lower viscosity (Stephenson & Agapiou, 2016). Thus, it would move more efficiently to tool/chip interface by capillary action to remove heat and lubricate a tool (Li et al., 2015; Walker, 2013).

Table 6. Contact angle of different oils on glass and polished A380

Measurements	On glass		On polished A380	
	Coolube 2210Al	Castrol Hyspray A 1536	Coolube 2210Al	Castrol Hyspray A 1536
Projected diameter for 0.1 µL oil drops (mm)	2.188	1.515	1.557	1.218
	2.288	1.560	1.394	1.429
	2.249	1.559	1.266	1.100
	2.201	1.317	1.426	1.239
	2.150	1.326	1.318	1.072
	2.130	1.230	1.349	1.237
	2.143	1.248	1.353	1.100
	2.089	1.453	1.306	1.407
	2.108	1.435	1.323	1.131
	2.126	1.506	1.336	1.176
	2.408	1.508	1.047	1.253
	2.398	1.528	1.863	1.133
	2.126	1.507	1.414	1.094
	2.116	1.190	1.552	1.256
	2.133	1.223	1.851	1.119
Average diameter (mm)	2.190±0.101	1.407±0.135	1.424±0.212	1.198±0.110
Contact angle (°)	5.60±0.70	21.49±6.31	21.81±8.63	33.16±7.27

4.2. Droplet formation and flow

Two sets of data were obtained by high speed imaging technique to capture the flow of lubricants. First set of data was collected when viewing the lubricant flow by positioning the camera perpendicular to the drill axis and second set of data when viewing the flow with the camera parallel to the drill axis.

4.2.1. View perpendicular to the drill axis

Figure 45(a)-(f) compares the droplet formation of Coolube and Castrol oils at the drill tip. As drill coolant hole sizes and shapes affect the micromist formation and flow (Kao et al., 2017), the smaller drill of 4 mm diameter was chosen since its smaller oil channels are more difficult for oil to flow.

It was observed that at pressure 413 kPa, Coolube oil tends to form thicker liquid threads, which break up into droplets due to air pressure (Figure 45(a)). At 551 kPa, liquid threads were seen at the tip of the drill (Figure 45(c)). However, these liquid threads are thinner than those at 413 kPa. These threads disperse into droplets quicker as compared to 413 kPa. In contrast, at 689 kPa, no liquid threads were observed, instead, micro-droplets were formed (Figure 45(e)).

For Castrol oil, at air pressure 413 kPa, the oil tends to remain at the tip of the drill, instead of dispersing into droplets (Figure 45(b)). For 551 kPa air pressure, oil remains at the drill tip, however it disperses into droplets quicker than that of 413 kPa (Figure 45(d)). In case of 698 kPa air pressure, oil disperses into droplets quicker than 551 kPa, however, tendency of the oil sticking to the drill tip is observed (Figure 45(e)). Time required to form the droplets was more for Castrol oil than that of Coolube oil.

83

It was observed that Castrol oil required very high air pressure to form the micromist. With high speed imaging technique, it was observed at lower air pressures, micromist droplets highly tend to coalesce with each other. However, the mist included finer droplets with increasing air pressure. High viscous Castrol oil did not flow easily through the coolant holes of the drill. This was related to the basic fluid mechanics about the air flow inside a channel. The air velocity was zero at the wall of the coolant channel and the highest at the centre. Therefore, high viscous oil stuck to the surface of the coolant channel, which resulted in fewer micromist droplets flying out of the drill.
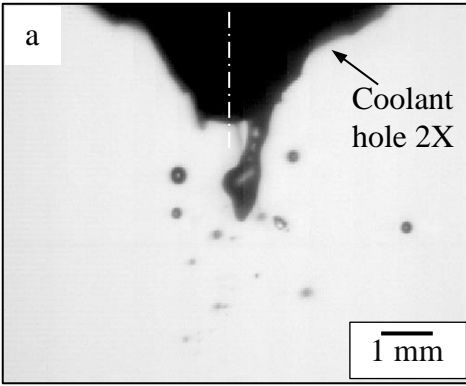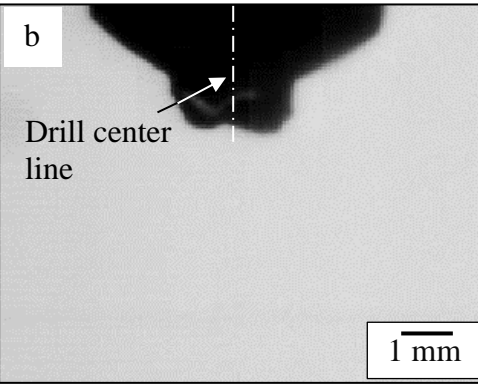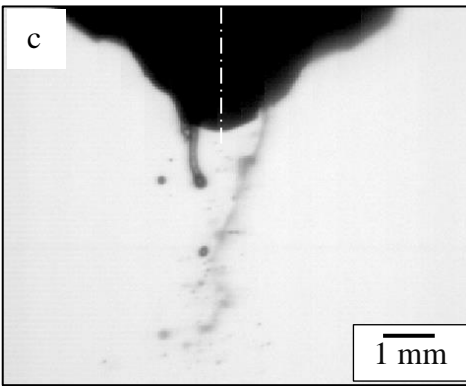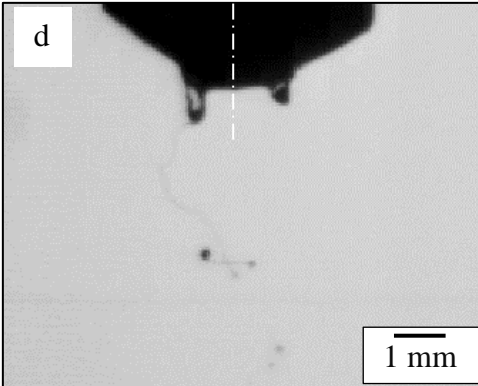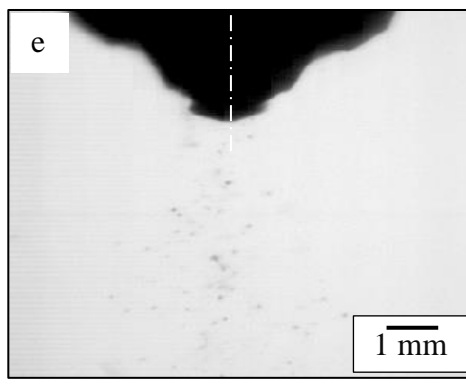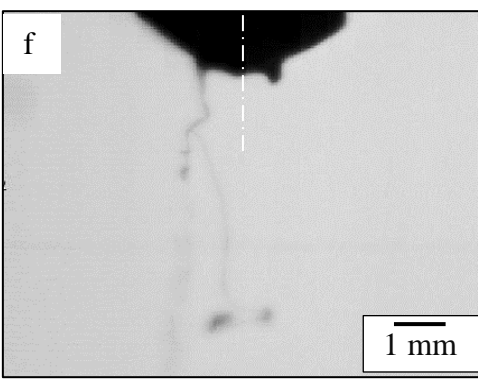
Air pressure (kPa)	Coolube oil (265th frame at 6 ms)	Castrol Oil (669th frame at 16 ms)
413	a Coolant hole 2X 1 mm	b Drill center line 1 mm
551	c 1 mm	d 1 mm
689	e 1 mm	f 1 mm

Figure 45. Droplet formations, 4 mm drill at different air pressures

85

In case of 8 mm drill experiments, mist droplets would have been finer than 4 mm drill due to the higher airspeed in larger coolant channels of 8 mm drill (Kao et al., 2017). The tendency of oil to stick near the drill centre would have been observed as well. Higher air pressure would result in finer mist droplets and there would have been far less coalescence of droplets with each other as higher pressure broke down droplets into smaller drops (Khan et al., 2018). On the other hand, 4 mm drill possessed lower airspeed in coolant channels due to smaller coolant channel size than that of 8 mm drill. Thus, lubricant droplets were also found to coalesce with each other (Kao et al., 2017).

(a) Inactive stroke, 507th frame at 12ms, 551 kPa

(b) Active stroke, 885th frame at 21ms, 551 kPa

(c) Inactive stroke, 730th frame at 17ms, 689 kPa

(d) Active stroke, 815th frame at 19ms, 689 kPa
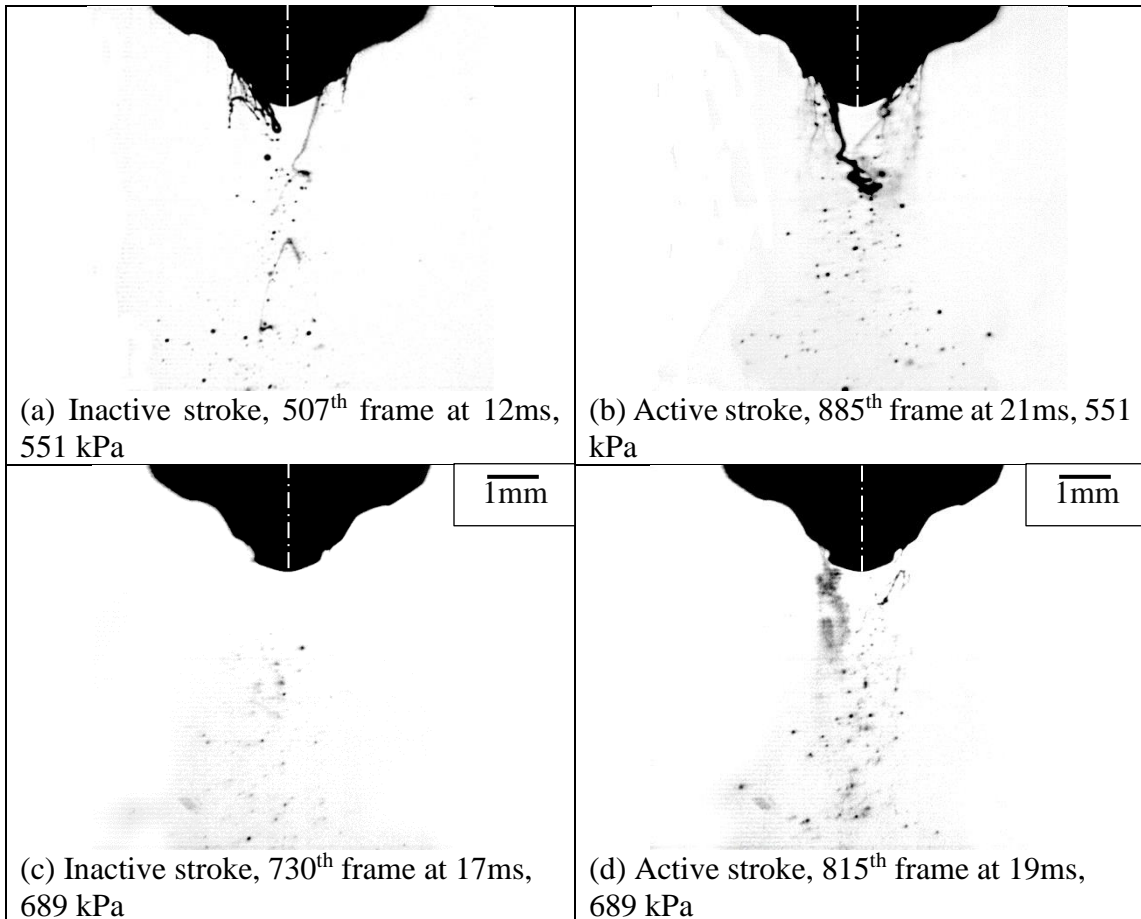
Figure 46. Effect of pump frequency on microdroplet formation. Coolube oil, 4 mm drill, pump frequency 0.67 Hz (40 strokes/min).

Two microdroplet formation mechanisms were evident in the high-speed video. The Unist system operated at 40 strokes/min (0.67 Hz) in this study. During the inactive stroke, the system sucked in 0.016 mL lubricant from the reservoir and then pumped this volume to the air-jet stream during its active stroke. Under a steady air flow, microdroplets were formed continuously, but additional microdroplets were formed during the active pump stroke.

- During the inactive stroke, some microdroplets deposited on the inner channel wall, formed a stream of lubricant, flowed downstream with additional gravity effect, and then collected as a lubricant pool at the drill tip. When the cumulative volume of lubricant was sufficiently large, the air stream then broke down the lubricant pool into oil strings and larger microdroplets (Figure 46(a)).

- During the active stroke, a fresh volume of lubricant was pumped into the air-jet stream and atomized inside the aerosol reservoir. The newly atomized aerosol then flowed into both lubricant channels and exited out of the holes near the drill tip (Figure 46(b),(d)). Cyclic bursts of oil microdroplets were seen in synchronicity with the pumping frequency. Coalescence of airborne microdroplets were expected from the large microdroplets that come from the pool at drip tip and the smaller microdroplets that exited from the lubricant channels. Fine aerosol streams were visible at both hole exits near the drill centreline. Perhaps there were finer microdroplets at the exit holes away from the centreline, but such micron-level airborne microdroplets were not captured due to insufficient resolution of the Photron camera.

4.2.2. View parallel to the drill axis

When the drill axis was parallel to the camera axis, the impact zone was defined as the area covered with the mist droplets on the glass panel. Two distinct oil jet streams and impact zones were observed in each case. Each impact zone was a result of the mist directed out of each coolant hole of the drill (Figure 47). These two zones illustrated that the micromist exited the coolant holes of the drill at an outward angle rather than parallel with the drill centre axis. The outward angle of the mist can result in covering more surface area of the workpiece. The centre line angle was defined as the angle between the centre lines associated with the impact zones formed due to the coolant holes, as shown in Figure 47. There was an overlapping area between the impact zones where very few droplets were present due to the interference from both the coolant holes. The distance between the centres of the two impact zones was measured by visually inspecting the mist impacted on the glass panel and then utilizing the Adobe Photoshop software to determine the pixels between the centres of the impact zones. The area the camera recorded was a 30 x 30 mm square. However, the camera registered the size of the image in a 1024 x 1024 pixel image. Therefore, each pixel was 0.03 mm. Thus, the number of pixels was multiplied by 0.03 mm to get the actual distance.
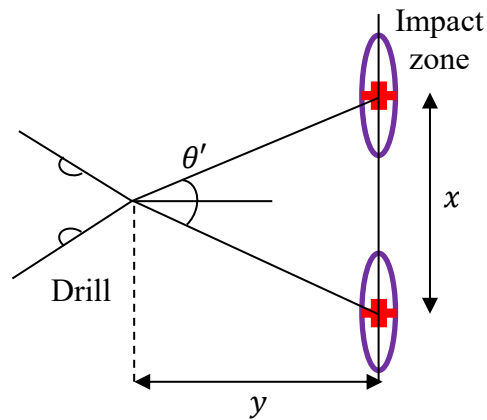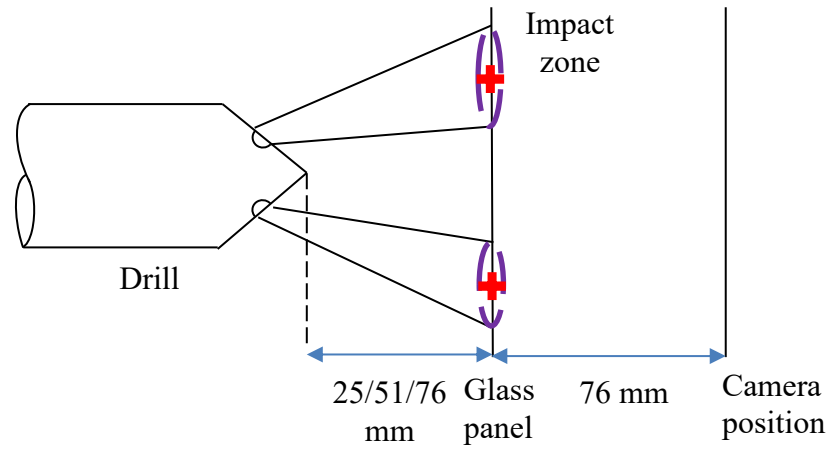
Figure 47. Centre line angle and impact zones on the glass panel

The mist formation for Coolube oil with 25 mm distance between the glass and the 8 mm drill at air pressure 413 kPa is shown in Figure 48. From the high-speed camera videos, it was observed that the 8 mm drill produced smaller droplets than 4 mm drill.

Table 7 summarizes the distance between the impact zone centres for both the drills at different air pressures and the corresponding centre line angles. The centre line angles were calculated as shown in equation (8):

$$\theta' = 2tan^{-1}\left(\frac{x}{2y}\right) \qquad\qquad (8)$$

Where,

θ': Centre line angle (˚)

x: Distance between the centres of the two impact zones (mm)

y: Distance between the drill and the glass panel (mm)

      The droplets exiting the coolant holes of the drill travelled at an angle rather than parallel to the drill axis. Thus, the droplets travelled further away in the direction those were headed, creating the larger impact zones with the increased distance between the drill and the glass panel. The increased size of the impact zones also minimized the droplets' coalescence. As indicated in Table 7, the distance between the impact zone centres increased for both the drills, with increasing distance between the glass panel and the drill at all the pressures.
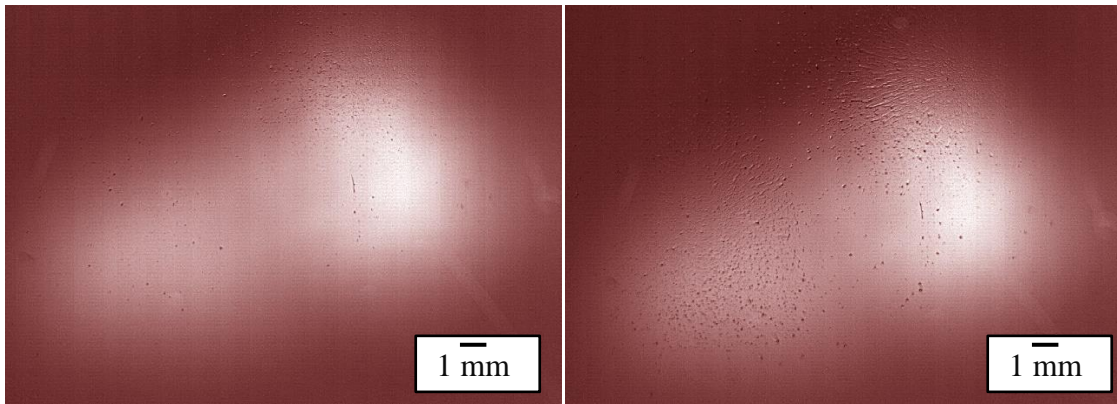
(a) 111th frame at 15 ms　　　　**(b) 311th frame at 44 ms**
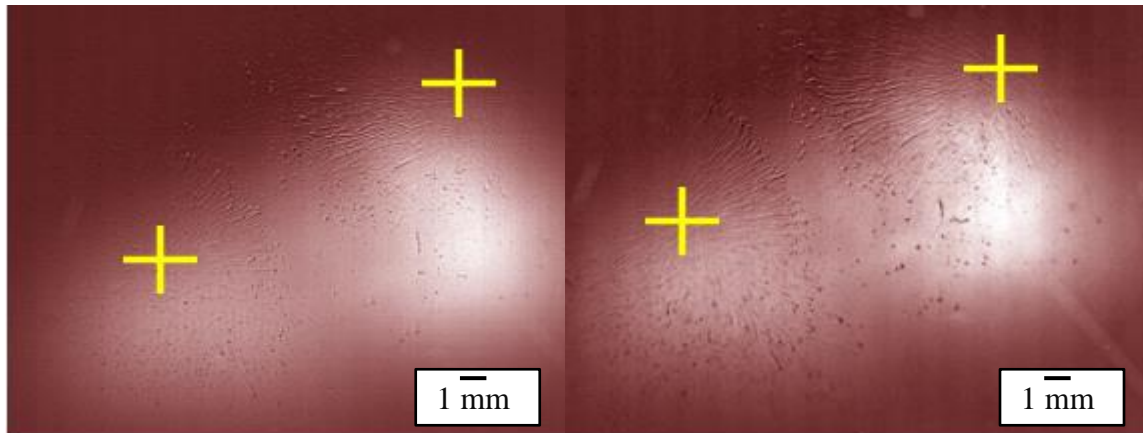
(c) 511th frame at 73 ms　　　　**(d) 711th frame at 101 ms**
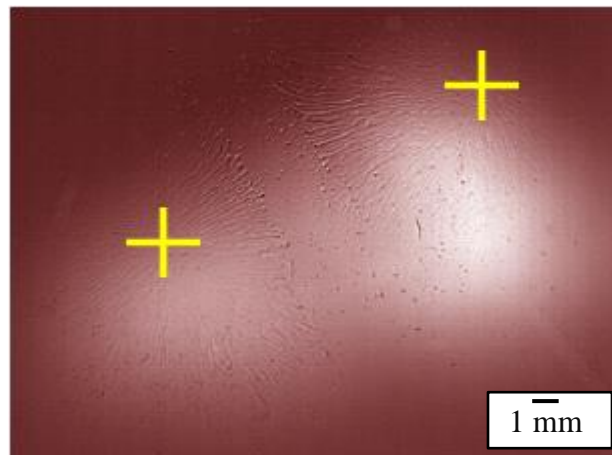
(e) 911th frame at 130 ms

Figure 48. Mist formation for Coolube oil. 25 mm distance between the 8 mm drill and the glass panel. Air pressure 413 kPa. The "+" sign indicates the centre of an oil jet stream flowing into the glass panel.

Table 7. Zone centres' distances, centre line angles (2 drills, different air pressures)

Air Pressure (kPa)	Distance between the drill and glass panel (mm)	8 mm drill		4 mm drill	
		Distance between 2 zone centres (mm)	Centre line angle (°)	Distance between 2 zone centres (mm)	Centre line angle (°)
413	25	13	29	14	31
	51	18	20	21	23
	76	---	---	---	---
551	25	14	31	12	28
	51	17	19	17	19
	76	---	---	---	---
689	25	16	36	10	22
	51	19	21	14	15
	76	---	---	---	---

Note: The "---" symbol indicates non-conclusive information

From Table 7 indicates non-conclusive information in case of 76 mm distance between the drill and the glass panel. Due to this distance, many droplets fell off due to gravity and very small droplets might have evaporated before hitting the glass panel. Thus, the images and videos for such cases did not imply any significant information. 64 mm

(2.5 in) distance between the drill and the glass panel is recommended for future studies to minimize the loss of information.
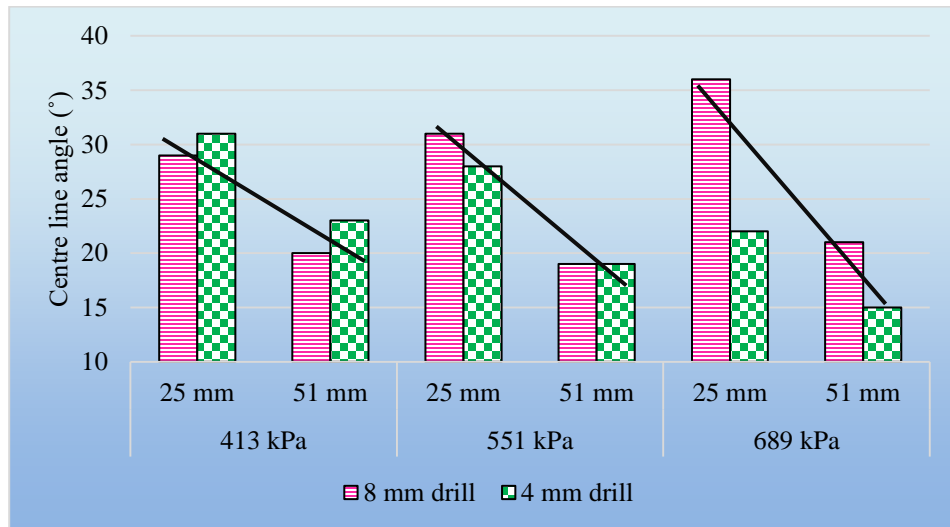
Figure 49. Centre line angles for 4 and 8 mm drills with varying distance between drill tip and glass panel and different air pressures.

Centre line angles calculated for both the drills with 25 mm distance between the drill and the glass panel were about 30˚ at all the air pressures. This implied that the distance between the drill and the glass panel might be proportional to the distance between the two impact zone centres. For 56 mm distance from the glass panel to the drill, there was a potential chance of information loss because of gravity and evaporation of droplets. Centre line angles for both the drills in this case were about 20˚ at all the air pressures. Overall, the airborne droplet streams flowed towards the drill centre line after hitting and merging on the glass panel, and the centre line angle decreased with increase in the distance between the drill and glass panel. Similarly, Kao et al. (2017) observed the lubricant accumulation near the drill centre point for circular coolant channels.
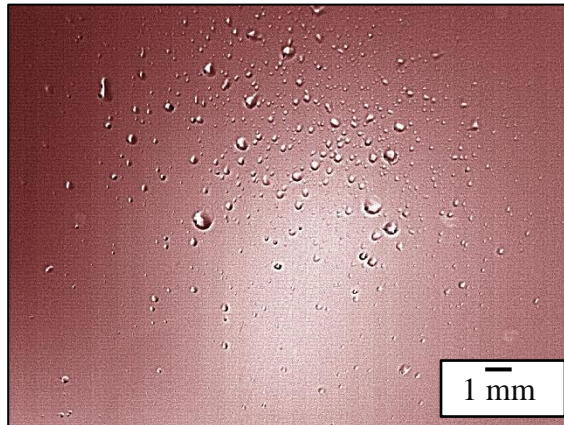
Figure 50. Oil mist formation for Coolube oil on vertical glass panel. One coolant hole plugged for horizontally positioned 4 mm drill. 7651st frame at 1092 ms. 76 mm distance between the drill and the glass panel. Air pressure 413 kPa.

Figure 50 shows the image of Coolube oil mist formation with one coolant hole plugged for 4 mm drill at air pressure 413 kPa and 76 mm distance between the drill and the glass panel. As the distance between the drill and the glass panel was 76 mm, many droplets did not hit the glass panel due to gravity and evaporation. No specific shape or pattern of droplets' coalescence was observed. In addition, no centre of the oil jet stream was seen due to possible turbulent flow of air stream. This result for 76 mm distance was consistent with other cases when both the coolant holes were unplugged.

Castrol oil would have resulted in larger droplets as compared to Coolube oil. The dispersion tendency of oil from the drill tip would have been similar, however, mist generation in case of Castrol oil would take longer than Coolube oil, as seen in first part of the experiments. Larger droplets would have been generated with Castrol oil and the smaller drill as compared to the larger drill. Higher air pressure would result in finer mist with Castrol oil, as observed in first part of the experiments.

94

4.3. Airborne diameter measurement and distribution

It was observed that the different sections on the glass plate, which were near to the drill centre contained significantly more droplets than those which were comparatively far from the drill centre. Specifically, sections 1, 2, and 4 contained more droplets than sections 3, 5, 6, 7 and 8 on the glass plate (Figure 37). Sections 1, 2, and 4 also contained more droplets which were coalesced with each other. However, droplets collected in remaining sections were less and separate from each other. Figure 51 shows microscopic images and image processing steps with Adobe Photoshop and ImageJ software for experimental data of sections 1 and 8 of the glass plate. These sections were at the radial distances 0 and 93.4 mm respectively from the drill centre line. In droplet collection experiments, some smaller droplets might have evaporated before settling down on the glass slide. In image processing with ImageJ and Adobe Photoshop, very small droplets of airborne diameters less than 1.6 μm were not captured.

(a)

(b)

(c)
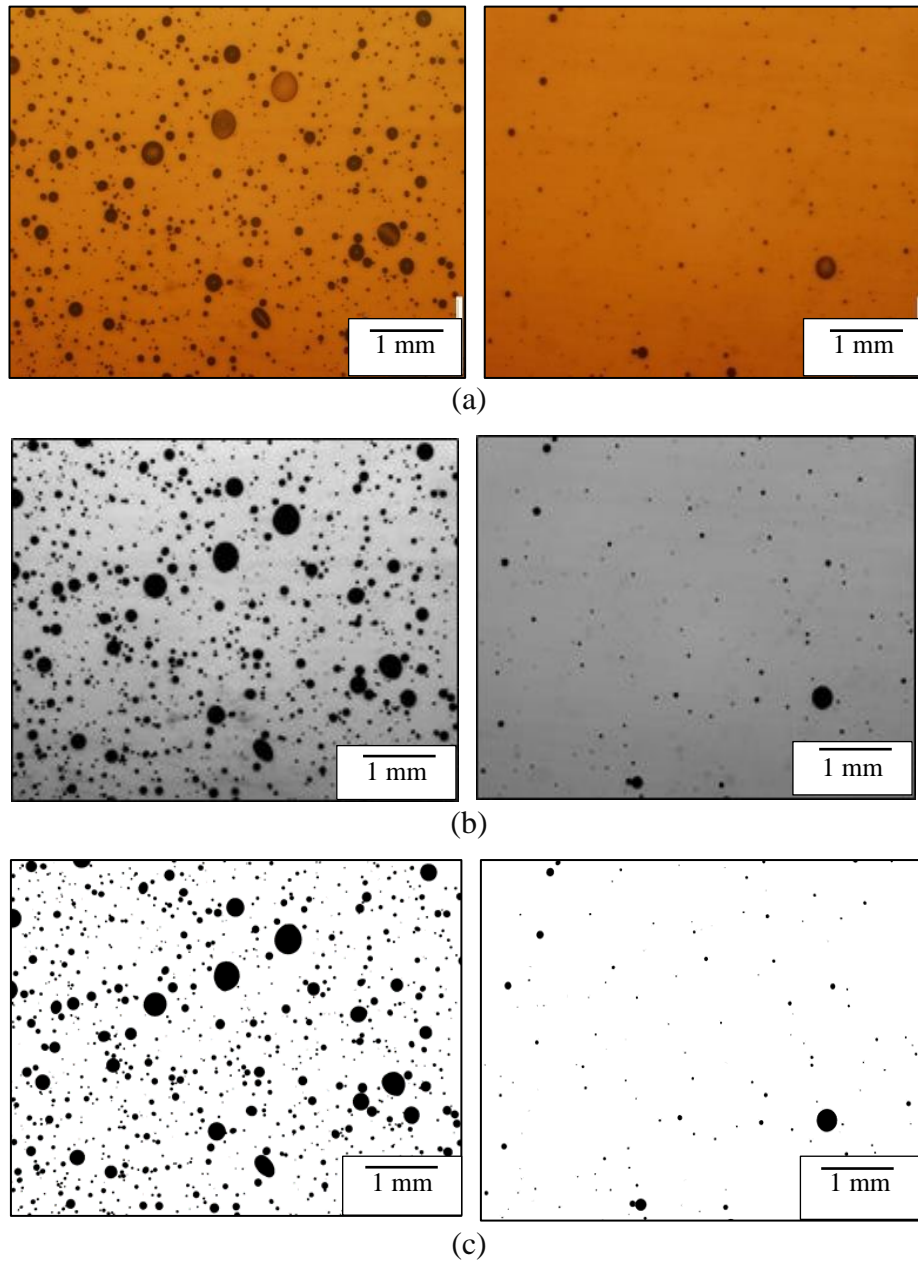
Figure 51. Glass slide sections at 0 mm (left) and 93.4 mm (right) radial distances from the drill centre. Microscopic images for Castrol oil at 413 kPa (a) deposited droplets on glass plate; (b) after image processing using Adobe Photoshop; (c) after image processing using ImageJ

The area for deposited droplets for each set of experiment was obtained from

ImageJ software. It was assumed that droplets were perfectly spherical and thus that area

was used to calculate the projected diameter (Figure 52). Equations (9) and (10) were used

for calculation as follows.
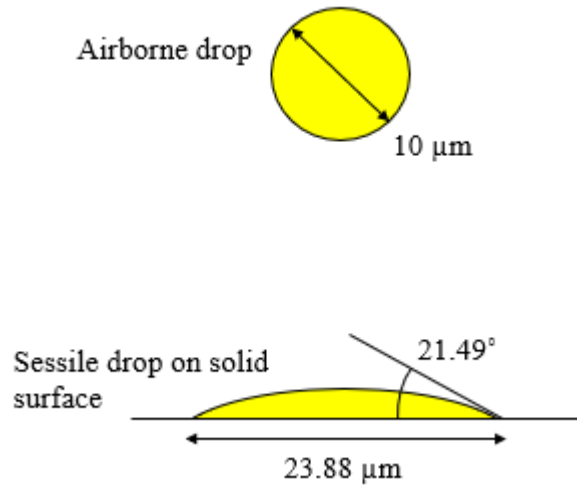
Figure 52. Airborne and sessile drop

Sample calculation:

Case: 413 kPa air pressure, 8 mm drill, Castrol oil (Contact angle $\theta \approx 21.49°$ on glass plate)

A: Shaded area of a droplet calculated from ImageJ ≈ 448 μm²

P: Projected diameter of the droplet (μm)

Projected diameter calculation:

$$P = 2\sqrt{\frac{A}{\pi}} = 2\sqrt{\frac{448}{\pi}} \approx 23.88 \text{ μm} \tag{9}$$

Airborne drop volume calculation:

$$\frac{P}{V''^{\frac{1}{3}}}(\theta) = \left[\left(\frac{24}{\pi}\right)\left(\frac{(1 - K\cos^2\theta)^{3/2}}{2 - 3\cos\theta + \cos^3\theta}\right)\right]^{1/3} \tag{10}$$

0° < θ < 90°, hence, K=1

Thus, from equation (10),

$$V''' = \left(\frac{\pi P^3}{24}\right)\left(\frac{2 - 3cos\theta + cos^3\theta}{(1 - cos^2\theta)^{3/2}}\right) \tag{11}$$

$$= \left(\frac{\pi 23.88^3}{24}\right)\left(\frac{2 - 3\cos 21.49 + cos^3 21.49}{(1 - cos^2 21.49)^{3/2}}\right)$$

$$\approx 513 \text{ µm}^3$$

Airborne diameter of a spherical droplet is:

$$d = \left(\frac{6V'''}{\pi}\right)^{1/3} = \left(\frac{6 * 513 \text{ µm}^3}{\pi}\right)^{1/3} \approx 10 \text{ µm} \tag{12}$$

The resultant airborne diameters and standard deviations calculated from all the experiments were plotted in the form of histograms to study their distribution (Figure 53 and Figure 54). Airborne drop sizes greater than 150 µm were expected to be the result of droplet coalescence. Thus, histograms plotted are for droplets with airborne sizes less than 150 µm.
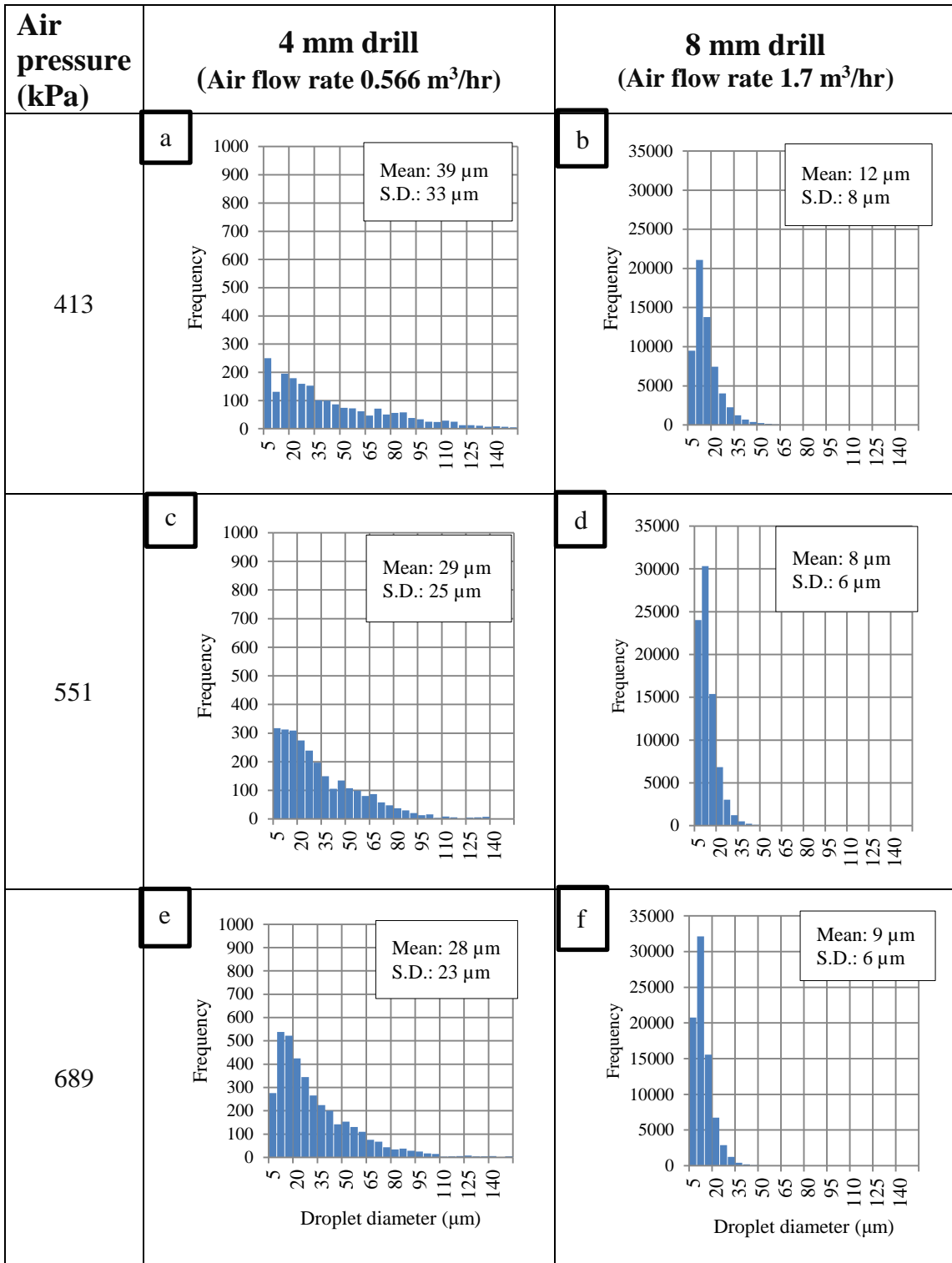
Figure 53. Airborne drop size distribution, mean and standard deviation of Coolube oil at different air pressures.

Air pressure (kPa)	4 mm drill (Air flow rate 0.566 m³/hr)	8 mm drill (Air flow rate 1.7 m³/hr)
413	a — Mean: 26 µm, S.D.: 23 µm	b — Mean: 19 µm, S.D.: 18 µm
551	c — Mean: 24 µm, S.D.: 22 µm	d — Mean: 18 µm, S.D.: 16 µm
689	e — Mean: 24 µm, S.D.: 23 µm	f — Mean: 17 µm, S.D.: 15 µm
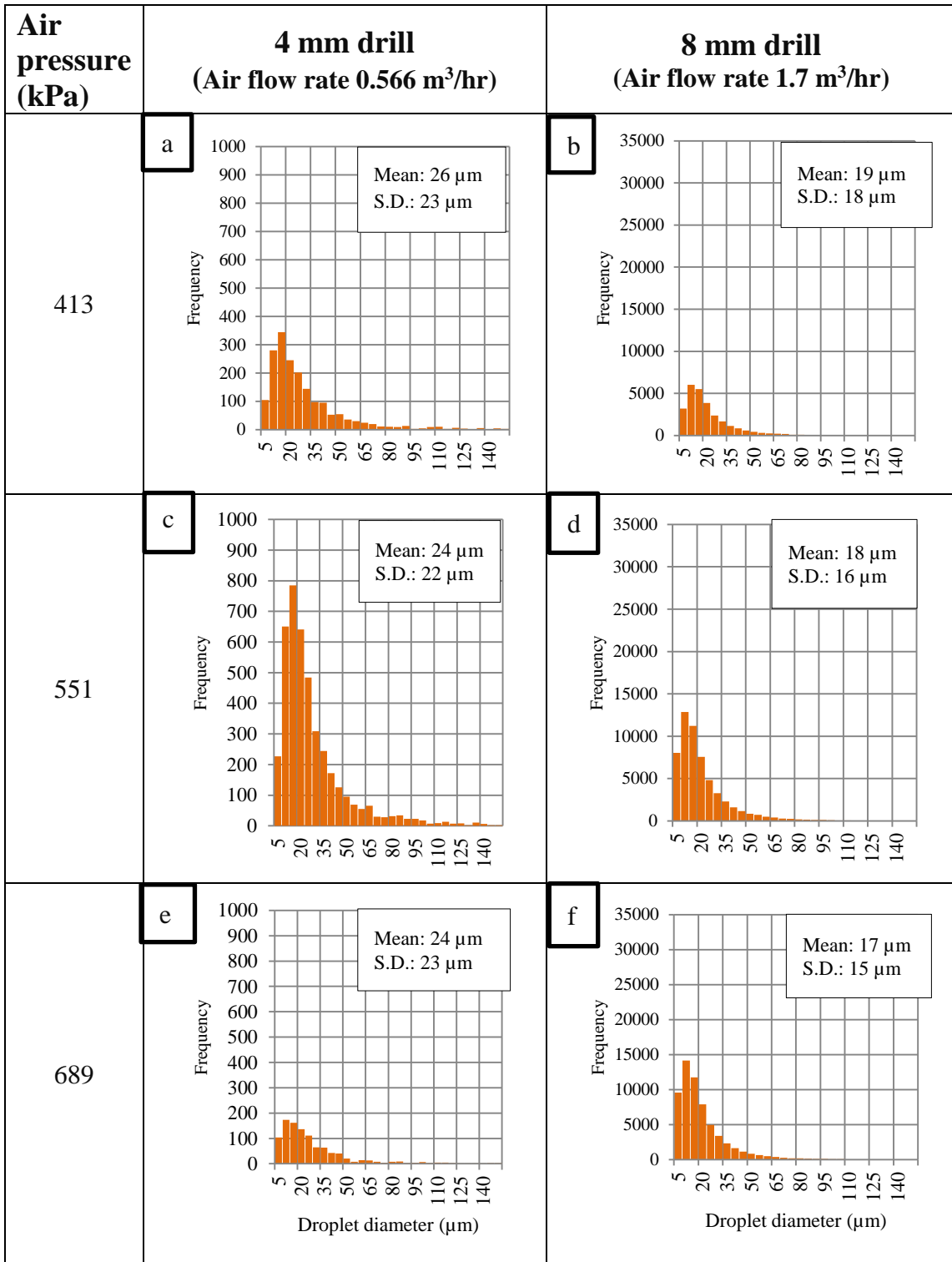
Figure 54. Airborne drop size distribution, mean and standard deviation of Castrol oil at different air pressures.

In all the cases it was observed that the standard deviation from the mean airborne diameter was large. Therefore, it was implied that the mean value was not a good estimator for airborne diameters. Instead of considering the average value of the whole set, different clusters of different sizes of airborne diameter was considered to be a better estimate.

Due to a large variation in airborne diameters, the K-means clustering method was used to identify the clusters of different airborne diameter range (James et al., 2017). For results of all the cases, the "elbow method" was used to plot the within-cluster sum of square against number of clusters from 1 to 15. There was a sudden drop in sum of squares at K=3 in every case. Figure 55 shows the elbow plots for airborne drop diameters of both the oils with 4 mm drill and air pressure 551 kPa. Thus, the total number of clusters was chosen to be 3 for effective comparison in all the cases and avoid overfitting of the data.
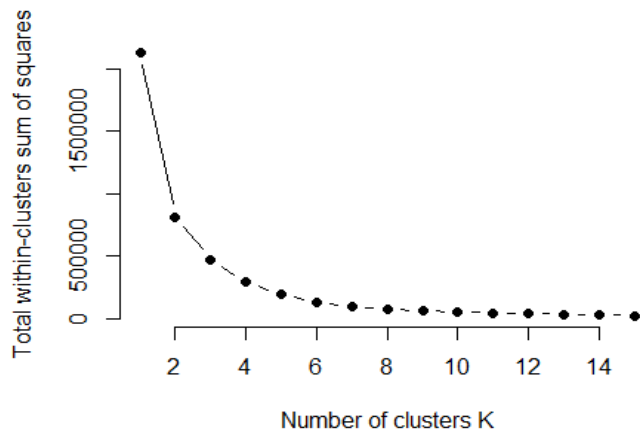
(a)
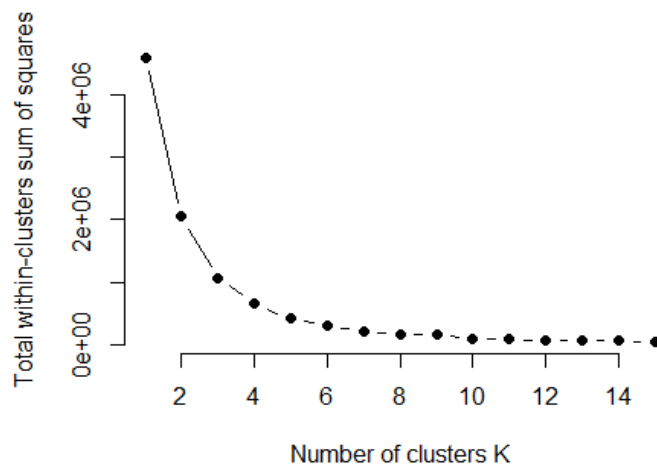
(b)

Figure 55. Elbow plot for airborne droplet diameters of (a) Coolube oil (b) Castrol oil. Air pressure 551 kPa, 4 mm drill

Figure 56 summarize the airborne diameter sizes for 413, 551 and 689 kPa with 4 and 8 mm drill experiments with Coolube and Castrol oils. For both the lubricants, the number of droplets collected with 8 mm drill experiments was much higher than that of the 4 mm drill at all three air pressures. The trendlines in Figure 56 indicated that the smaller droplets formed cluster 1, medium size droplets formed cluster 2, and the bigger droplets formed cluster 3 in all the cases for both the oils.
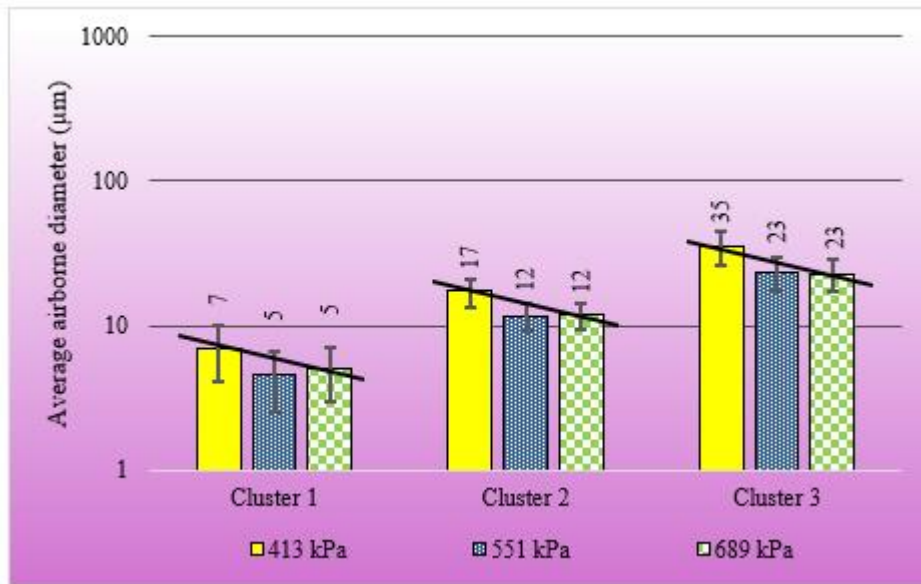
(a) 8 mm drill
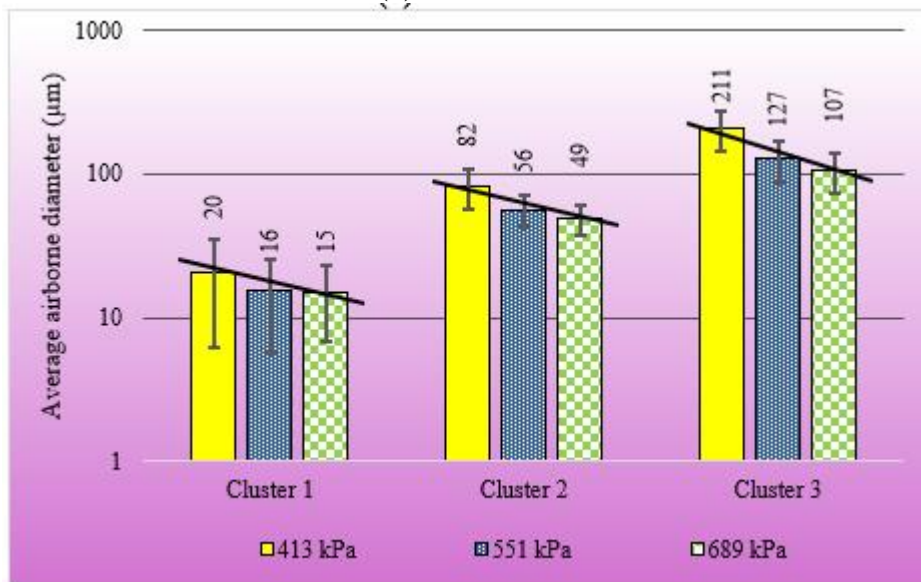
(b) 4 mm drill
Figure 56. Average airborne diameter for Coolube oil at different air pressures

- In Figure 56(a) (Coolube oil, 8 mm drill), the airborne drop size decreased for all

  three clusters, when pressure was increased from 413 to 551 kPa. However,

airborne diameter values observed at 689 kPa were almost equal to the values obtained at 551 kPa.

- In Figure 56(b) (Coolube oil, 4 mm drill), the airborne diameter size decreased with increase in pressure for all three clusters. The airborne drop sizes at 689 kPa were closer to those obtained at 551 kPa, as compared to 413 kPa for all the clusters. Khan et al. (2018), Liu et al. (2012), and Park et al. (2010) also found the same tendency of airborne diameters to decrease as pressure increases.
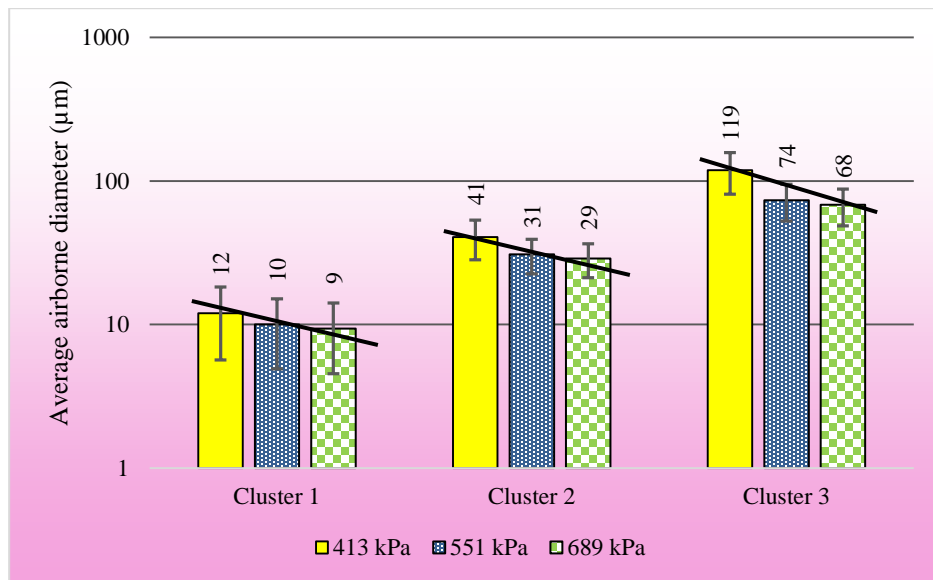
(a) 8 mm drill
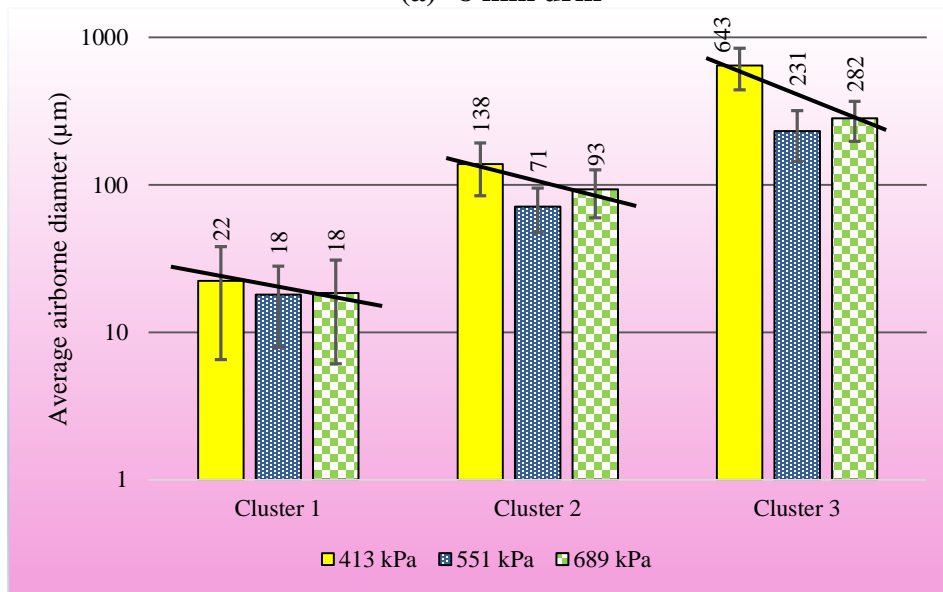
(b) 4 mm drill

Figure 57. Average airborne diameter for Castrol oil at different air pressures.

- Figure 57(a) (Castrol oil, 8 mm drill) shows the airborne diameter reduction with pressure increase for each cluster. The reduction in diameter corresponding to 551 to 689 kPa is lesser as compared to that of 413 to 551 kPa for all three clusters.

- In Figure 57(b) (Castrol oil, 4 mm drill), similar to other cases, droplet diameter reduction is significant from 413 to 551 kPa pressure increase, however, values of airborne diameter against 551 and 689 kPa pressure are relatively closer. In this case, there is a slight increase in droplet diameters from 551 to 689 kPa air pressure for each cluster.
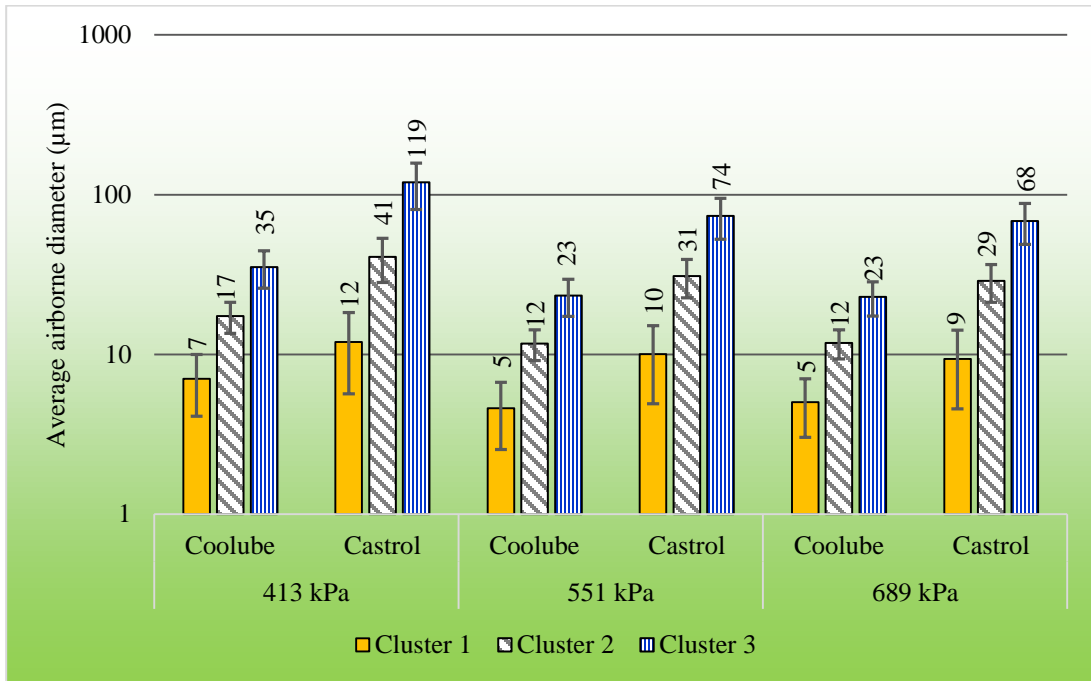
(a)   8 mm drill
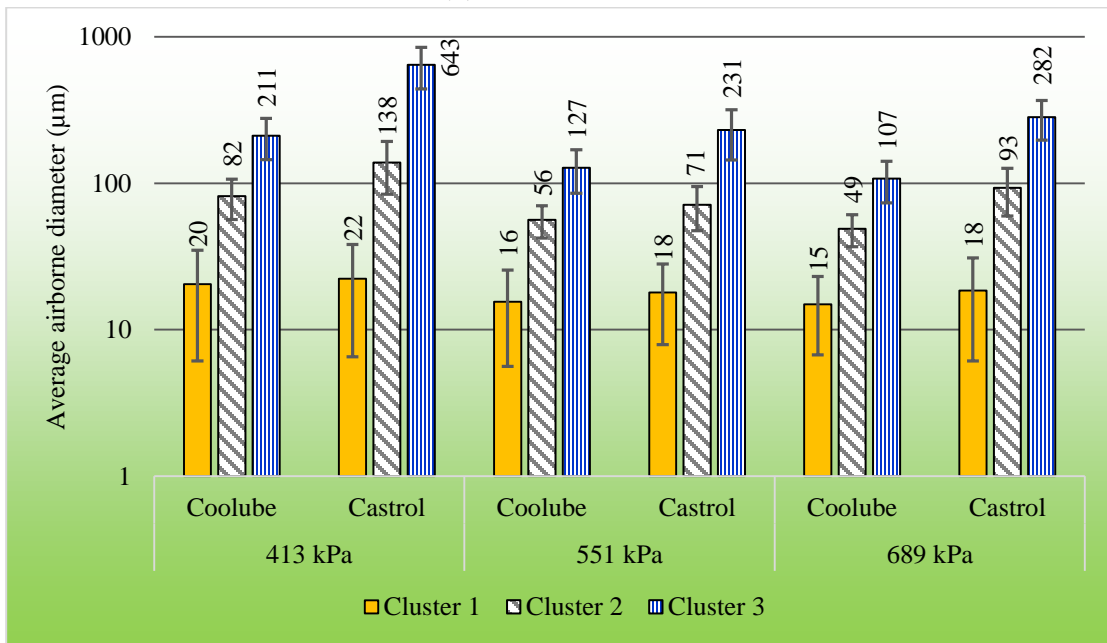
(b)   4 mm drill

Figure 58. Average airborne diameter comparison for both oils at different air pressures.

- Figure 58(a)-(b) compare the airborne droplet diameters for both oils against varying air pressure for 4 and 8 mm drills. The average airborne diameters in all the clusters were larger for Castrol oil than that for Coolube oil at all three pressure values with both the drills. For both the oils and drills, the average airborne diameters decreased for each cluster with the increase in air pressure.

- Average airborne diameters in each cluster were smaller for 8 mm drill (coolant channel diameter 1 mm) case than those for 4 mm drill (coolant channel diameter 0.7 mm) at all three air pressures. Similar results were obtained by Kao et al. (2017) in their study. According to Kao et al. (2017) and Stephenson et al. (2019), airspeed inside the coolant channels increased with the diameter of the channel, when the input air pressure was constant. Thus, the high airspeed generated finer droplets (Li et al., 2015; Liu et al., 2012). Hence, smaller coolant channel of 4 mm drill, caused more droplets to coalesce. Also, this was concluded from the droplet formation and flow study using high-speed imaging technique (Section 4.2).
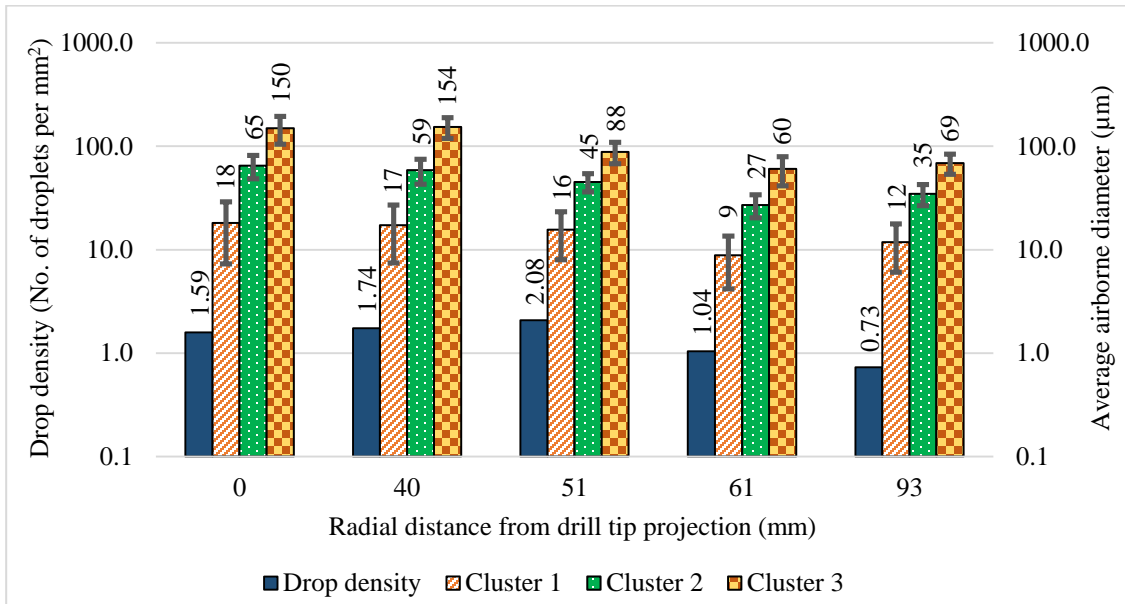
(a) Coolube, 4 mm drill, 689 kPa
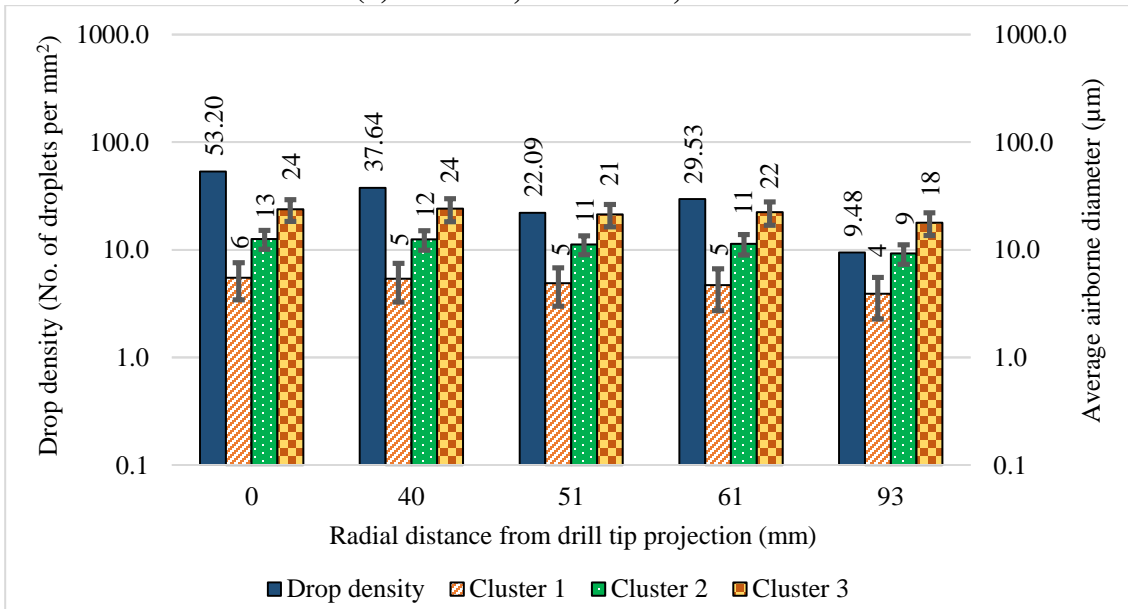
(b) Coolube, 8 mm drill, 689 kPa

Figure 59. Droplet characterization for different sections on the glass slide
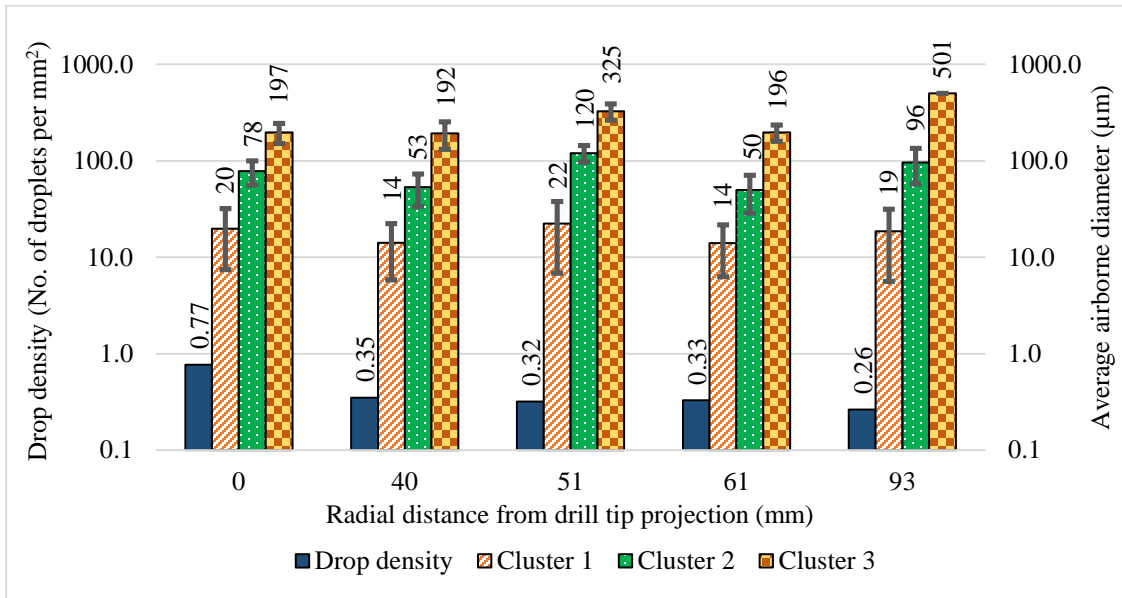
(c) Castrol, 4 mm drill, 689 kPa
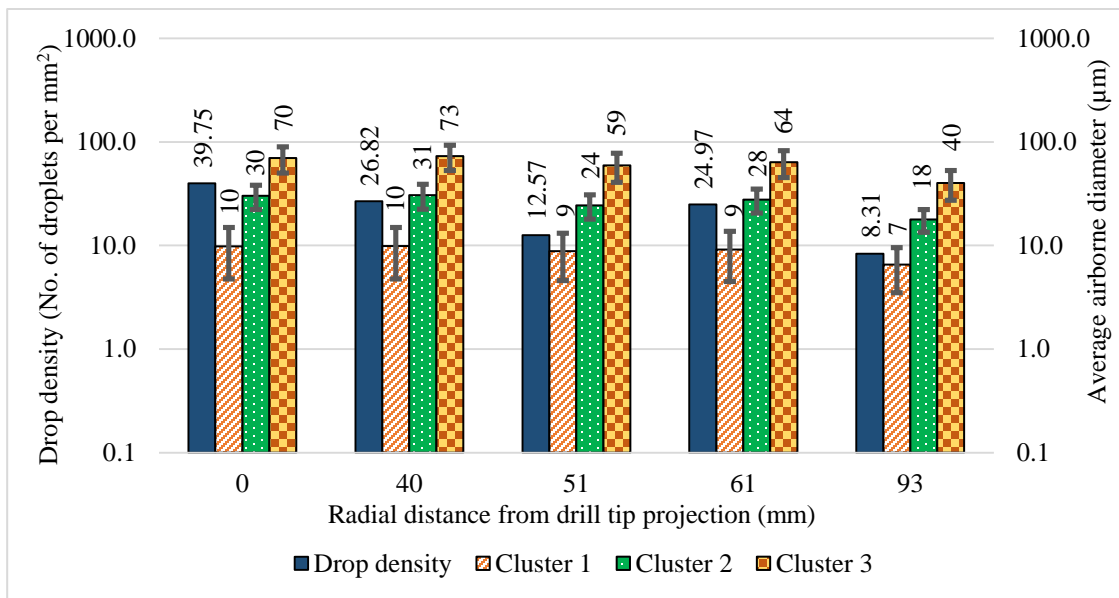
(d) Castrol, 8 mm drill, 689 kPa

Figure 59. Continued

Drop density was defined as the ratio of number of droplets in a section to the area of that section in mm^2. The sections on the glass panel with same distance from the drill tip projection were combined, as the distance between the drill tip and the glass panel was sufficiently large (~355 mm).

- For both the oils, 8 mm drill experiments resulted in much higher drop density compared to those of 4 mm drill for each section on the glass panel at a different radial distance from the drill tip projection. However, for both the oils, average airborne drop diameter was smaller with 8 mm drill as compared to that of 4 mm drill for each section and each cluster. Thus, 8 mm drill produced more number of smaller microdroplets due to higher airspeed inside the coolant channels (Figure).

- Considering both oils and both drills, the section at 93 mm radial distance from drill tip projection showed lesser drop density than that of the section at 0 mm radial distance (Figure).

- For both the drills, Coolube oil resulted in larger drop density and smaller sized droplets for all sections as compared to those with Castrol oil. Due to lower viscosity of Coolube oil, it generated micromist more effectively (Figure).

- The larger drill with larger coolant hole channel produced smaller drop size. Similar conclusion was also obtained by other studies (Kao et al., 2017; W. A. Khan et al., 2018; Liu et al., 2012; Raval et al., 2019; Stephenson et al., 2019).

4.4. Air jet diversion

112
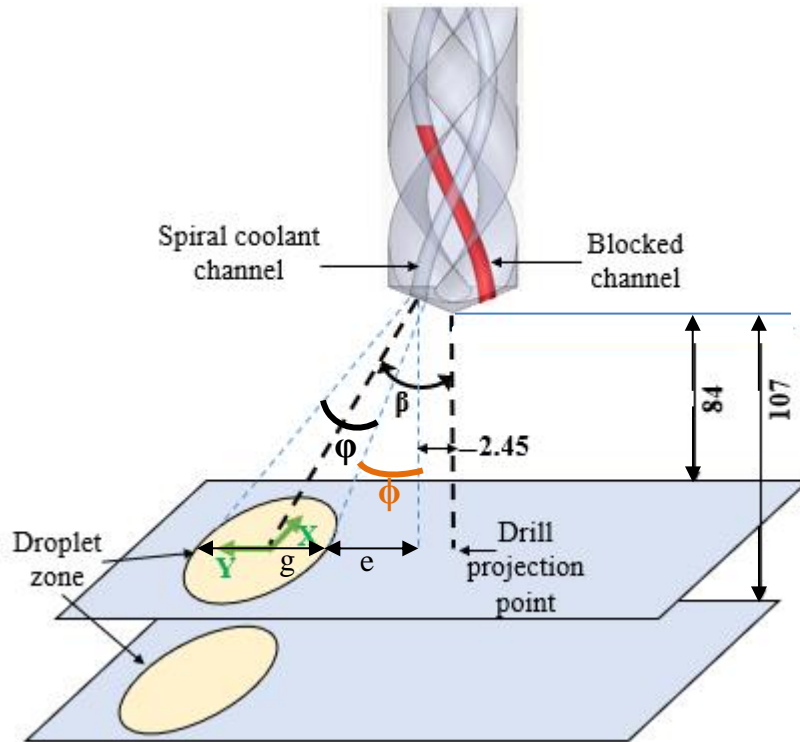
Figure 60. Cone angle representation. Unit: mm

The air jet diversion and the droplet zone position with respect to the drill position for one coolant channel of 10 mm drill was studied using Castrol oil at 413 kPa. The cone angle β and the droplet zone coverage angle φ were calculated to analyze the diversion of the jet resulting from the coolant channel (Figure 60).

Images captured for Castrol oil droplets at 413 kPa with only one coolant channel unblocked of 10 mm drill were merged as shown in Figure 61(a). These images were processed to identify the droplet zone and its centre. Droplet zone was a contour on the processed image which incorporated most of the droplets. The centre of the droplet zone was embedded in the region with the highest drop density (Figure 61(b)). Distance between the drill projection point and the centre of droplet zone was measured from the processed microscopic images (Figure 38, Figure 61).

113
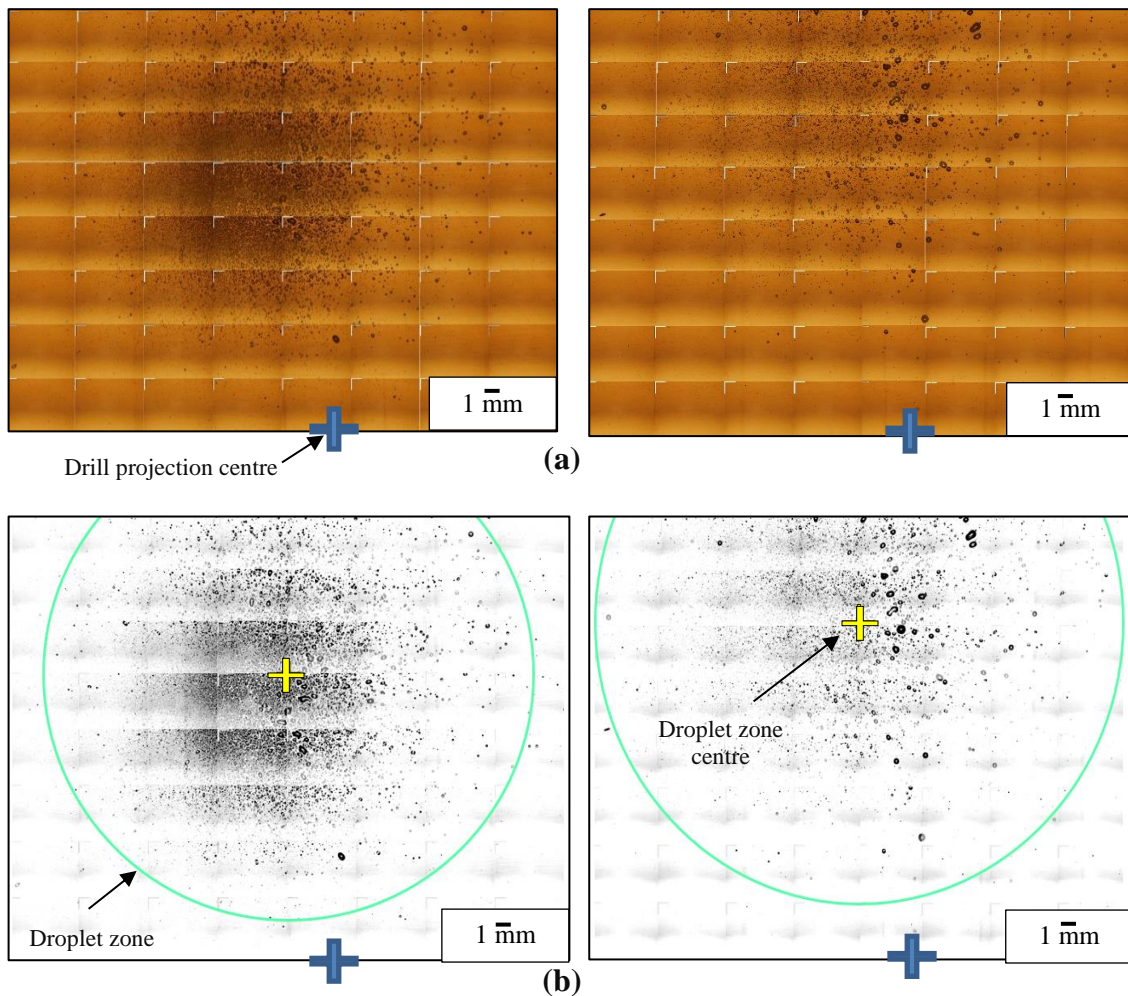
Figure 61. Glass slide at 84 mm (left) and 107 mm (right) distances from the drill centre. Microscopic images for Castrol oil at 413 kPa (a) deposited droplets on glass plate; (b) after image processing using Adobe Photoshop

- The droplet zones were formed at 25 mm radial distance from the drill projection point (referring to Figure 38). This was attributed to the geometry of the drill, including, 140° point angle, 30° helix angle, and curvature of helical coolant channel. The centrifugal forces due to the fluid motion in the coolant channel

caused oil to flow toward the wall and formed high velocity region away from the chisel edge (Lin et al., 2017; Raval et al., 2019; Tang et al., 2016). Thus, higher drop density was not in the vicinity of drill projection centre. This was also observed in high speed camera experiments with the view parallel to drill axis. The oil stream flowed at an outward angle with respect to the drill axis (section 4.2.2). There was no interference of droplets exiting the other coolant channel as it was blocked and to minimize droplet coalescence, the time for data collection was about 1 second. If data collection time would have been larger and other coolant channel would have been unblocked, droplets would have deposited near the drill projection centre as well.

- As the distance from the droplet zone centre increased, droplet sizes and drop density reduced based on the polar coordinates (Figure 38, Figure 62). In airborne droplet diameter and distribution study, sections on the glass slide at same radial distance from drill projection point were considered similar and their data was combined for analysis, because the distance between drill tip and glass slide was large enough (355 mm). In air jet diversion study, data collected from sections at same radial distances from droplet zone centre were not combined, as the distance between the drill and the glass slide was less (84 or 107 mm). Most of the droplets were captured in 64 images when the distance between the glass slide and drill centre was 84 mm, as the droplet zone was smaller. However, with 107 mm distance between the glass slide and drill centre, the droplet zone was larger, and

64 images could not represent the entire droplet collection. More droplets coalesced and formed larger droplets in smaller droplet zone (Figure 61(b)).
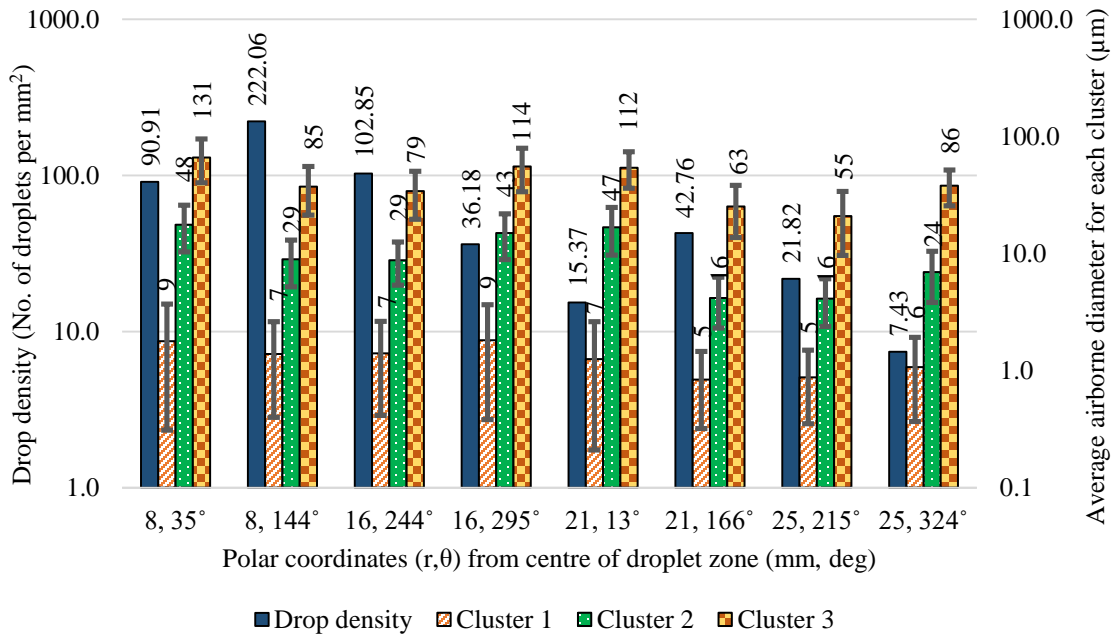
(a) 84 mm
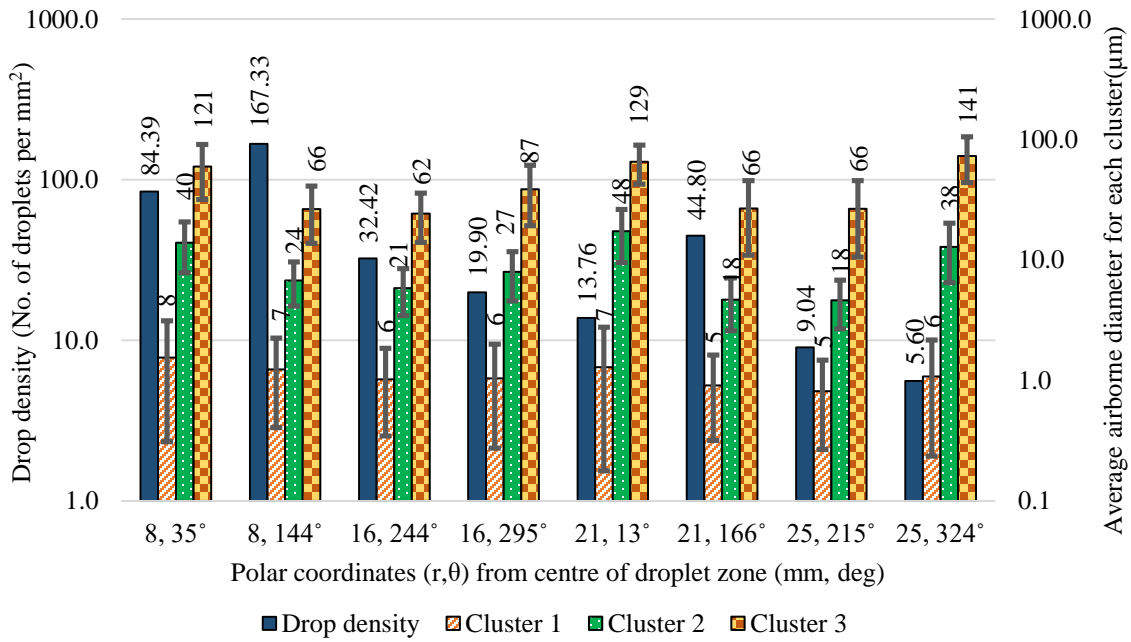
(b) 107 mm

Figure 62. Castrol oil droplet characterization at different sections on glass slide at 413 kPa with one unblocked coolant channel of 10 mm drill. Distance between drill and glass slide (a) 84 mm (b) 107 mm

Cone angle calculation:

Point angle of drill = 140˚

Horizontal distance between drill centre and coolant hole centre = 2.45 mm (Figure 63)
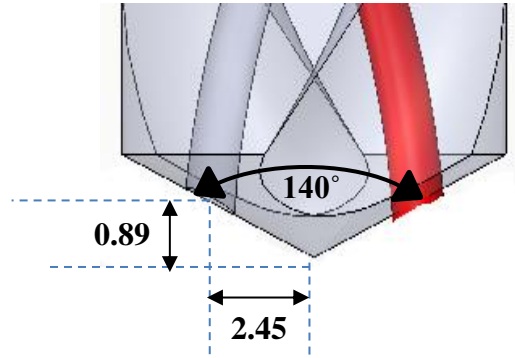
Figure 63. Schematic representation of drill specifications. Unit: mm

Part (a):

Distance between drill centre and glass slide = 84 mm

Distance between drill projection point and the centre of droplet zone = 25.6 mm

Let the distance between coolant hole centre and glass slide be denoted as z_{84}.

Vertical distance between drill centre and coolant hole centre was calculated using point angle as follows (Figure 63):

$$\left(2.45 \times tan\left(\frac{180 - 140}{2}\right)\right) = 0.89 \ mm$$

$$z_{84} = 84 + 0.89 = 84.89 \ mm \tag{13}$$

Cone angle β_{84} calculation:

$$\beta_{84} = \ tan^{-1}\left(\frac{25.6}{84.89}\right) = 16.78° \approx 17° \tag{14}$$

Part (b):

Distance between drill centre and glass slide = 107 mm

Distance between drill projection point and the centre of droplet zone = 30.5 mm

The distance between the coolant hole centre and glass slide z_{107} was calculated as follows:

$$z_{107} = 107 + 0.89 = 107.89 \, mm \tag{15}$$

Cone angle β_{107} calculation:

$$\beta_{107} = tan^{-1}\left(\frac{30.5}{107.89}\right) = 15.78° \approx 16° \tag{16}$$

The cone angle was about 16° in both the cases, which was about half of the 30° helix angle of the drill.

Droplet zone coverage angle calculation:

In addition to the cone angle β, droplet zone coverage angle φ was calculated when the distance between the drill tip and the glass panel was 84 and 107 mm. The droplet zone coverage angle was used to predict the resultant flow pattern. If the droplet zone coverage angle would be constant with varying distance between the drill and glass panel, the resultant flow could follow a linear path. These results can further be utilized to validate simulation results.

Part (a):

Distance between drill centre and glass slide = 84 mm

Droplet zone diameter = 49 mm

$$\tan \beta = \frac{\left(\frac{g}{2}\right) + e}{z_{84}} \tag{17}$$

$$\tan 16.78° = \frac{\left(\frac{49}{2}\right) + e}{84.89}$$

$$e = 1.097 \; mm$$

$$\tan \left(\frac{e}{z_{84}}\right) = \phi \tag{18}$$

$$\phi = 0.74°$$

$$\tan(\varphi + \phi) = \frac{g + e}{z_{84}} \tag{19}$$

$$\tan(\varphi + 0.74) = \frac{49 + 1.097}{84.89}$$

$$\varphi = 29.80°$$

Part (b):

Distance between drill centre and glass slide = 107 mm

Droplet zone diameter = 55.14 mm

$$\tan \beta = \frac{\left(\frac{g}{2}\right) + e}{z_{107}} \tag{20}$$

$$\tan 15.78° = \frac{\left(\frac{55.14}{2}\right) + e}{107.89}$$

$$e = 2.92 \; mm$$

$$\tan \left(\frac{e}{z_{107}}\right) = \phi \tag{21}$$

$$\phi = 1.55°$$

$$\tan(\varphi + \phi) = \frac{g + e}{z_{107}} \tag{22}$$

$$\tan(\varphi + 1.55) = \frac{55.14 + 2.92}{107.89}$$

$$\varphi = 26.73°$$

Thus, the droplet zone coverage angle is about 30° considering both the cases. To compare these droplet zone coverage angle with channel helix angle, following calculations were performed:

$$\tan(drill\ helix\ angle) = \frac{Circumference\ of\ the\ drill}{pitch\ of\ the\ drill} \tag{23}$$

$$\tan(30°) = \frac{\pi(10\ mm)}{pitch\ of\ the\ drill}$$

$$pitch\ of\ the\ drill = 54.41\ mm$$

Assuming the same pitch for the coolant channels, coolant channel helix angle can be estimated as follows:

$$\tan(channel\ helix\ angle) = \frac{\pi(4.9)}{54.41} \tag{24}$$

$$channel\ helix\ angle = 15.79°$$

The droplet zone coverage angle with the stationary drill was about half of the channel helix angle. The coverage angle was constant with the varying distance between the drill and the glass panel. Thus, the flow path resulting from the coolant channel would follow

a linear pattern. These results can be used to validate computational fluid dynamics simulation results.

4.5. Drilling of A380 die cast aluminium

4.5.1. Drilled hole quality

Actual drill diameter measurements are shown in Table 8. The actual drill size in case of dry drilling, flood cooling method, and MQL with Castrol oil was 7.995 mm and 7.996 mm with Coolube oil application.

Table 8. Drill diameters used with different cutting fluids

	Without coolant, TRIM MicroSol	Coolube oil	Castrol oil
Measured diameter (mm)	7.995	7.996	7.996
	7.996	7.997	7.995
	7.995	7.995	7.995
	7.994	7.996	7.995
	7.995	7.995	7.995
Average measured diameter (mm)	7.9950±0.0007	7.9958±0.0008	7.9952±0.0004

Cylindricity and hole diameter were studied to assess the hole quality with Coolube and Castrol oil (Zaimovic-Uzunovic and Lemes, 2018). The recommended milling parameters (Machinery Handbook, 29 ed., p. 1043) for A380 are: chip load 0.008-0.015 in/flute (0.20-0.38 mm/flute) and cutting speed 485-1905 ft/min (148-580 m/min). The

drilling parameters were chosen based on the milling information since no drilling

parameters are available. The cutting speed was chosen, so that all three machines can

operate at 10,000 rpm and at low chip load for assuring high hole quality.

Spindle speed:

$$N = \frac{V'}{\pi D'} = \frac{250 \ m/min}{\pi \frac{rad}{rev} \times 0.008 \ m} = 9{,}947 \ rpm \approx 9{,}950 \ rpm \tag{25}$$

Feed rate:

$$f_r = fnN = 0.20 \ \frac{mm}{flute} \times 2 \ \frac{flute}{rev} \times 9{,}950 \ \frac{rev}{min} = 3{,}980 \ mm/min \tag{26}$$

Drilling time:

$$t = \frac{0.5D' \tan\left(90° - \frac{\alpha}{2}\right) + d_p}{f_r} = \frac{0.5 \ (8 \ mm) \tan\left(90° - \frac{135}{2}\right) + 25 \ mm}{3{,}980 \ mm/min}$$

$$= 0.40 \ s \tag{27}$$

Where,

N: Spindle speed (rpm)

V': Cutting speed (m/min)

D': Drill diameter (mm)

f_r: Feed rate (mm/min)

f: Chip load (mm/flute)

n: Number of flutes per revolution (flute/rev)

123

t: Drilling time (s)

α: Included angle of drill (°)

d_p: Part thickness (mm)

Hole oversize and cylindricity was defined as follows:

Hole oversize = (measured hole diameter) - (measured drill size) (28)

Cylindricity = radial deviation of all circles on a right cylinder (29)

Cylindricity and hole diameter of drilled holes can also be attributed to various factors, such as BUE formation, thermal distortion of workpiece and the drill. According to Tai et al. (2012), the thermal distortion of Al 6061-T6 workpiece in MQL deep-hole drilling can be up to 61 μm. Instability and vibration induced in drilling can highly impact on hole quality (Aized & Amjad, 2013; Kaplan et al., 2015; S. A. Khan et al., 2017). Thermal distortion of the drill can also lead to oversized holes and increased depth of drilled holes (Bono & Ni, 2001).
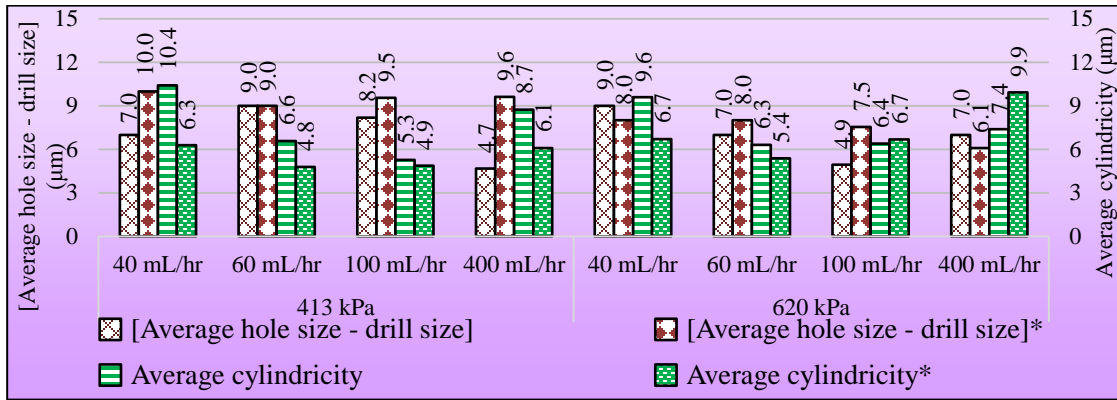
(a) Coolube oil
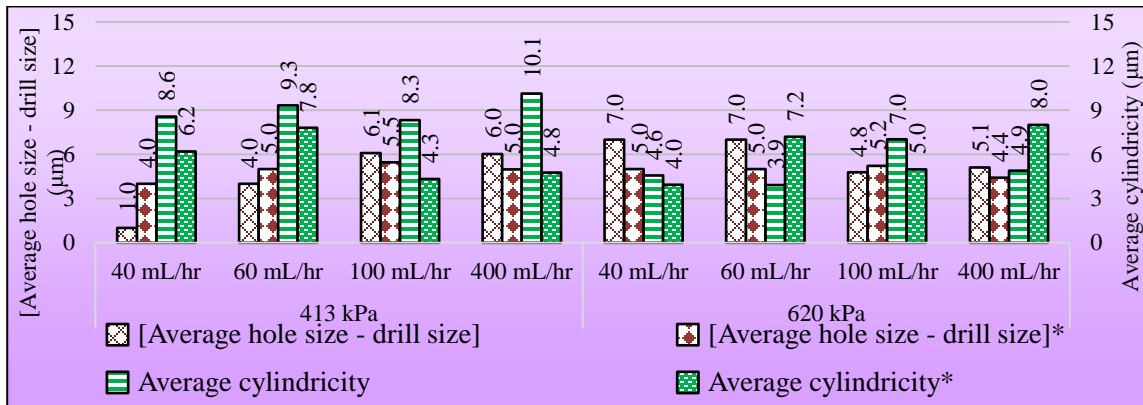
(b) Castrol oil

Figure 64. **Average hole size deviation from drill size and average cylindricity for different oils at different air pressures and oil flow rate.**

(*: The second bar represents the repeated result for the specific oil)
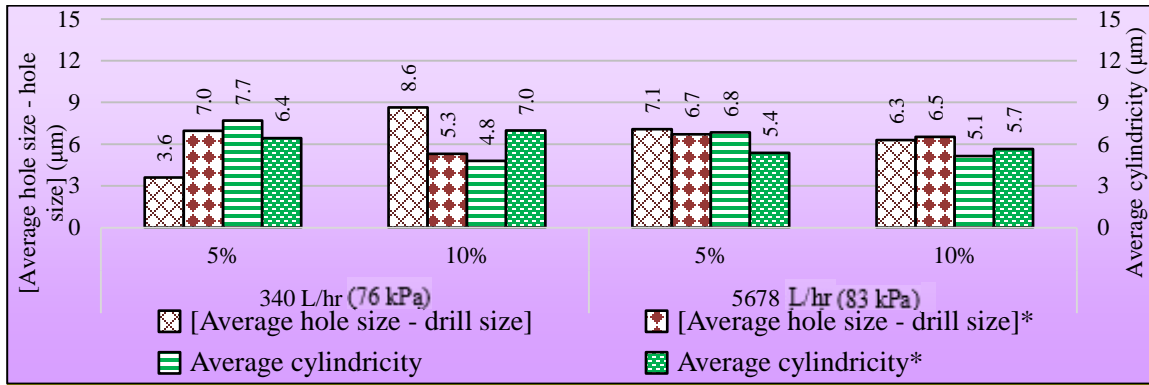
(c) TRIM MicroSol
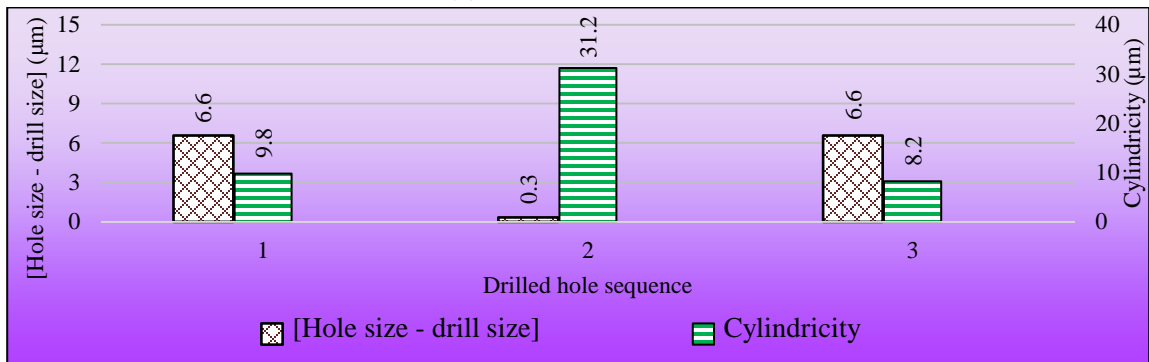
(d) No lubricant (dry drilling)
Figure 64. Continued

During dry drilling, the drill was broken after three holes. This was caused due to overheating of the tool and significant frictional forces generated at the tool-workpiece interface. Figure 64 shows the results obtained for average cylindricity and deviation of average hole size from the actual drill size when the lubricant was supplied with MQL, flood cooling method at different air pressures and oil flow rates, and in case of no lubricant.

- In Figure 64(a) (Coolube oil), the average hole size deviation from the actual tool diameter was greater than 6 µm for almost all the experiments. It did not show much variation with varying air pressures and oil quantity. It was concluded that

126

applying the excessive amount of lubricant (100 and 400 mL/hr) did not improve the hole quality.

- Figure 64(b) (Castrol oil) showed that the average hole size deviation was less than 6 µm in most of the cases. The average cylindricity values obtained with high oil flow rate did not vary much from those obtained with low oil flow rate. The application of more Castrol oil did not improve the hole quality, similar to Coolube oil cases.

- Figure 64(c) (TRIM MicroSol) implied that the average hole size deviation was about 6 µm considering all the cases of flood coolant application. Larger flow rate of flood coolant (5678 L/hr) resulted in more consistent data in terms of hole size and average cylindricity. There was no significant difference in the hole quality due to change in the lubricant concentration. The flood coolant application, however, can offer better control of thermal distortion of workpiece and the tool.

- Figure 64(d) (dry drilling) consists of the hole size deviation and cylindricity values for the three drilled holes without lubricant. The most non-uniform and larger values of hole size deviation and cylindricity were seen for this case as compared to the other cases.

These differences may be due to the variation of 3 different machines in this study.
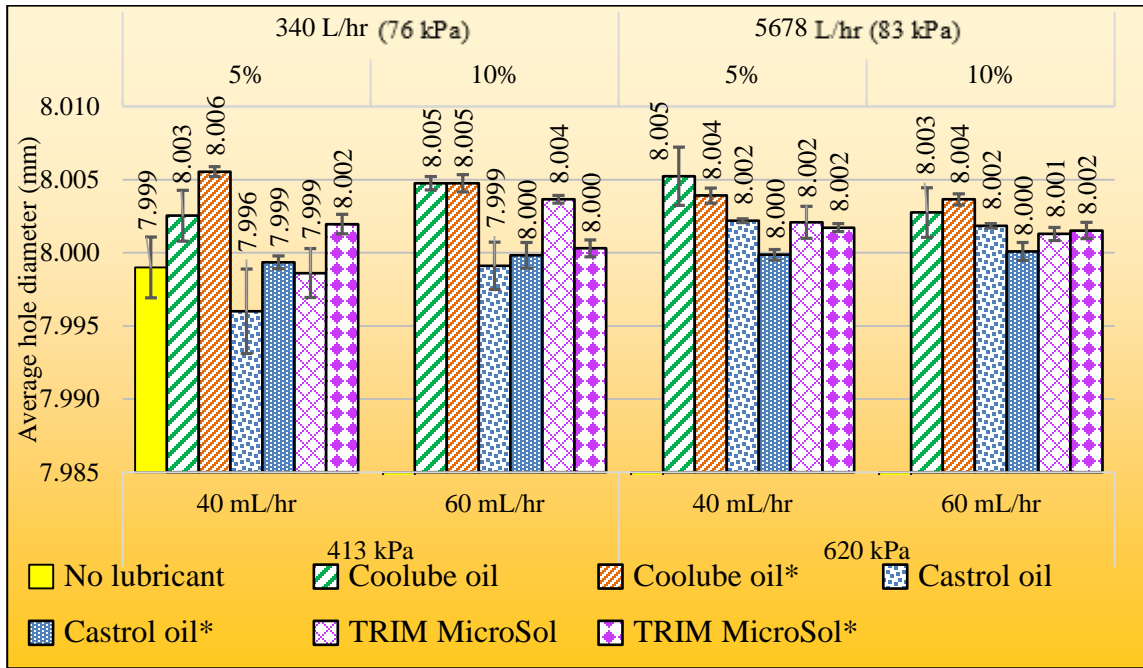
(a) Average hole diameter
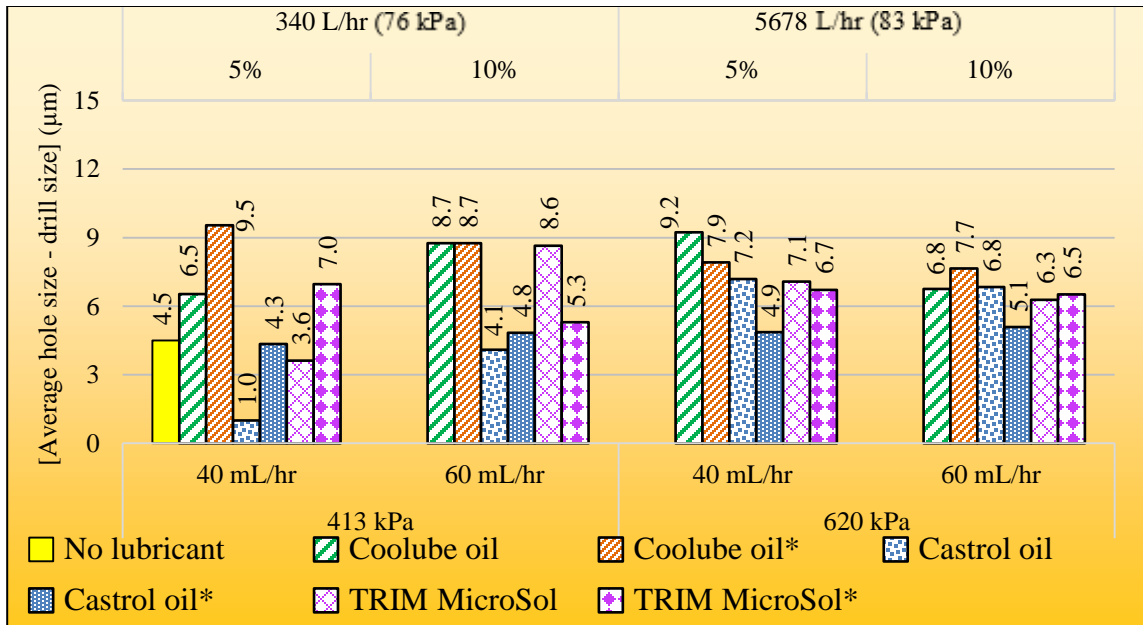
(b) Deviation of average hole diameter from actual drill diameter

Figure 65. Hole quality assessment with dry drilling, flood cooling, and MQL application (lower oil flow rate) (*: The second bar represents the repeated result for the specific oil)

128
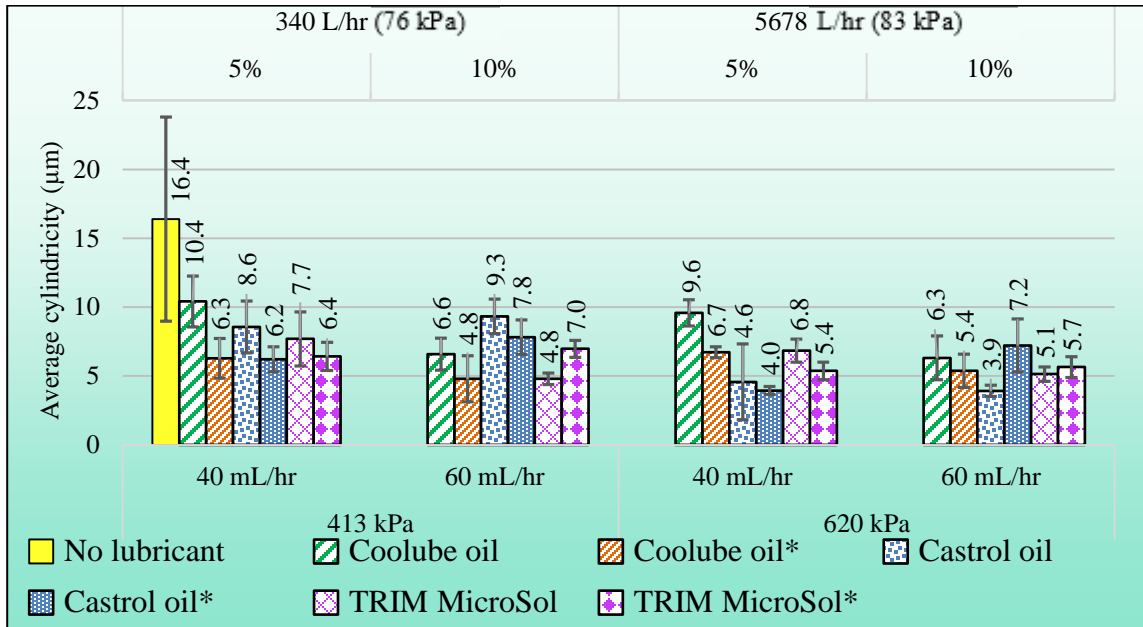
(c) Average cylindricity

Figure 65. Continued

- **Figure 65**(a) shows the average hole sizes obtained with dry drilling, MQL application, and flood cooling. The standard error bars are shown for each case. **Figure 65**(b) shows the deviation of the average hole sizes from the actual drill sizes in each case. **Figure 65**(c) shows the average cylindricity plot extracted from the data obtained with dry drilling, flood cooling and MQL application.

- With dry drilling method, the average hole diameter was larger than the actual drill diameter by 4.5 µm (**Figure 65**(b)). Castrol oil application resulted in more uniform hole size deviation than Coolube oil. The most uniform hole size deviation was observed with flood cooling method at higher flow rate of 5678 mL/hr.

- The average cylindricity with dry drilling was maximum, i.e., 16 µm (**Figure 65**(c)). With all other lubrication methods, the average cylindricity values were significantly (~8 µm) lower.
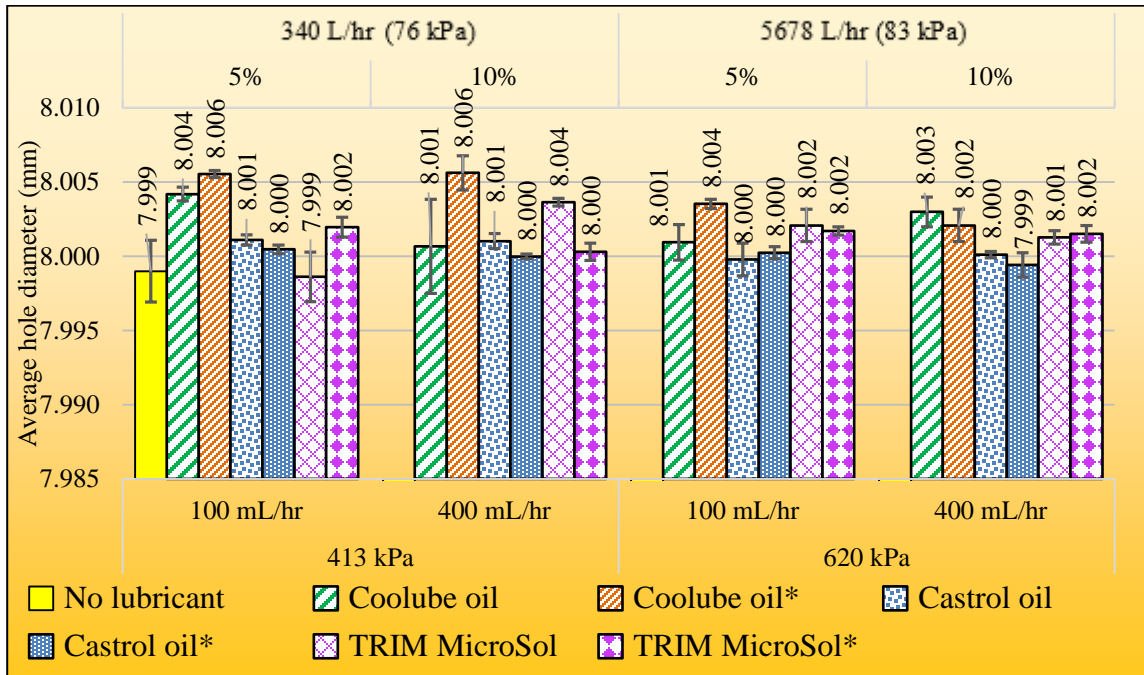
(a) Average hole diameter

Figure 66. Hole quality assessment with dry drilling, flood cooling, and MQL application (higher oil flow rate)
(*: The second bar represents the repeated result for the specific oil)
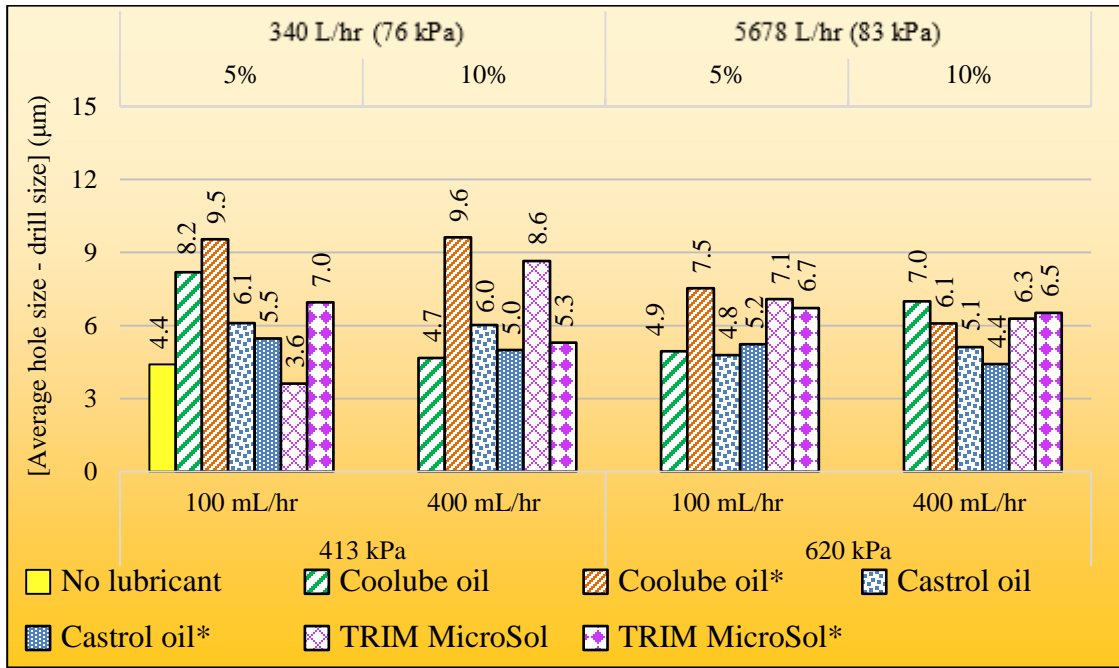
(b) Deviation of average hole diameter from the actual drill diameter
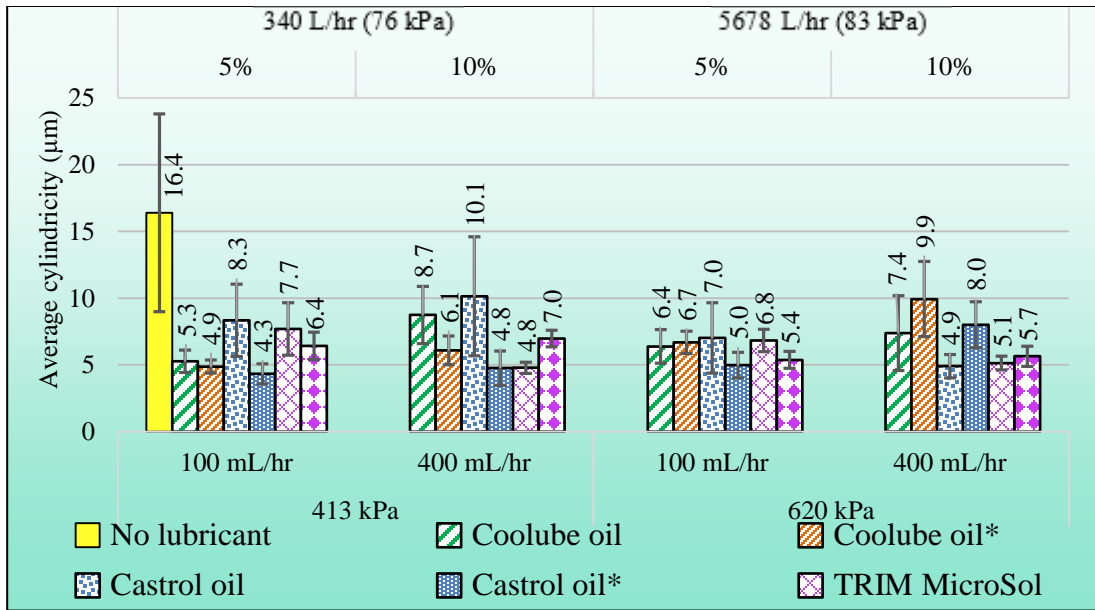
(c) Average cylindricity

Figure 66. Continued

131

- **Figure 66**(a) shows the average hole sizes obtained with dry, MQL, and flood cooling methods. In this case, MQL had 100 and 400 mL/hr oil flow rates. **Figure 66**(b) shows the deviation of average hole sizes from the drill sizes. With Castrol oil, the hole size deviation was smaller and more uniform as compared to that of Coolube oil (**Figure 66**(b)). At higher flow rate of the flood coolant, hole size deviation was the most uniform as compared to other cases.

- **Figure 66**(c) shows the comparison for average cylindricity values with dry, flood cooling and MQL methods. The average cylindricity was the most uniform with flood coolant at 5678 L/hr flow rate and 10% concentration.

Regression analysis was performed to investigate the impact of oil quantity and input air pressure on the average cylindricity and hole diameters. However, the p-values obtained were not smaller than 0.05 in almost all the cases. Also, the R-square values for the linear models were less than 10%. However, from the regression equations (30)-(35), it can be observed that oil flow rate shows slightly greater impact on these values as compared to air pressure. The regression analysis results for different lubrication methods are listed below:

For Coolube oil:

$$H_o = 10.90 - 4.81 \times 10^{-3} A_p - 3.85 \times 10^{-3} O_q \tag{30}$$
$$C_y = 4.99 + 2.86 \times 10^{-3} A_p + 3.57 \times 10^{-3} O_q \tag{31}$$

For Castrol oil:

$$H_o = 0.75 + 6.73 \times 10^{-3} A_p + 2.13 \times 10^{-3} O_q \tag{32}$$
$$C_y = 11.01 - 9.33 \times 10^{-3} A_p + 2.31 \times 10^{-3} O_q \tag{33}$$

132

For TRIM MicroSol (flood coolant):

$$H_o = 5.20 + 9.8 \times 10^{-5}\, F_f + 0.119\, C_c \tag{34}$$

$$C_y = 7.94 - 1.35 \times 10^{-4} F_f - 0.189\, C_c \tag{35}$$

Where,

H_o: hole oversize (µm)

C_y: cylindricity (µm)

A_p: air pressure (kPa)

O_q: oil quantity (mL/hr)

F_f: flood coolant flow (L/hr)

C_c: coolant concentration in water (%).

The data were affected by testing on different machines with different rigidity, accuracy, repeatability, and spindle runout. Any variation of machine tool conditions could invalid the above assumptions and affect measurement results of the drilled holes. It is also recommended that at least 3-level experiment with pressure values should be performed for drilling.

The regression model to predict the hole oversize and cylindricity based on oil quantity and air pressure as the only input parameters was non-conclusive. Generally, hole undersize was expected due to tool wear. However, tool runout and accuracies of machines resulted in hole oversize, instead of hole undersize when drilling A380 Al block. A better statistical model should include tool runout and accuracies of CMM and CNC as additional input parameters predict hole oversize and cylindricity.
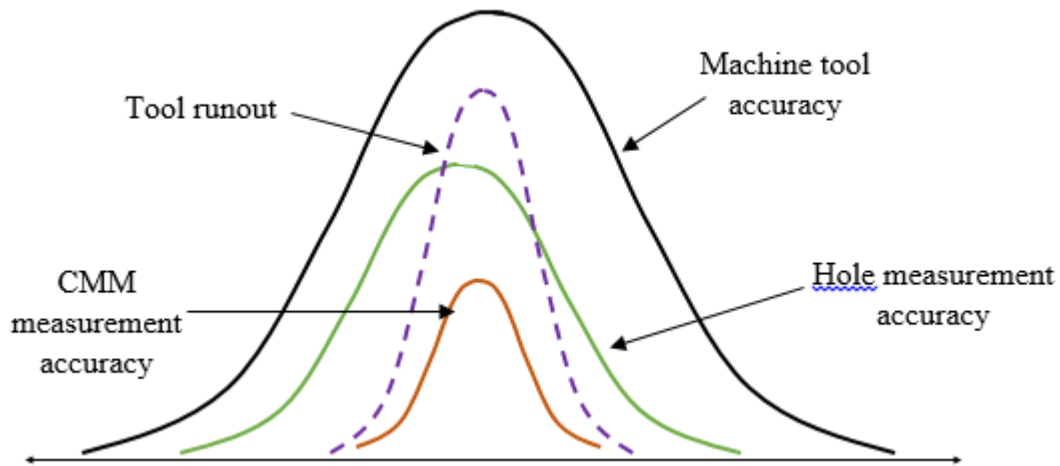
Figure 67. Schematic for accuracy comparison of CMM, CNC, hole measurements, and tool runout

Drilled hole diameters showed hole oversize when compared with the actual drill diameters. This can be attributed to combined effects of air pressure, oil quantity, tool runout, repeatability of three distinct CNC machines, and CMM. Hole oversize indicated that there could have been considerable tool runout, which should have been considered as one of the input parameters when generating the statistical model based on the collected data. In addition, the repeatability of positioning of an axis for HAAS VF2 was 5 μm and that of GROB CNC and FANUC Robodrill was 6 μm (G550 - GROB-WERKE GmbH & Co. KG; Haas accuracy; ROBODRILL α-DiB5 series). The CMM positioning error for TP200 probe was calculated as ±1.932 μm from the product data sheet using 8 mm drill size as measured length (Mitutoyo Product Details CNC CMM, CRYSTA-Apex S 7106). Hole oversize and cylindricity showed a deviation of up to 4 μm when drilling experiment was replicated with the same oil quantity and air pressure. The CMM was able to capture the hole oversize and cylindricity deviation up to 4 μm due to its smaller positioning error

134

as compared to the CNC machines. Thus, repeatability of three distinct CNC machines and CMM, and tool runout effects should be considered for a reliable statistical model of hole oversize and cylindricity along with air pressure and oil quantity.

4.5.2. Tool edge

Figure 68 - Figure 70 show the drill profile after drilling holes in the A380 aluminium plate. The tool used after flood cooling and dry drilling was not scanned since it was broken and embedded into the partially drilled hole. Microscopic examination shows wear on one of the cutting flutes after drilling with Coolube oil. Abrasive wear of the drill on one flute might be caused by tool defect rather than normal tool wear in drilling since the other flute remains sharp after all tests. It may cause imbalance and affect the hole oversize and cylindricity. Significant BUEs near the drill center were seen after drilling with Castrol oil. Generally, BUEs form on cutting tools, especially, at the drill center when machining soft materials such as aluminium at low cutting speed. Minimum BUEs were seen on the drill lubricated with Coolube oil. Lack of BUEs on tool with Coolube oil could be due to the effective lubrication of this oil, due to its smaller contact angle on aluminium as compared to Castrol oil.
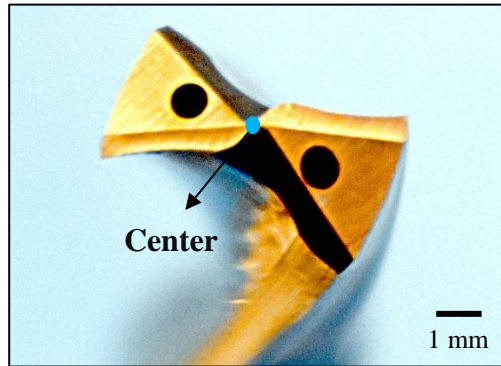
Figure 68. Drill (8 mm diameter)
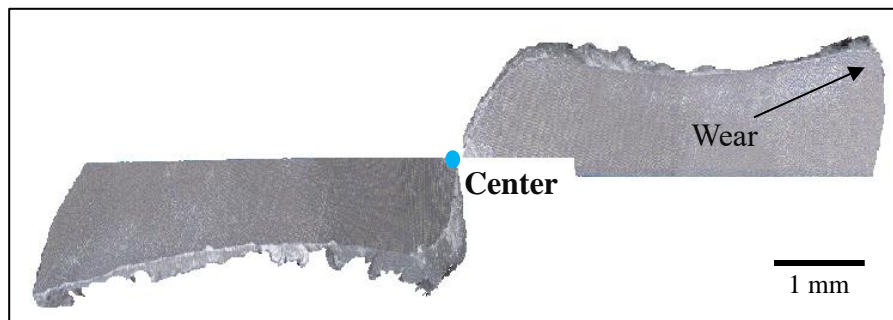
Figure 69. Drill edge profile after drilling with Coolube oil
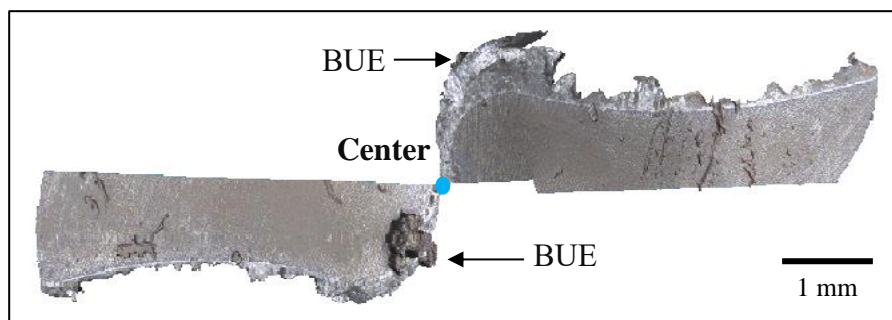
Figure 70. Drill edge profile after drilling with Castrol oil

CHAPTER 5

CONCLUSIONS AND RECOMMENDATIONS

Characterization and formation of internal MQL system droplets was studied with through-tool coolant channels of solid carbide twist drills. Effect of internal MQL system in drilling A380 die cast aluminium was investigated. This study showed:

1) Input air pressure and through-tool coolant channel sizes affected airborne droplet sizes of lubricant. Both air pressure and circular coolant channel size were inversely proportional to the airborne droplet sizes. The smallest airborne diameter was 5 μm for Coolube oil with 8 mm drill at 551 and 689 kPa air pressure.

2) Highly viscous Castrol oil required higher air pressure to form the mist. High-speed videos showed the high tendency of Castrol oil sticking to the drill tip as compared to the low viscous Coolube oil. MQL using higher viscosity oil resulted in large diameter droplets for both sizes of coolant channel.

3) BUEs at the drill centre with Castrol oil were considerable than those with Coolube oil. Castrol oil, with greater contact angle and high viscosity, might not provide effective lubrication to the cutting zone.

4) Excessive oil supply did not improve hole quality with both oils. Thus, hole quality can be improved by an optimal oil supply and essential air flow rate.

5) The aerosol jet stream resulting from the coolant channels of the drill was diverted at an outward angle instead of following a path parallel to the drill axis. The constant droplet zone coverage angle with varying distance between glass panel

and drill implied that the resultant flow from the channel can follow a linear path, which can be used to validate simulation results.

6) The regression model for hole sizes and cylindricity based on oil quantity and air pressure was non-conclusive. An ideal model should include additional parameters such as tool runout, machine tool accuracies, and CMM accuracy.

Future works:

a) To reduce data variation due to different machine rigidity and accuracy, test all oils on one CNC machine.

b) To find the effectiveness of internal MQL, drill high aspect ratio holes on more challenging materials such as stainless steel or Inconel.

c) This study studied contact angle on workpiece material. Inspect the contact angles of lubricants on the tool material, which can explain how lubricants flow and spread inside the coolant channels of the drill.

d) Study the effect of surface roughness of coolant channels of the twist drill on micromist formation in MQL. A rough solid surface induces turbulent air flow, therefore, affects the droplet size.

e) Study the droplet formation and flow with straight coolant channels, i.e., $0°$ channel helix angle.

REFERENCES

Aized, T., & Amjad, M. (2013). Quality improvement of deep-hole drilling process of

    AISI D2. *International Journal of Advanced Manufacturing Technology*, *69*(9–12),

    2493–2503. https://doi.org/10.1007/s00170-013-5178-4

Barnes, S., & Pashby, I. R. (2000). Through-tool coolant drilling of aluminum/SiC metal

    matrix composite. *Journal of Engineering Materials and Technology, Transactions*

    of the ASME, *122*(4), 384–388. https://doi.org/10.1115/1.1288925

Bono, M., & Ni, J. (2001). The effects of thermal distortions on the diameter and

    cylindricity of dry drilled holes. *International Journal of Machine Tools and*

    Manufacture, *41*(15), 2261–2270. https://doi.org/10.1016/S0890-6955(01)00047-5

Braga, D. U., Diniz, A. E., Miranda, G. W. A., & Coppini, N. L. (2002). Using a

    minimum quantity of lubricant (MQL) and a diamond coated tool in the drilling of

    aluminum-silicon alloys. *Journal of Materials Processing Technology*, *122*(1),

    127–138. https://doi.org/10.1016/S0924-0136(01)01249-3

Coolube 2210 Al SDS. (n.d.). https://unist.com/uploads/SDS/SDS_Coolube_2210AL.pdf

Dasch, J. M., & Kurgin, S. K. (2010). A characterisation of mist generated from

    minimum quantity lubrication (MQL) compared to wet machining. *International*

    Journal of Machining and Machinability of Materials, *7*(1–2), 82–95.

    https://doi.org/10.1504/IJMMM.2010.029847

Fachausschuss Information Sheet No. 006. (2005). *Low-emitting metal working with*

    minimum quantity lubrication.

Furness, R., Company, F. M., & Stoll, A. (2006). *Minimum quantity lubrication (MQL)*

machining for complex powertrain components.

https://asmedigitalcollection.asme.org/MSEC/proceedings-

pdf/MSEC2006/47624/965/2659649/965_1.pdf

G550 - GROB-WERKE GmbH & Co. KG. (n.d.). Retrieved October 17, 2020, from

https://www.grobgroup.com/en/products/product-range/universal-machining-

centers/milling-centers/g550/

Haas accuracy. (n.d.). Retrieved October 17, 2020, from

https://www.practicalmachinist.com/vb/haas/haas-accuracy-216158/

Hughey, E., & Stephenson, D. A. (2019). Oil delivery balancing and priming for multi-

diameter minimum quantity lubrication tooling assemblies. *Procedia

Manufacturing*, *34*, 343–348. https://doi.org/10.1016/j.promfg.2019.06.172

Hyspray A 1536 SDS. (n.d.). https://thelubricantoracle.castrol.com/product/hyspray-a-

1536/industrial/en-US

Item # D8TFR-15-1, Hot Plate On Waage Electric, Inc. (n.d.). Retrieved August 29,

2020, from http://waage.thomasnet.com/item/band-tubular-and-strip-heaters/hot-

plate/d8tfr-15-1

James, G., Witten, D., Hastie, T., & Tibshirani, R. (2017). *An introduction to statistical

learning: With applications in R*. https://doi.org/10.1007/978-1-4614-7138-7

Kadirgama, K., Noor, M. M., Abou-El-Hossein, K. A., Habeeb, H. H., Rahman, M. M.,

Mohamad, B., & Bakar, R. A. (2010). Effect of dry cutting on force and tool life

when machining aerospace material. *World Academy of Science, Engineering and

Technology*, *71*(11), 452–456.

Kajaria, S. (2009). Modeling of tool life and micro-mist flow for effective micro-machining of 316L stainless steel. *Thesis, Texas A&M University*, 115–119.

Kao, Y. T., Takabi, B., Hu, M., & Tai, B. L. (2017). Coolant channel and flow characteristics of MQL drill bits: Experimental and numerical analyses. *ASME 2017 12th International Manufacturing Science and Engineering Conference, MSEC 2017 Collocated with the JSME/ASME 2017 6th International Conference on Materials and Processing*, *2*, 1–7. https://doi.org/10.1115/MSEC2017-3060

Kaplan, Y., Motorcu, A. R., Nalbant, M., & Okay, Ş. (2015). The effects of process parameters on acceleration amplitude in the drilling of cold work tool steels. *International Journal of Advanced Manufacturing Technology*, *80*(5–8), 1387–1401. https://doi.org/10.1007/s00170-015-7097-z

Khan, S. A., Nazir, A., Mughal, M. P., Saleem, M. Q., Hussain, A., & Ghulam, Z. (2017). Deep hole drilling of AISI 1045 via high-speed steel twist drills: evaluation of tool wear and hole quality. *International Journal of Advanced Manufacturing Technology*, *93*(1–4), 1115–1125. https://doi.org/10.1007/s00170-017-0587-4

Khan, W. A., Hoang, N. M., Tai, B., & Hung, W. N. P. (2018). Through-tool minimum quantity lubrication and effect on machinability. *Journal of Manufacturing Processes*, *34*(March), 750–757. https://doi.org/10.1016/j.jmapro.2018.03.047

Kovvuri, V., Wang, Z., Araujo, A., Da Silva, M. B., Bukkapatnam, S., & Hung, W. N. P. (2015). *Built-Up-Edge Formation In Micromilling*. https://asmedigitalcollection.asme.org/IMECE/proceedings-pdf/IMECE2015/57359/V02AT02A057/2492078/v02at02a057-imece2015-

53390.pdf

Kumar, M. S., Prabukarthi, A., & Krishnaraj, V. (2013). Study on tool wear and chip

formation during drilling carbon fiber reinforced polymer (CFRP)/titanium alloy

(Ti6Al4V) stacks. *Procedia Engineering*, *64*, 582–592.

https://doi.org/10.1016/j.proeng.2013.09.133

Li, Q., Lerma, I., Alvarado, J., Edinbarough, I., & Hung, W. N. P. (2015).

Characterization of micromist for effective machining. *ASME International*

Mechanical Engineering Congress and Exposition, Proceedings (IMECE), *2A-*

2015. https://doi.org/10.1115/IMECE2015-53632

Li, R., Hegde, P., & Shih, A. J. (2007). High-throughput drilling of titanium alloys.

International Journal of Machine Tools and Manufacture, *47*(1), 63–74.

https://doi.org/10.1016/j.ijmachtools.2006.02.012

Lin, Q., Liu, P., Feng, Z., & Zhu, L. (2017). A review on fluid flow and heat transfer in

helical channel. *Chinese Science Bulletin*, *62*(25), 2931–2940.

https://doi.org/10.1360/N972016-01134

Liu, Z. Q., Cai, X. J., Chen, M., & An, Q. L. (2012). Selection of minimum quantity

lubrication (MQL) parameters in milling of Ti-6Al-4V. *Advanced Materials*

Research, *426*, 139–142. https://doi.org/10.4028/www.scientific.net/AMR.426.139

Madhukar, S., Shravan, A., Vidyanand, P., & Reddy, G. S. (2016). A Critical review on

Minimum Quantity Lubrication (MQL) Coolant System for Machining Operations.

International Journal of Current Engineering and Technology, *6*(5).

http://inpressco.com/category/ijcet

Marutho, D., Hendra Handaka, S., Wijaya, E., & Muljono. (2018). The Determination of Cluster Number at k-Mean Using Elbow Method and Purity Evaluation on Headline News. *Proceedings - 2018 International Seminar on Application for Technology of Information and Communication: Creative Technology for Human Life, ISemantic 2018*, 533–538. https://doi.org/10.1109/ISEMANTIC.2018.8549751

Minh Duc, T., The Long, T., & Van Thanh, D. (2020). Evaluation of minimum quantity lubrication and minimum quantity cooling lubrication performance in hard drilling of Hardox 500 steel using Al 2 O 3 nanofluid. *Advances in Mechanical Engineering*, *12*(2), 1–12. https://doi.org/10.1177/1687814019888404

Mitutoyo Product Details CNC CMM, CRYSTA-Apex S 7106. (n.d.). https://shop.mitutoyo.eu/web/mitutoyo/en/mitutoyo/$catalogue/mitutoyoData/PR/1 91-254- 10/datasheet.xhtml;jsessionid=DF9F87FA263A1FFEF6989ADACA9F7FF1

NCSS 2020 Statistical Software. (2020). NCSS, LLC. ncss.com/software/ncss

Nozzle Requirements Calculators. (n.d.). Retrieved April 22, 2020, from http://irrigation.wsu.edu/Content/Calculators/Sprinkler/Nozzle-Requirements.php

Okafor, A. C., & Nwoguh, T. O. (2020). A study of viscosity and thermal conductivity of vegetable oils as base cutting fluids for minimum quantity lubrication machining of difficult-to-cut metals. *International Journal of Advanced Manufacturing Technology*, *106*(3–4), 1121–1131. https://doi.org/10.1007/s00170-019-04611-3

Park, K. H., Olortegui-Yume, J., Yoon, M. C., & Kwon, P. (2010). A study on droplets and their distribution for minimum quantity lubrication (MQL). *International*

143

Journal of Machine Tools and Manufacture, *50*(9), 824–833.

https://doi.org/10.1016/j.ijmachtools.2010.05.001

Patil, A., Raval, J., Bangma, T., Edinbarough, I., Tai, B., Stephenseon, D., Suleiman, O., & Hung, W. N. (2020). Characterization and Performance of Minimum Quantity Lubricants in Through-Tool Drilling. *International Journal of Engineering Materials and Manufacture*, *5*(4), 98–115.

https://doi.org/10.26776/ijemm.05.04.2020.01

Rahim, E. A., & Sharif, S. (2006). Investigation of tool life and surface integrity when drilling Ti-6A1-4V and Ti-5A1-4V-Mo/Fe. *JSME International Journal, Series C: Mechanical Systems, Machine Elements and Manufacturing*, *49*(2), 340–345.

https://doi.org/10.1299/jsmec.49.340

Ramulu, M., Branson, T., & Kim, D. (2001). A study on the drilling of composite and titanium stacks. *Composite Structures*, *54*(1), 67–77. https://doi.org/10.1016/S0263-8223(01)00071-X

Raval, J. K., Kao, Y.-T., & Tai, B. L. (2019). Characterizing Mist Distribution in Through Tool Minimum Quantity Lubrication (MQL) Drills. *Journal of Manufacturing Science and Engineering*, 1–16. https://doi.org/10.1115/1.4045799

ROBODRILL α-DiB5 series High-performance vertical machining center Automated machining for more versatile milling, drilling and tapping. (n.d.).

Serv-O-Spray ™ Operation Manual. (2018). https://unist.com.au/wp-content/uploads/2018/03/Serv-O-Spray-Operation-Manual-2018-1.pdf

Sharon-Cutwell Co.,Inc. (n.d.). https://cutwell.com/

Sivalingam, V., Zan, Z., Sun, J., Selvam, B., Gupta, M. K., Jamil, M., & Mia, M. (2020). Wear behaviour of whisker-reinforced ceramic tools in the turning of Inconel 718 assisted by an atomized spray of solid lubricants. *Tribology International*, 106235. https://doi.org/10.1016/j.triboint.2020.106235

Star SU LLC. (n.d.). https://www.star-su.com/cutting-tools/gundrills/solid-carbide-twist-drills/

Stephenson, D. A., & Agapiou, J. S. (2016). *Metal Cutting Theory and Practice, Third Edition* (3rd ed.). CRC Press.

Stephenson, D. A., Hughey, E., & Hasham, A. A. (2019). Air flow and chip removal in minimum quantity lubrication drilling. *Procedia Manufacturing*, *34*, 335–342. https://doi.org/10.1016/j.promfg.2019.06.171

Sultana, M. N., Dhar, N. R., & Zaman, P. B. (2019). *A Review on Different Cooling / Lubrication Techniques in Metal Cutting-MQL*. *7*(4), 71–87. https://doi.org/10.11648/j.ajma.20190704.11

Sun, J., Wong, Y. S., Rahman, M., Wang, Z. G., Neo, K. S., Tan, C. H., & Onozuka, H. (2006). Effects of coolant supply methods and cutting conditions on tool life in end milling titanium alloy. *Machining Science and Technology*, *10*(3), 355–370. https://doi.org/10.1080/10910340600902181

Tai, B. L., Dasch, J. M., & Shih, A. J. (2011). Evaluation and comparison of lubricant properties in minimum quantity lubrication machining. *Machining Science and Technology*, *15*(4), 376–391. https://doi.org/10.1080/10910344.2011.620910

Tai, B. L., Jessop, A. J., Stephenson, D. A., & Shih, A. J. (2012a). Workpiece thermal

distortion in minimum quantity lubrication deep hole drilling-finite element modeling and experimental validation. *Journal of Manufacturing Science and Engineering, Transactions of the ASME*, *134*(1). https://doi.org/10.1115/1.4005432

Tai, B. L., Jessop, A. J., Stephenson, D. A., & Shih, A. J. (2012b). Workpiece thermal distortion in minimum quantity lubrication deep hole drilling-finite element modeling and experimental validation. *Journal of Manufacturing Science and Engineering, Transactions of the ASME*, *134*(1). https://doi.org/10.1115/1.4005432

Tang, L., Tang, Y., & Parameswaran, S. (2016). A numerical study of flow characteristics in a helical pipe. *Advances in Mechanical Engineering*, *8*(7), 168781401666024. https://doi.org/10.1177/1687814016660242

Venkatesh, V. C., & Xue, W. (1996). A study of the built-up edge in drilling with indexable coated carbide inserts. *Journal of Materials Processing Technology*, *58*(4), 379–384. https://doi.org/10.1016/0924-0136(95)02211-2

Walker, T. (2013). *The MQL Handbook - a guide to machining with minimum quantity lubrication*. 64.

Wang, Z., Kovvuri, V., Araujo, A., Bacci, M., Hung, W. N. P., & Bukkapatnam, S. T. S. (2016). Built-up-edge effects on surface deterioration in micromilling processes. *Journal of Manufacturing Processes*, *24*, 321–327. https://doi.org/10.1016/j.jmapro.2016.03.016

Zaimovic-Uzunovic, N., & Lemes, S. (2018). Cylindricity measurement on a coordinate measuring machine. *Lecture Notes in Mechanical Engineering*, *201519*, 825–835. https://doi.org/10.1007/978-3-319-68619-6_80

Zhang, P. F., Churi, N. J., Pei, Z. J., & Treadwell, C. (2008). Mechanical drilling processes for titanium alloys: A literature review. In *Machining Science and Technology* (Vol. 12, Issue 4, pp. 417–444). https://doi.org/10.1080/10910340802519379

APPENDIX A

IMAGE PROCESSING STEPS

Image processing steps including Adobe Photoshop version 6.0 and ImageJ 1.52a were as follows.

(a)   (b)
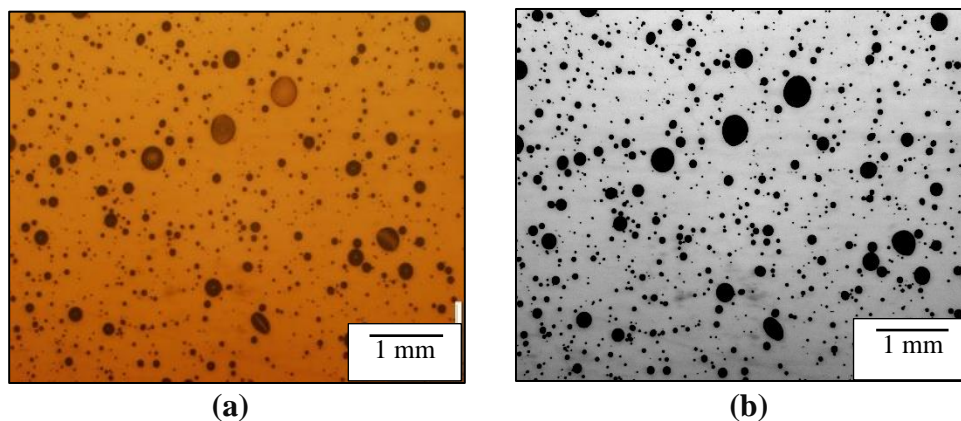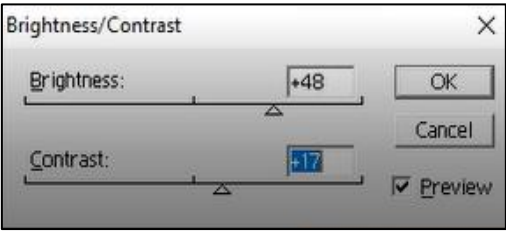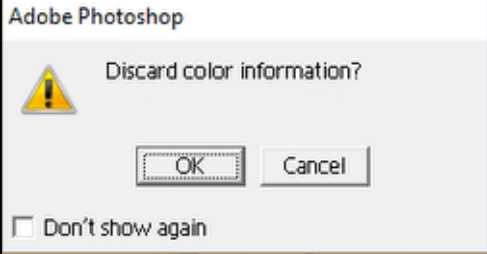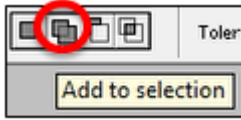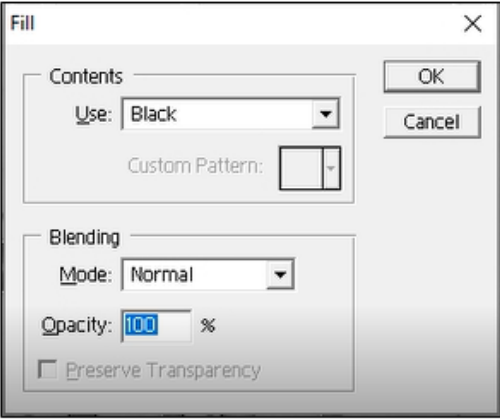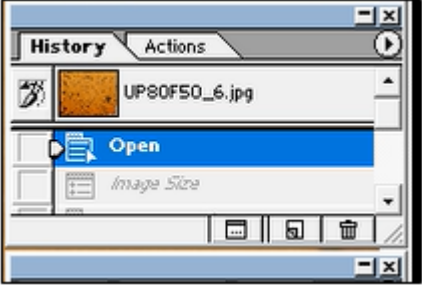
Figure 71. Microscopic images (a) before Adobe Photoshop processing; (b) after Adobe Photoshop processing
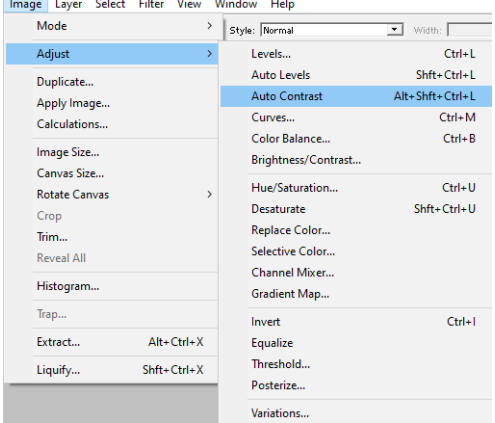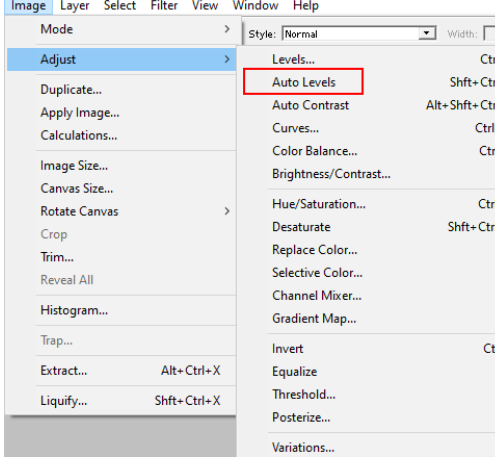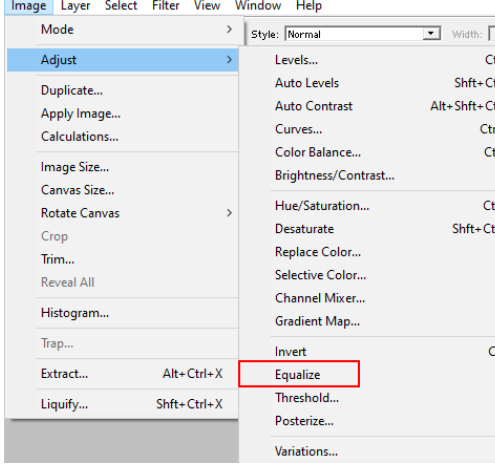
Adobe Photoshop version 6.0 procedure:
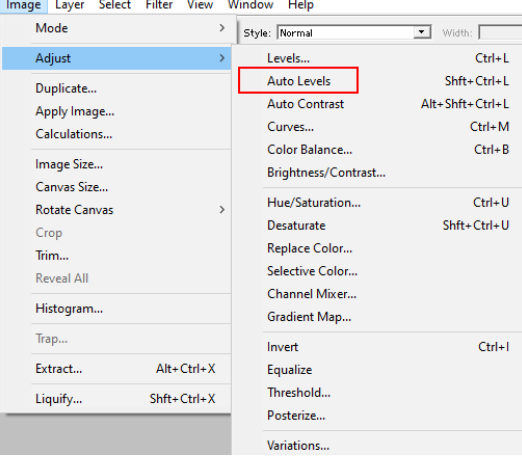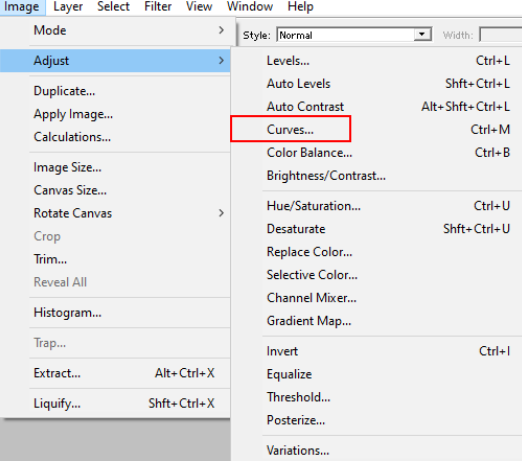
	Open the image in the software from File option and resize using Ctrl + + or Ctrl + - Image → Adjust → Brightness/Contrast Change the brightness and contrast in such a way that the software can identify all the boundaries for all the droplets in the image.
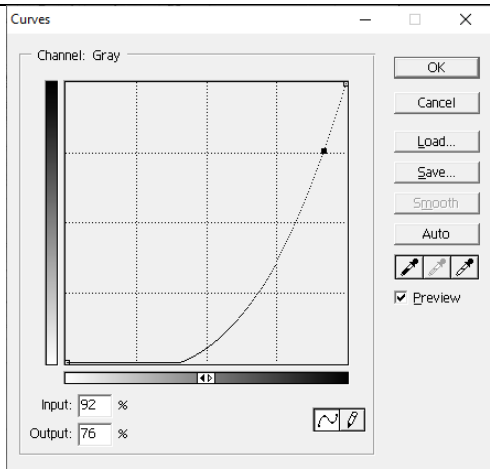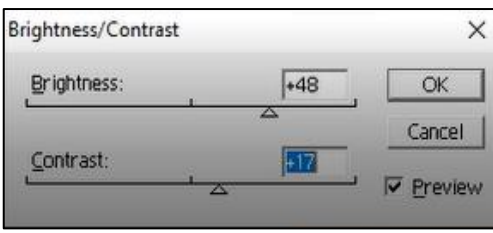
	Image → Mode → Grayscale → Accept discarding color information. Image becomes B&W.
	Select magic wand tool from the toolbox. Click on the portion of the image without droplets. When clicked on an area in the image with this tool, Photoshop identifies the tone and color of the area and selects pixels that share the same color and brightness values.
	Some portion of the image might not get selected because of the difference in the tone and color of the area which was selected. To add that portion of the image into the selection, click Add to Selection from the upper toolbox and select the remaining portion using magic wand tool. To select the droplets use Inverse command from Select menu from main toolbar.

	Edit → Fill → Black To completely fill the droplets, Fill command is used. In the Grayscale image form, select the Black color to fill the complete area of the droplets. To remove all the selections from the image, use Deselect option from Select menu.
	Until all the droplets are filled in, repeat the steps. This can be done by selecting the initial form of the image by going back in History panel and then repeating the steps. Here, by changing the brightness and contrast again, and repeating other steps, the final output can be improved.
	Crop → Drag (Select the required portion) → Accept the change When the image processing is done, crop the image eliminating the portion that has the scale for the image. Save the file.

Adobe Photoshop version 6.0 procedure for droplet zone boundary identification were as

follows:

	Open the image in the software from File option and resize using Ctrl + + or Ctrl + - Image → Adjust → Auto Contrast Brightness and contrast will be automatically adjusted.
	Image → Adjust → Auto Levels Auto Levels corrected the tonal adjustment in the image.
	Image → Adjust → Equalize Light areas turned white and dark areas to black. Repeat Auto Contrast step if required.

	Image → Mode → Grayscale → Accept discarding color information. Image becomes B&W.
	Repeat Auto Contrast and Auto Levels step as required.
	Image → Adjust → Curves Select curves option for tonal adjustments of B&W image.

152

Curves — □ × Channel: Gray Input: 92 % Output: 76 % OK Cancel Load... Save... Smooth Auto ☑ Preview	Drag the curve to different positions for tonal adjustments. Note the Input and Output value for batch processing.
Brightness/Contrast × Brightness: +48 Contrast: +17 OK Cancel ☑ Preview	Image → Adjust → Brightness/Contrast Change the brightness and contrast such that most droplets will be highlighted. Repeat Auto Contrast and Auto Levels steps if required.

ImageJ procedure for airborne diameters:

(a)   (b)
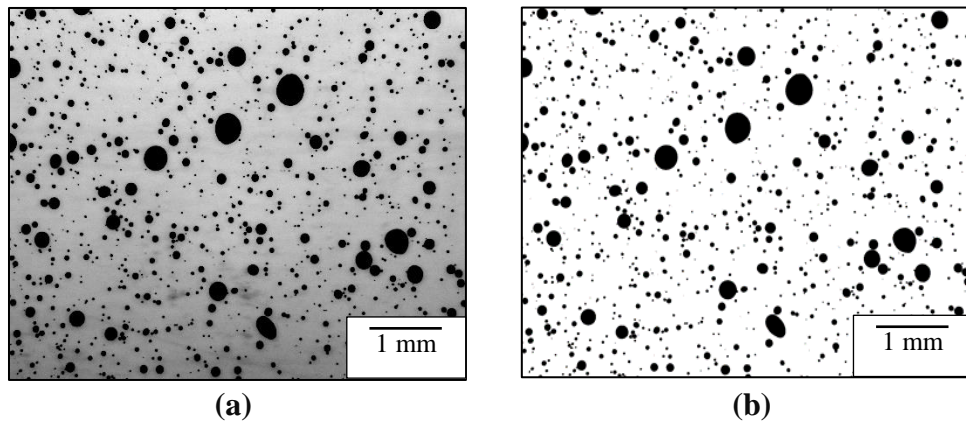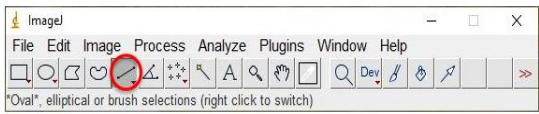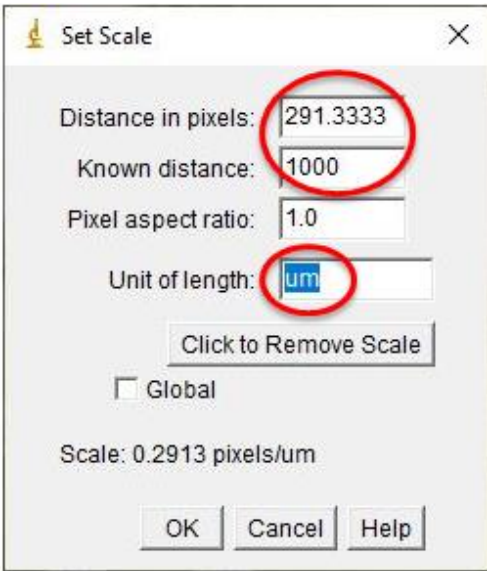
Figure 72. Microscopic images (a) before ImageJ processing; (b) after ImageJ processing

153

	To open the microscopic image in the software, select open from File menu. From the ImageJ window, select the line option.
	Using line command, draw a line on the scale bar of chosen microscopic image.
	Analyze → Set scale ImageJ software calculates the length of the line drawn in step 3 and shows it in the Distance in pixels box of the Set scale window. Known distance is the value scale in microscopic image, which was 1 mm, i.e., 1000 µm. Unit of length was µm.
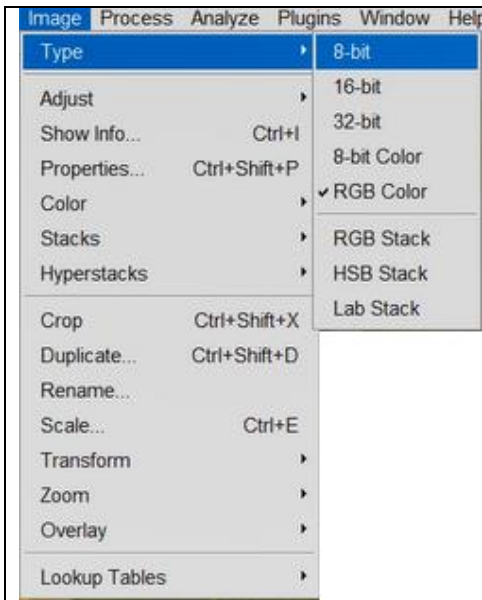
	Open the image processed in Adobe Photoshop from File menu. Convert image to 8-bit image.
	Image → Type → 8-bit
	Go to the threshold option as follows - Image → Adjust → Threshold
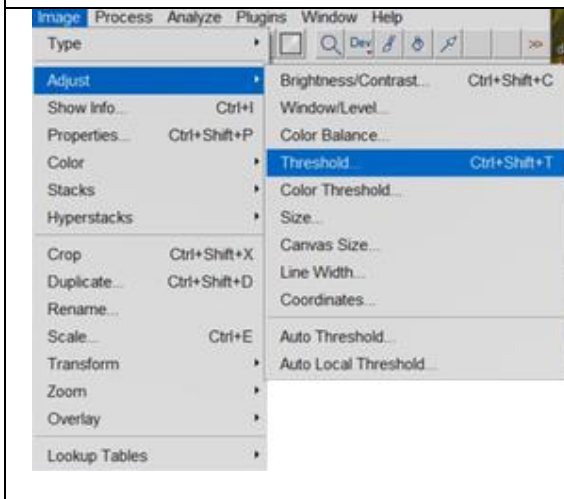
155
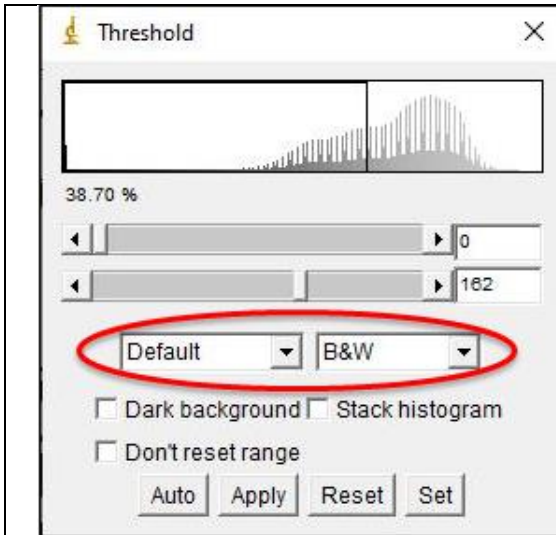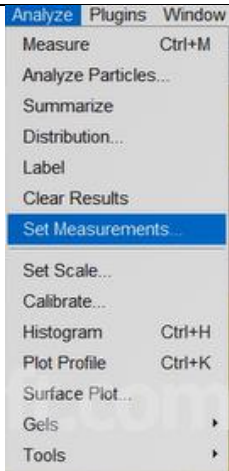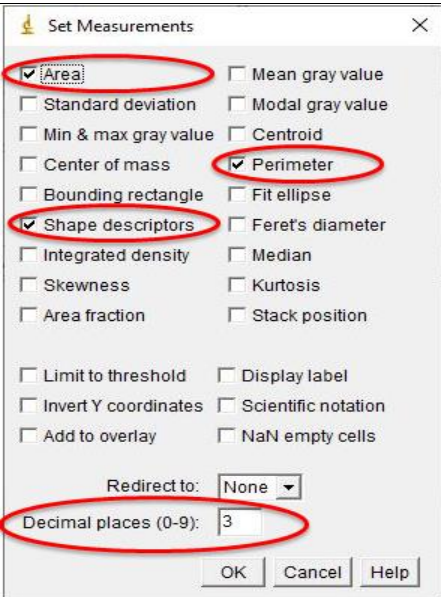
	Threshold was adjusted using the Default method and B&W option.
	Process→Binary→Watershed Watershed separates merged droplets.
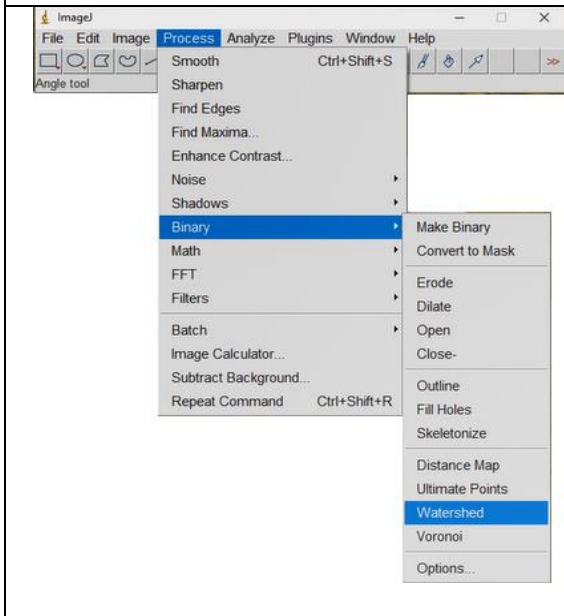
	Required set of measurements was selected for the final result display. Analyze → Set Measurements
	Area, shape descriptors, perimeter, area fraction were selected along with the decimal place limit as 3.
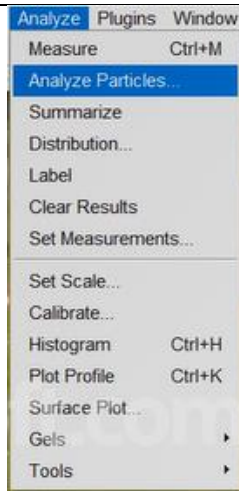
	To calculate droplet areas, Analyze → Analyze Particles
	In Analyze Particles window, the Exclude on edges option was elected to avoid half-cut droplets present at the edges of the image.
	From the Results window, use Save as from File menu, to save the final results.
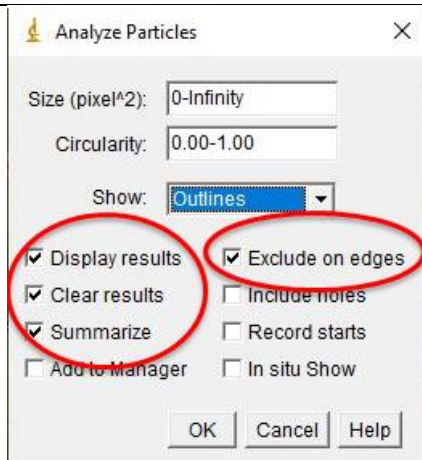
APPENDIX B

CMM PROCEDURE

References: Mitutoyo MCOSMOS C1 CMM Software overview (1st edition) and

Mitutoyo Bolt circle pattern measurement by GeoPak. Following procedure was used to

measure cylindricity and hole size of drilled holes in A380 aluminium plate.
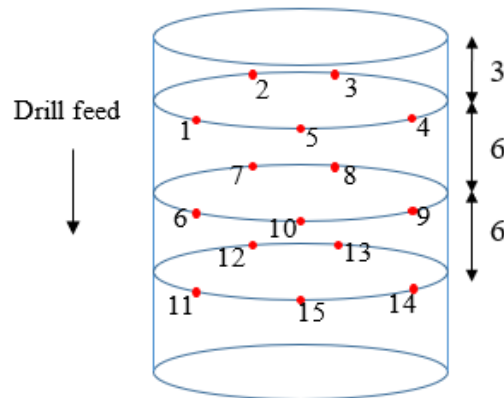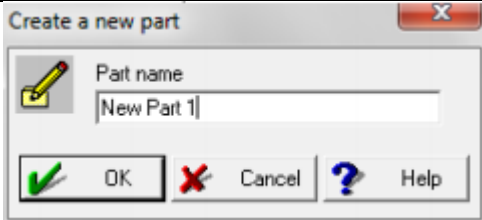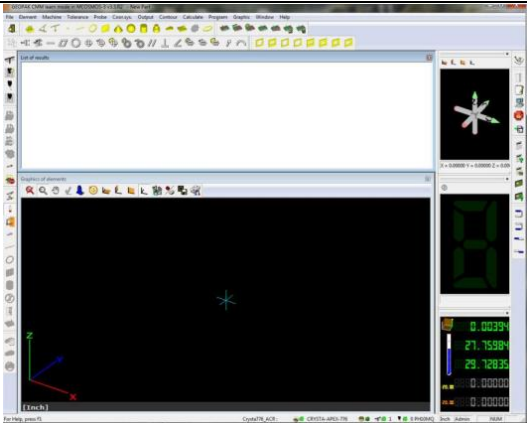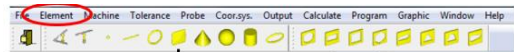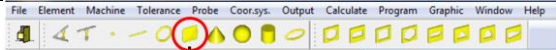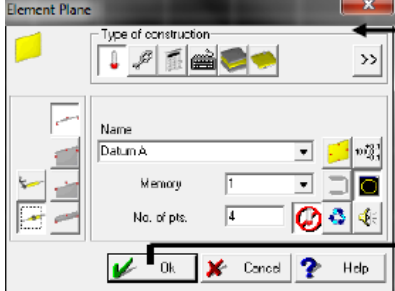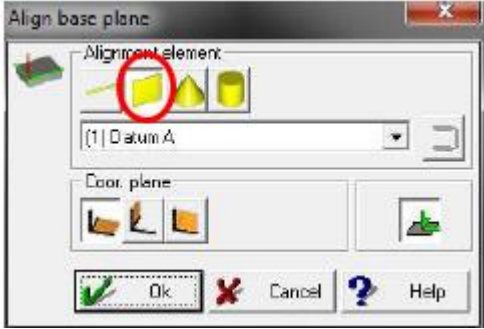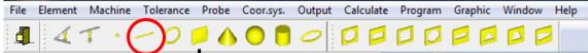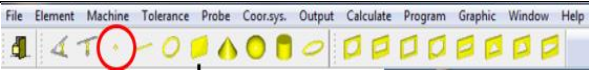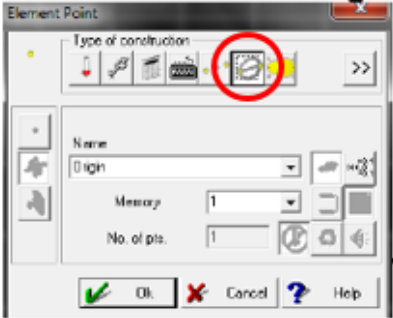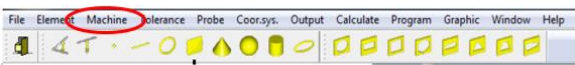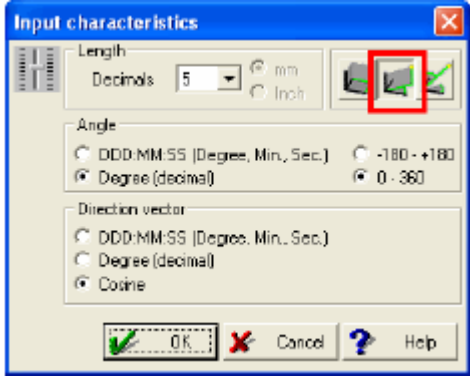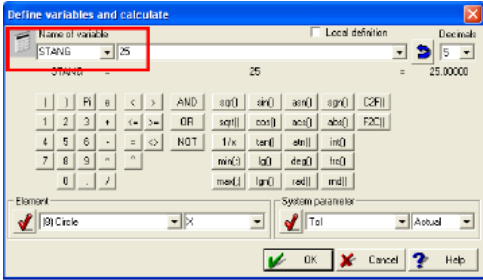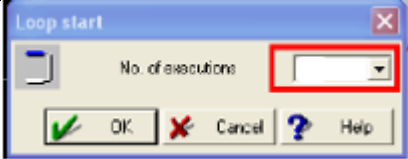
Figure 73. Cylindricity and hole size measurement schematic

Steps for Alignment (Plane, Line & Line)	
	MCOSMOS CMM Software shows PartManager.

	Create new part from Part menu.
	Select New Part from the list.
	Select program list and select the created file of the new program to enter to the CMM learn mode. Set up Units to mm, No. of Probes = 1, No. of Coordinate system = 1 from settings and then input characteristics.
	To print an output file, select All elements and All tolerance comparisons. Press Next and select Open Protocol, Select All elements, Select the Path to

	save the output file, and then Finish.
	Click on Plane icon.
	Select No. of pts. = 4 Click OK. Take 4 hits on the top of the part using the probe of CMM.
	Select Coor. Sys. option and click on Align plane, then choose XY plane and hit OK.
	Click on Line icon and select No. of pts. as 2 and then OK. Take 2 hits on the edge of the part, which is supposed to be the X-axis.

	Click on Coor. sys. and select Align axis parallel to axis and select X-axis, click OK. Repeat previous step and this step for Y-axis.
	Click on Point.
	Select Intersection construction and then OK. In intersection element point window, Select X-axis and Y-axis and hit OK.
Measurement steps	
	Click on Machine, CNC ON/OFF option, CNC ON. Go to Machine and click Clearance height, click on the tick mark.

	For Z-axis, select proper clearance height, say, 20 mm in this case. Select File, Settings, Input characteristics, XY plane and hit OK.
	Click Calculate and click Formula calculation
	Name the variable, say X_DIS. Enter the distance of 1st circle (should be known) and Select X-axis. Make sure that the probe is away from the part. Hit OK.
	Select Program, click loops, and loop start.
	No. of executions = 5 (chosen)
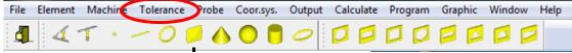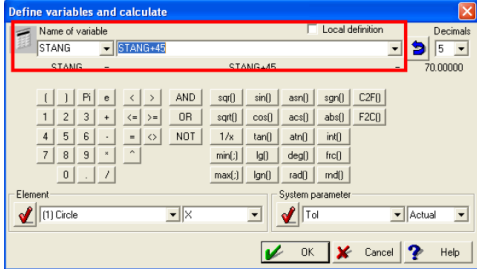
	Click Cylinder icon then select Type of construction as Measurement.
	Select Measure Automatic, Name Cylinder, Select loop counter, No. of pts. = 15 (each circle 5 pts, such 3 circles)
	Automatic cylinder measurement dialog appears. Type of element - inner cylinder, No. of pts. = 15, Diameter = 8, No. of steps = 3, Height difference = 6, Driving plane = XY plane, Start angle = 0, End angle = 360, Driving direction = Circular, counter-clockwise (as probe was at -ve direction), X = X_DIS, Y = 44.88 (distance from the edge of
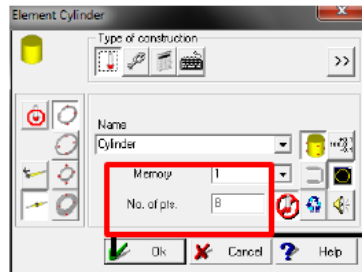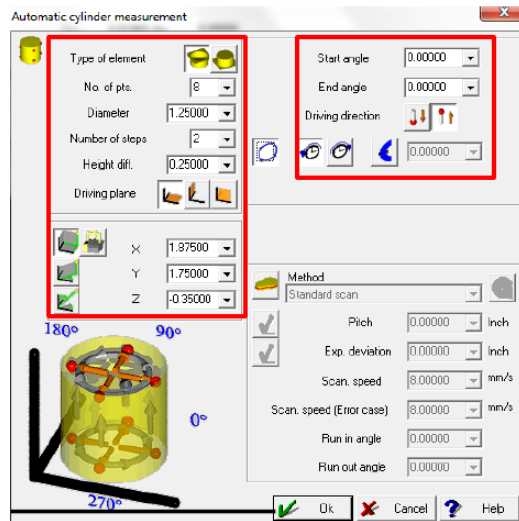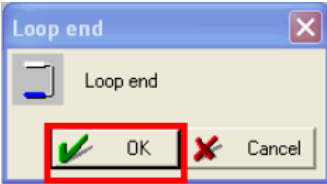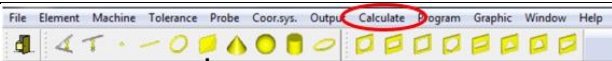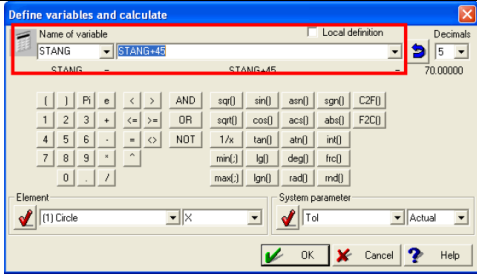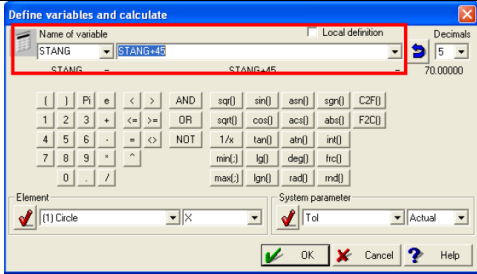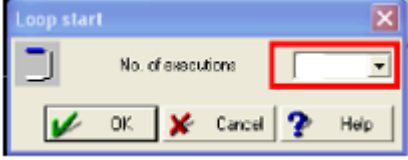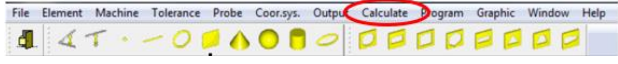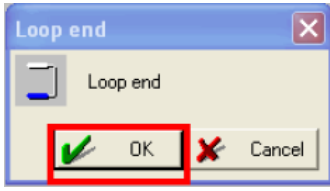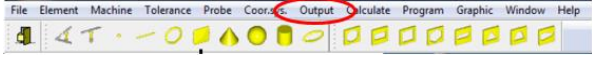
	the part to the measurement point), and Z= -3 (based on where the part needs to be measured), hit OK. The probe moves.
	Click Tolerance element and Tolerance last element, Click C1, OK. Enter the values for Tolerance limits, Diameter = 8, Upper and Lower as required, click OK.
	Redefine the variable for the next measurement. In this case, the distance between the centers of the drilled holes was 10 mm. Select Calculate, Formula calculate, X_DIS+10, and OK.

	Select Program, loop, loop end, and OK. The probe moves and takes the measurement.
	Save the output file to the desired folder by selecting Output, Close output file, OK, Save the file.
	Run the loop for the next measurements as follows. Open the Output file again. If required, change the name of the file for the next measurement.
	Click Calculate, Formula calculation.
	Name the variable, say X_DIS+10.

	Go to Program loops, loop start.
	No. of executions = 5 (chosen).
	Click on the Cylinder icon, Name it as C2, Enter X_DIS, the probe moves. Click Tolerance element, Click C2, OK (check the values of X_Coor etc.).
	Click Calculate, Formula calculate, X_DIS+10, hit OK.
	Click on Program, loop, loop end, and OK. CMM repeats the measurement process.
	Click Output, Close output file, click OK and save the file to the desired folder.
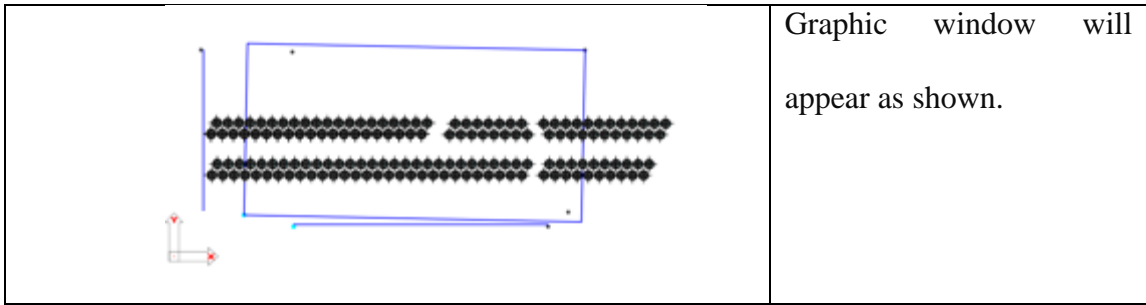
| | Graphic window will appear as shown. |

APPENDIX C

AIRBORNE DIAMETER CALCULATION DATA
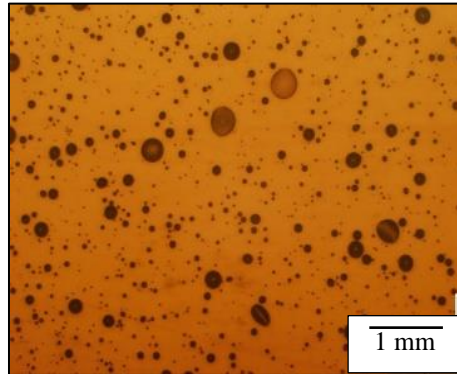
Figure 74. Microscopic image for Castrol oil. Air pressure 413 kPa, drill diameter 8 mm

Following is the data generated from image processing steps for Figure 75:

Sr. No.	Area (μm²)	Perimeter (μm)	Projected diameter (μm)	Volume (μm³)	Airborne diameter(μm)
1	448	76	24	513	10
2	566	86	27	729	11
3	1626	144	45	3553	19
4	118	38	12	69	5
5	695	91	30	993	12
6	895	109	34	1452	14
7	35	19	7	11	3
8	12	10	4	2	2
9	212	51	16	167	7
10	6987	313	94	31649	39
11	51063	847	255	625329	106
12	1426	141	43	2917	18
13	2333	175	55	6106	23
14	1296	133	41	2529	17
15	5267	275	82	20713	34
16	3299	211	65	10269	27
17	342	64	21	342	9
18	106	36	12	59	5
19	12	10	4	2	2
20	353	69	21	360	9
21	554	83	27	706	11
22	589	86	27	775	11
23	212	53	16	167	7
24	20147	534	160	154978	67
25	118	38	12	69	5
26	1437	139	43	2953	18
27	353	65	21	360	9
28	71	29	9	32	4
29	2144	168	52	5381	22
30	401	72	23	435	9
31	2651	184	58	7397	24

Sr. No.	Area (µm²)	Perimeter (µm)	Projected diameter (µm)	Volume (µm³)	Airborne diameter(µm)
32	153	41	14	103	6
33	707	93	30	1019	12
34	2568	204	57	7054	24
35	2993	197	62	8872	26
36	389	68	22	415	9
37	412	69	23	454	10
38	94	31	11	50	5
39	919	107	34	1510	14
40	1084	122	37	1934	15
41	801	102	32	1229	13
42	106	36	12	59	5
43	1485	137	43	3100	18
44	236	53	17	196	7
45	1178	127	39	2192	16
46	306	62	20	291	8
47	2427	180	56	6480	23
48	1037	116	36	1809	15
49	1355	131	42	2703	17
50	2297	175	54	5968	23
51	82	29	10	41	4
52	613	88	28	822	12
53	2239	171	53	5740	22
54	330	62	20	325	9
55	35	19	7	11	3
56	259	55	18	226	8
57	978	115	35	1657	15
58	401	69	23	435	9
59	3323	209	65	10379	27
60	660	93	29	918	12
61	1037	114	36	1809	15
62	2462	180	56	6622	23
63	683	93	29	968	12
64	4890	257	79	18529	33
65	730	97	30	1070	13
66	1437	137	43	2953	18
67	12	10	4	2	2
68	20171	534	160	155250	67
69	412	74	23	454	10
70	1626	153	45	3553	19
71	365	71	22	378	9
72	5856	284	86	24283	36
73	448	73	24	513	10
74	884	107	34	1424	14
75	872	108	33	1395	14
76	2250	177	54	5785	22
77	1520	140	44	3211	18
78	554	82	27	706	11
79	165	48	14	115	6
80	1143	119	38	2094	16
81	1378	138	42	2774	17
82	1331	133	41	2633	17
83	518	84	26	640	11
84	12984	423	129	80177	53
85	141	44	13	91	6
86	5596	277	84	22689	35
87	365	67	22	378	9
88	6492	300	91	28347	38
89	412	73	23	454	10
90	530	86	26	662	11
91	16954	489	147	119637	61
92	2062	169	51	5074	21

Sr. No.	Area (µm²)	Perimeter (µm)	Projected diameter (µm)	Volume (µm³)	Airborne diameter(µm)
93	259	62	18	226	8
94	1732	153	47	3906	20
95	1378	137	42	2774	17
96	5420	275	83	21623	35
97	3252	204	64	10049	27
98	448	79	24	513	10
99	3334	213	65	10434	27
100	2062	165	51	5074	21
101	5973	289	87	25020	36
102	2180	170	53	5515	22
103	4736	255	78	17665	32
104	2616	185	58	7249	24
105	59	26	9	25	4
106	12	10	4	2	2
107	1461	135	43	3026	18
108	353	67	21	360	9
109	177	46	15	127	6
110	59004	908	274	776733	114
111	471	76	24	554	10
112	1119	119	38	2029	16
113	24	15	5	6	2
114	2462	183	56	6622	23
115	884	104	34	1424	14
116	8247	338	102	40590	43
117	3865	224	70	13019	29
118	848	104	33	1339	14
119	943	119	35	1568	14
120	224	53	17	182	7
121	636	93	28	870	12
122	3393	215	66	10712	27
123	1225	127	39	2324	16
124	1190	125	39	2225	16
125	4230	245	73	14908	31
126	2733	190	59	7745	25
127	189	50	15	140	6
128	14268	458	135	92362	56
129	801	99	32	1229	13
130	1202	129	39	2258	16
131	3099	199	63	9348	26
132	7399	316	97	34492	40
133	2863	198	60	8302	25
134	542	83	26	684	11
135	35	19	7	11	3
136	4088	236	72	14167	30
137	601	86	28	798	12
138	7741	329	99	36908	41
139	11146	400	119	63769	50
140	789	100	32	1202	13
141	330	67	20	325	9
142	12	10	4	2	2
143	518	81	26	640	11
144	8813	349	106	44836	44
145	9060	356	107	46737	45
146	9814	369	112	52692	47
147	3205	208	64	9832	27
148	1767	151	47	4026	20
149	1249	130	40	2392	17
150	2321	177	54	6060	23
151	153	46	14	103	6
152	7057	335	95	32130	39
153	2698	194	59	7595	24

Sr. No.	Area (µm²)	Perimeter (µm)	Projected diameter (µm)	Volume (µm³)	Airborne diameter(µm)
154	59	26	9	25	4
155	71	29	9	32	4
156	648	90	29	894	12
157	672	95	29	943	12
158	542	86	26	684	11
159	2297	173	54	5968	23
160	6492	297	91	28347	38
161	141	41	13	91	6
162	931	111	34	1539	14
163	389	71	22	415	9
164	7328	319	97	33999	40
165	2698	192	59	7595	24
166	1661	146	46	3669	19
167	106	33	12	59	5
168	695	95	30	993	12
169	1461	139	43	3026	18
170	2144	168	52	5381	22
171	153	41	14	103	6
172	94	31	11	50	5
173	142562	1411	426	2917112	177
174	3228	208	64	9940	27
175	1037	114	36	1809	15
176	10898	411	118	61658	49
177	2180	168	53	5515	22
178	754	97	31	1122	13
179	4948	262	79	18865	33
180	106	36	12	59	5
181	789	102	32	1202	13
182	3452	217	66	10992	28
183	2015	169	51	4901	21
184	71	36	9	32	4
185	1390	133	42	2809	18
186	5620	273	85	22832	35
187	1508	143	44	3174	18
188	236	53	17	196	7
189	1155	123	38	2126	16
190	24	15	5	6	2
191	1284	130	40	2494	17
192	1520	143	44	3211	18
193	8766	346	106	44477	44
194	306	60	20	291	8
195	613	89	28	822	12
196	518	81	26	640	11
197	2345	175	55	6153	23
198	978	120	35	1657	15
199	283	59	19	258	8
200	2368	185	55	6246	23
201	483	76	25	575	10
202	7022	309	95	31889	39
203	1555	144	44	3324	19
204	389	69	22	415	9
205	2321	178	54	6060	23
206	224	51	17	182	7
207	177	45	15	127	6
208	1744	154	47	3946	20
209	82	31	10	41	4
210	2309	175	54	6014	23
211	1720	148	47	3866	19
212	59	24	9	25	4
213	353	66	21	360	9
214	2946	203	61	8663	25

Sr. No.	Area (µm²)	Perimeter (µm)	Projected diameter (µm)	Volume (µm³)	Airborne diameter(µm)
215	365	66	22	378	9
216	872	108	33	1395	14
217	283	59	19	258	8
218	6056	290	88	25540	37
219	2321	177	54	6060	23
220	719	98	30	1044	13
221	5208	265	81	20366	34
222	342	69	21	342	9
223	4489	245	76	16299	31
224	130	38	13	80	5
225	1119	122	38	2029	16
226	295	59	19	274	8
227	872	107	33	1395	14
228	1190	125	39	2225	16
229	2616	186	58	7249	24
230	47	19	8	18	3
231	342	64	21	342	9
232	2580	189	57	7103	24
233	295	58	19	274	8
234	837	104	33	1311	14
235	106	33	12	59	5
236	7635	321	99	36152	41
237	94	34	11	50	5
238	71	26	9	32	4
239	165	43	14	115	6
240	295	59	19	274	8
241	1060	121	37	1871	15
242	2380	177	55	6292	23
243	353	66	21	360	9
244	624	91	28	846	12
245	507	79	25	618	11
246	59	26	9	25	4
247	47	19	8	18	3
248	71	26	9	32	4
249	10592	380	116	59076	48
250	106	38	12	59	5
251	2392	177	55	6339	23
252	4571	249	76	16750	32
253	766	102	31	1149	13
254	1166	123	39	2159	16
255	12795	425	128	78437	53
256	507	80	25	618	11
257	236	53	17	196	7
258	5031	260	80	19338	33
259	71	26	9	32	4
260	236	55	17	196	7
261	1096	118	37	1966	16
262	271	61	19	242	8
263	978	116	35	1657	15
264	5255	269	82	20643	34
265	94	31	11	50	5
266	259	57	18	226	8
267	3063	201	62	9188	26
268	365	66	22	378	9
269	12	10	4	2	2
270	131688	1374	409	2589780	170
271	5856	281	86	24283	36
272	1449	137	43	2990	18
273	1979	164	50	4772	21
274	3853	227	70	12960	29
275	4183	239	73	14659	30

Sr. No.	Area (μm²)	Perimeter (μm)	Projected diameter (μm)	Volume (μm³)	Airborne diameter(μm)
276	3476	215	67	11105	28
277	1119	124	38	2029	16
278	1956	158	50	4687	21
279	4442	246	75	16043	31
280	1485	137	43	3100	18
281	11287	396	120	64987	50
282	401	71	23	435	9
283	3912	230	71	13258	29
284	683	93	29	968	12
285	754	102	31	1122	13
286	1426	137	43	2917	18
287	2698	192	59	7595	24
288	4960	262	79	18932	33
289	59	24	9	25	4
290	3676	230	68	12078	28
291	118	39	12	69	5
292	342	66	21	342	9
293	1178	126	39	2192	16
294	12	10	4	2	2
295	4666	253	77	17271	32
296	1508	139	44	3174	18
297	1261	130	40	2426	17
298	283	59	19	258	8
299	542	83	26	684	11
300	1308	131	41	2563	17
301	29196	648	193	270350	80
302	10663	389	117	59669	48
303	5396	273	83	21482	34
304	4124	237	72	14351	30
305	2993	199	62	8872	26
306	342	64	21	342	9
307	507	82	25	618	11
308	766	97	31	1149	13
309	17485	496	149	125293	62
310	28937	636	192	266758	80
311	259	55	18	226	8
312	448	75	24	513	10
313	7317	314	97	33917	40
314	1508	139	44	3174	18
315	13573	437	131	85695	55
316	1225	126	39	2324	16
317	919	109	34	1510	14
318	471	77	24	554	10
319	6209	304	89	26515	37
320	919	109	34	1510	14
321	672	93	29	943	12
322	931	108	34	1539	14
323	683	93	29	968	12
324	2239	180	53	5740	22
325	3817	228	70	12782	29
326	130	43	13	80	5
327	4831	259	78	18195	33
328	1060	118	37	1871	15
329	106	34	12	59	5
330	10957	385	118	62158	49
331	16000	478	143	109679	59
332	1308	131	41	2563	17
333	4784	253	78	17929	32
334	1732	149	47	3906	20
335	96071	1163	350	1613731	146
336	448	73	24	513	10

Sr. No.	Area (µm²)	Perimeter (µm)	Projected diameter (µm)	Volume (µm³)	Airborne diameter(µm)
337	9143	360	108	47377	45
338	4041	234	72	13922	30
339	295	60	19	274	8
340	295	60	19	274	8
341	542	84	26	684	11
342	3664	241	68	12020	28
343	436	72	24	493	10
344	10026	371	113	54409	47
345	28135	636	189	255756	79
346	10026	373	113	54409	47
347	742	97	31	1096	13
348	259	55	18	226	8
349	1673	152	46	3709	19
350	1508	142	44	3174	18
351	1096	119	37	1966	16
352	59	24	9	25	4
353	26038	612	182	227700	76
354	507	78	25	618	11
355	2144	175	52	5381	22
356	342	69	21	342	9
357	401	71	23	435	9
358	47	19	8	18	3
359	1496	140	44	3137	18
360	601	88	28	798	12
361	1272	129	40	2460	17
362	10309	373	115	56727	48
363	365	69	22	378	9
364	13714	434	132	87037	55
365	837	104	33	1311	14
366	707	95	30	1019	12
367	742	100	31	1096	13
368	47505	827	246	561120	102
369	412	74	23	454	10
370	483	79	25	575	10
371	189	48	15	140	6
372	118	39	12	69	5
373	1449	137	43	2990	18
374	306	60	20	291	8
375	1060	117	37	1871	15
376	6115	296	88	25913	37
377	47	19	8	18	3
378	1532	147	44	3249	18
379	1225	129	39	2324	16
380	1991	165	50	4815	21
381	130	41	13	80	5
382	1331	133	41	2633	17
383	8000	333	101	38777	42
384	2309	180	54	6014	23
385	59	24	9	25	4
386	106	33	12	59	5
387	954	109	35	1598	15
388	306	61	20	291	8
389	130	38	13	80	5
390	2074	171	51	5117	21
391	1072	119	37	1903	15
392	4171	239	73	14598	30
393	224	53	17	182	7
394	24	17	5	6	2
395	247	57	18	211	7
396	306	62	20	291	8
397	507	80	25	618	11

Sr. No.	Area (µm²)	Perimeter (µm)	Projected diameter (µm)	Volume (µm³)	Airborne diameter(µm)
398	483	79	25	575	10
399	1202	126	39	2258	16
400	707	93	30	1019	12
401	118	43	12	69	5
402	683	93	29	968	12
403	2887	197	61	8405	25
404	2368	177	55	6246	23
405	13325	429	130	83362	54
406	16672	478	146	116657	61
407	7246	313	96	33426	40
408	9897	369	112	53357	47
409	2604	186	58	7201	24
410	436	73	24	493	10
411	825	101	32	1284	13
412	2074	169	51	5117	21
413	353	66	21	360	9
414	1532	141	44	3249	18
415	931	109	34	1539	14
416	730	99	30	1070	13
417	259	55	18	226	8
418	189	48	15	140	6
419	825	102	32	1284	13
420	448	79	24	513	10
421	1897	159	49	4477	20
422	1390	135	42	2809	18
423	28996	632	192	267573	80
424	636	90	28	870	12
425	25214	589	179	216968	75
426	495	81	25	597	10
427	82	31	10	41	4
428	236	53	17	196	7
429	4359	244	75	15598	31
430	177	45	15	127	6
431	2368	177	55	6246	23
432	12	10	4	2	2
433	672	93	29	943	12
434	25049	638	179	214842	74
435	401	71	23	435	9
436	1485	142	43	3100	18
437	4748	253	78	17731	32
438	4183	238	73	14659	30
439	306	62	20	291	8
440	353	67	21	360	9
441	130	41	13	80	5
442	1697	151	46	3787	19
443	1378	137	42	2774	17
444	7647	327	99	36236	41
445	59	24	9	25	4
446	1249	128	40	2392	17
447	3181	211	64	9723	26
448	9673	371	111	51557	46
449	1826	159	48	4229	20
450	672	91	29	943	12
451	24	15	5	6	2
452	4666	249	77	17271	32
453	471	84	24	554	10
454	24	17	5	6	2
455	3228	210	64	9940	27
456	141	41	13	91	6
457	624	91	28	846	12
458	377	69	22	397	9

Sr. No.	Area (µm²)	Perimeter (µm)	Projected diameter (µm)	Volume (µm³)	Airborne diameter(µm)
459	448	74	24	513	10
460	754	99	31	1122	13
461	6739	311	93	29983	39
462	21596	551	166	171996	69
463	177	46	15	127	6
464	1308	130	41	2563	17
465	353	69	21	360	9
466	1473	138	43	3063	18
467	9496	365	110	50151	46
468	24	15	5	6	2
469	1237	131	40	2358	17
470	6127	289	88	25988	37
471	3358	215	65	10545	27
472	2969	198	61	8768	26
473	2474	180	56	6670	23
474	837	104	33	1311	14
475	5596	284	84	22689	35
476	2404	201	55	6386	23
477	636	88	28	870	12
478	118	43	12	69	5
479	931	116	34	1539	14
480	59	26	9	25	4
481	1532	150	44	3249	18
482	47	24	8	18	3
483	483	79	25	575	10
484	82	31	10	41	4
485	1968	163	50	4730	21
486	3947	231	71	13438	29
487	566	83	27	729	11
488	778	99	31	1175	13
489	1131	121	38	2061	16
490	224	51	17	182	7
491	1119	121	38	2029	16
492	3629	221	68	11847	28
493	1708	152	47	3827	19
494	1767	156	47	4026	20
495	4359	249	75	15598	31
496	401	71	23	435	9
497	825	105	32	1284	13
498	766	99	31	1149	13
499	165	46	14	115	6
500	672	93	29	943	12
501	1791	154	48	4107	20
502	766	100	31	1149	13
503	1155	121	38	2126	16
504	35087	725	211	356174	88
505	11169	392	119	63972	50
506	389	69	22	415	9
507	259	57	18	226	8
508	1744	154	47	3946	20
509	12	10	4	2	2
510	471	79	24	554	10
511	872	109	33	1395	14
512	754	99	31	1122	13
513	1331	132	41	2633	17
514	5608	276	85	22761	35
515	683	97	29	968	12
516	1591	144	45	3438	19
517	424	72	23	473	10
518	2050	166	51	5030	21
519	318	64	20	307	8

Sr. No.	Area (µm²)	Perimeter (µm)	Projected diameter (µm)	Volume (µm³)	Airborne diameter(µm)
520	318	62	20	307	8
521	4171	242	73	14598	30
522	5891	283	87	24504	36
523	342	66	21	342	9
524	3676	221	68	12078	28
525	212	51	16	167	7
526	3935	237	71	13378	29
527	20206	532	160	155658	67
528	16471	483	145	114561	60
529	813	104	32	1256	13
530	931	111	34	1539	14
531	542	83	26	684	11
532	2133	171	52	5337	22
533	4619	249	77	17010	32
534	3417	215	66	10824	27
535	778	101	31	1175	13
536	6704	302	92	29747	38
537	200	51	16	154	7
538	2191	173	53	5560	22
539	12772	422	128	78220	53
540	1037	115	36	1809	15
541	59	26	9	25	4
542	96636	1170	351	1628001	146
543	624	93	28	846	12
544	59	24	9	25	4
545	1331	131	41	2633	17
546	7564	327	98	35651	41
547	683	97	29	968	12
548	40719	754	228	445283	95
549	7788	328	100	37246	41
550	683	95	29	968	12
551	247	55	18	211	7
552	1579	147	45	3400	19
553	754	97	31	1122	13
554	1779	153	48	4067	20
555	130	41	13	80	5
556	14940	460	138	98959	57
557	94	36	11	50	5
558	9591	369	111	50899	46
559	848	106	33	1339	14
560	130	41	13	80	5
561	3700	224	69	12195	29
562	7411	322	97	34574	40
563	1202	128	39	2258	16
564	8212	335	102	40330	43
565	2616	190	58	7249	24
566	4183	241	73	14659	30
567	141	43	13	91	6
568	801	97	32	1229	13
569	1814	156	48	4188	20
570	19770	553	159	150648	66
571	2239	176	53	5740	22
572	837	111	33	1311	14
573	9744	367	111	52123	46
574	189	48	15	140	6
575	16377	475	144	113579	60
576	71	26	9	32	4
577	353	66	21	360	9
578	860	111	33	1367	14
579	1049	119	37	1840	15
580	648	91	29	894	12

Sr. No.	Area (µm²)	Perimeter (µm)	Projected diameter (µm)	Volume (µm³)	Airborne diameter(µm)
581	3523	220	67	11331	28
582	884	104	34	1424	14
583	518	84	26	640	11
584	730	112	30	1070	13
585	71	26	9	32	4
586	1567	145	45	3362	19
587	94	31	11	50	5
588	1720	149	47	3866	19
589	71	26	9	32	4
590	106	36	12	59	5
591	12	10	4	2	2
592	4029	234	72	13862	30
593	1343	133	41	2668	17
594	47	19	8	18	3
595	389	69	22	415	9
596	1155	126	38	2126	16
597	1001	114	36	1718	15
598	837	105	33	1311	14
599	966	111	35	1627	15
600	1909	161	49	4519	21
601	82	31	10	41	4
602	1331	135	41	2633	17
603	10144	373	114	55371	47
604	542	89	26	684	11
605	2651	190	58	7397	24
606	1532	141	44	3249	18
607	50097	835	253	607666	105
608	47	19	8	18	3
609	1343	133	41	2668	17
610	106	33	12	59	5
611	5549	276	84	22403	35
612	12748	418	127	78004	53
613	259	57	18	226	8
614	601	89	28	798	12
615	1520	139	44	3211	18
616	4230	244	73	14908	31
617	648	90	29	894	12
618	1131	124	38	2061	16
619	2580	186	57	7103	24
620	4807	255	78	18062	33
621	837	110	33	1311	14
622	1084	123	37	1934	15
623	189	51	15	140	6
624	1013	115	36	1748	15
625	165	43	14	115	6
626	212	50	16	167	7
627	5361	304	83	21271	34
628	412	71	23	454	10
629	554	87	27	706	11
630	872	109	33	1395	14
631	943	111	35	1568	14
632	271	57	19	242	8
633	1909	163	49	4519	21
634	943	111	35	1568	14
635	377	69	22	397	9
636	20100	529	160	154434	67
637	13726	449	132	87149	55
638	18769	517	155	139347	64
639	48565	854	249	580012	103
640	6386	291	90	27655	38
641	2981	202	62	8820	26

Sr. No.	Area (µm²)	Perimeter (µm)	Projected diameter (µm)	Volume (µm³)	Airborne diameter(µm)
642	3664	225	68	12020	28
643	507	83	25	618	11
644	2863	196	60	8302	25
645	2333	178	55	6106	23
646	189	48	15	140	6
647	11275	402	120	64885	50
648	1155	124	38	2126	16
649	47	19	8	18	3
650	3393	215	66	10712	27
651	130	38	13	80	5
652	566	83	27	729	11
653	1508	137	44	3174	18
654	1803	153	48	4148	20
655	6303	291	90	27121	37
656	212	53	16	167	7
657	1567	142	45	3362	19
658	7010	309	94	31809	39
659	766	99	31	1149	13
660	2663	190	58	7446	24
661	306	61	20	291	8
662	672	91	29	943	12
663	5078	262	80	19611	33
664	12194	447	125	72977	52
665	1108	121	38	1997	16
666	6739	310	93	29983	39
667	200	49	16	154	7
668	12	10	4	2	2
669	24	15	5	6	2
670	801	100	32	1229	13
671	3040	199	62	9082	26
672	236	55	17	196	7
673	789	104	32	1202	13
674	1155	124	38	2126	16
675	10934	392	118	61958	49
676	471	76	24	554	10
677	459	79	24	534	10
678	990	115	35	1687	15
679	71	26	9	32	4
680	636	91	28	870	12
681	2345	175	55	6153	23
682	57107	918	270	739579	112
683	2144	175	52	5381	22
684	507	87	25	618	11
685	1155	125	38	2126	16
686	978	111	35	1657	15
687	495	83	25	597	10
688	3417	230	66	10824	27
689	2510	185	57	6813	24
690	59	24	9	25	4
691	4536	251	76	16556	32
692	9909	366	112	53453	47
693	895	111	34	1452	14
694	130	38	13	80	5
695	2969	213	61	8768	26
696	789	104	32	1202	13
697	1355	133	42	2703	17
698	789	100	32	1202	13
699	1190	126	39	2225	16
700	4112	237	72	14289	30
701	2027	164	51	4944	21
702	2392	180	55	6339	23

Sr. No.	Area (µm²)	Perimeter (µm)	Projected diameter (µm)	Volume (µm³)	Airborne diameter(µm)
703	6798	312	93	30377	39
704	1202	128	39	2258	16
705	35	19	7	11	3
706	966	111	35	1627	15
707	3169	206	64	9669	26
708	12807	430	128	78545	53
709	82	29	10	41	4
710	1343	133	41	2668	17
711	754	99	31	1122	13
712	1885	159	49	4436	20
713	141	41	13	91	6
714	342	66	21	342	9
715	7682	323	99	36488	41
716	3817	227	70	12782	29
717	283	64	19	258	8
718	1119	126	38	2029	16
719	1060	114	37	1871	15
720	2875	196	61	8353	25
721	5490	272	84	22047	35
722	778	99	31	1175	13
723	707	95	30	1019	12
724	801	103	32	1229	13
725	2568	184	57	7054	24
726	12	10	4	2	2
727	1897	165	49	4477	20
728	872	104	33	1395	14
729	295	61	19	274	8
730	59	29	9	25	4
731	1449	155	43	2990	18
732	1414	140	42	2881	18
733	4041	231	72	13922	30
734	306	61	20	291	8
735	589	88	27	775	11
736	1214	128	39	2291	16
737	130	38	13	80	5
738	224	51	17	182	7
739	10698	390	117	59966	49
740	1096	118	37	1966	16
741	507	80	25	618	11
742	2074	188	51	5117	21
743	1473	142	43	3063	18
744	3747	227	69	12428	29
745	1166	127	39	2159	16
746	2828	193	60	8149	25
747	16954	492	147	119637	61
748	389	71	22	415	9
749	2239	175	53	5740	22
750	4996	268	80	19135	33
751	11452	399	121	66416	50
752	1720	149	47	3866	19
753	15599	473	141	105586	59
754	82	33	10	41	4
755	212	51	16	167	7
756	106	36	12	59	5
757	495	79	25	597	10
758	41461	765	230	457514	96
759	2969	201	61	8768	26
760	236	55	17	196	7
761	1638	149	46	3592	19
762	3181	215	64	9723	26
763	660	90	29	918	12

Sr. No.	Area (µm²)	Perimeter (µm)	Projected diameter (µm)	Volume (µm³)	Airborne diameter(µm)
764	754	97	31	1122	13
765	412	73	23	454	10
766	2663	190	58	7446	24
767	931	112	34	1539	14
768	2710	197	59	7645	24
769	153	43	14	103	6
770	70303	1048	299	1010204	124
771	1390	135	42	2809	18
772	518	83	26	640	11
773	318	67	20	307	8
774	12	10	4	2	2
775	577	86	27	752	11
776	589	87	27	775	11
777	153	41	14	103	6
778	554	86	27	706	11
779	672	93	29	943	12
780	6186	296	89	26364	37
781	554	86	27	706	11
782	141	41	13	91	6
783	5361	272	83	21271	34
784	1732	151	47	3906	20
785	212	53	16	167	7
786	471	79	24	554	10
787	1261	133	40	2426	17
788	1378	135	42	2774	17
789	4489	246	76	16299	31
790	1072	119	37	1903	15
791	2321	177	54	6060	23
792	624	88	28	846	12
793	6044	289	88	25465	37
794	530	86	26	662	11
795	424	77	23	473	10
796	530	83	26	662	11
797	507	82	25	618	11
798	7776	333	100	37161	41
799	3087	203	63	9295	26
800	8966	352	107	46010	44
801	4277	241	74	15158	31
802	28783	634	191	264643	80
803	813	102	32	1256	13
804	7859	333	100	37754	42
805	1072	119	37	1903	15
806	283	58	19	258	8
807	3323	211	65	10379	27
808	9272	360	109	48388	45
809	200	51	16	154	7
810	542	82	26	684	11
811	4972	264	80	19000	33
812	707	96	30	1019	12
813	1343	135	41	2668	17
814	2616	190	58	7249	24
815	1284	133	40	2494	17
816	2946	211	61	8663	25
817	1461	136	43	3026	18
818	424	72	23	473	10
819	271	65	19	242	8
820	1108	122	38	1997	16
821	507	84	25	618	11
822	483	79	25	575	10
823	1178	125	39	2192	16
824	459	76	24	534	10

Sr. No.	Area (µm²)	Perimeter (µm)	Projected diameter (µm)	Volume (µm³)	Airborne diameter(µm)
825	3841	240	70	12900	29
826	52937	894	260	660054	108
827	71	31	9	32	4
828	1708	163	47	3827	19
829	837	105	33	1311	14
830	1814	159	48	4188	20
831	1166	126	39	2159	16
832	412	75	23	454	10
833	3664	227	68	12020	28
834	1661	154	46	3669	19
835	1355	136	42	2703	17
836	5349	272	83	21201	34
837	1331	135	41	2633	17
838	130	39	13	80	5
839	5655	283	85	23048	35
840	10462	391	115	57996	48
841	754	98	31	1122	13
842	35	19	7	11	3
843	707	95	30	1019	12
844	259	59	18	226	8
845	200	50	16	154	7
846	2875	207	61	8353	25
847	1225	126	39	2324	16
848	518	86	26	640	11
849	1084	127	37	1934	15
850	82	34	10	41	4
851	9638	410	111	51275	46
852	3087	203	63	9295	26
853	94	34	11	50	5
854	1920	161	49	4561	21
855	2003	164	50	4858	21
856	5573	274	84	22546	35
857	530	84	26	662	11
858	71470	999	302	1035449	126
859	412	73	23	454	10
860	3099	201	63	9348	26
861	401	70	23	435	9
862	943	129	35	1568	14
863	3570	225	67	11559	28
864	542	88	26	684	11
865	825	102	32	1284	13
866	1272	133	40	2460	17
867	1214	128	39	2291	16
868	4371	244	75	15662	31
869	35	19	7	11	3
870	35	19	7	11	3
871	306	61	20	291	8
872	4418	258	75	15916	31
873	8059	333	101	39207	42
874	848	102	33	1339	14
875	3982	228	71	13619	30
876	3546	223	67	11445	28
877	424	74	23	473	10
878	471	79	24	554	10
879	2109	169	52	5249	22
880	2816	196	60	8098	25
881	9838	370	112	52882	47
882	1131	124	38	2061	16
883	613	88	28	822	12
884	789	104	32	1202	13
885	24	15	5	6	2

Sr. No.	Area (µm²)	Perimeter (µm)	Projected diameter (µm)	Volume (µm³)	Airborne diameter(µm)
886	848	103	33	1339	14
887	1155	128	38	2126	16
888	200	50	16	154	7
889	1072	119	37	1903	15
890	2321	178	54	6060	23
891	978	119	35	1657	15
892	943	109	35	1568	14
893	436	76	24	493	10
894	16224	557	144	111989	60
895	1308	131	41	2563	17
896	3853	227	70	12960	29
897	4135	247	73	14412	30
898	589	88	27	775	11
899	2156	168	52	5426	22
900	1131	128	38	2061	16
901	1131	122	38	2061	16
902	10792	389	117	60760	49
903	11334	417	120	65394	50
904	9767	365	112	52313	46
905	1131	127	38	2061	16
906	15623	474	141	105826	59
907	401	75	23	435	9
908	35	19	7	11	3
909	141	40	13	91	6
910	1673	149	46	3709	19
911	542	84	26	684	11
912	601	88	28	798	12
913	2486	185	56	6717	23
914	1543	147	44	3286	18
915	1991	169	50	4815	21
916	907	120	34	1481	14
917	1296	133	41	2529	17
918	2486	181	56	6717	23
919	2356	180	55	6199	23
920	141	43	13	91	6
921	495	84	25	597	10
922	624	93	28	846	12
923	1814	157	48	4188	20
924	1249	129	40	2392	17
925	200	48	16	154	7
926	825	107	32	1284	13
927	530	84	26	662	11
928	931	107	34	1539	14
929	1178	123	39	2192	16
930	389	73	22	415	9
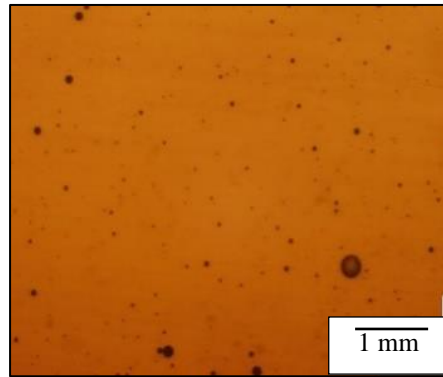
Figure 75. Microscopic image for Castrol oil. Air pressure 413 kPa, drill diameter 8 mm

Sr. No.	Area (µm²)	Perimeter (µm)	Projected diameter (µm)	Volume (µm³)	Airborne diameter(µm)
1	153	41	14	103	6
2	106	33	12	59	5
3	11264	394	120	64783	50
4	1214	129	39	2291	16
5	1402	137	42	2845	18
6	318	62	20	307	8
7	47	19	8	18	3
8	12	10	4	2	2
9	1461	140	43	3026	18
10	1956	164	50	4687	21
11	554	84	27	706	11
12	766	98	31	1149	13
13	448	78	24	513	10
14	35	23	7	11	3
15	2415	182	55	6433	23
16	719	95	30	1044	13
17	283	61	19	258	8
18	177	48	15	127	6
19	554	91	27	706	11
20	24	17	5	6	2
21	35	21	7	11	3
22	1331	133	41	2633	17
23	9968	369	113	53930	47
24	59	24	9	25	4
25	12	10	4	2	2
26	71	36	9	32	4
27	2757	194	59	7845	25
28	1779	157	48	4067	20
29	2003	159	50	4858	21
30	82	33	10	41	4
31	200	60	16	154	7
32	318	64	20	307	8
33	695	95	30	993	12
34	8907	355	106	45557	44
35	401	71	23	435	9
36	5007	262	80	19203	33
37	589	88	27	775	11
38	837	102	33	1311	14
39	12	10	4	2	2

185

Sr. No.	Area (µm²)	Perimeter (µm)	Projected diameter (µm)	Volume (µm³)	Airborne diameter(µm)
40	200	53	16	154	7
41	2663	192	58	7446	24
42	1001	114	36	1718	15
43	236	57	17	196	7
44	71	26	9	32	4
45	118	38	12	69	5
46	71	26	9	32	4
47	719	97	30	1044	13
48	259	59	18	226	8
49	707	95	30	1019	12
50	177	45	15	127	6
51	601	89	28	798	12
52	1496	144	44	3137	18
53	12	10	4	2	2
54	12	10	4	2	2
55	2498	186	56	6765	23
56	283	59	19	258	8
57	271	61	19	242	8
58	35	19	7	11	3
59	377	74	22	397	9
60	1237	131	40	2358	17
61	1708	152	47	3827	19
62	353	68	21	360	9
63	12	10	4	2	2
64	1602	149	45	3476	19
65	153	49	14	103	6
66	165	48	14	115	6
67	1272	131	40	2460	17
68	518	84	26	640	11
69	212	50	16	167	7
70	1190	126	39	2225	16
71	542	85	26	684	11
72	1025	116	36	1779	15
73	259	57	18	226	8
74	1284	133	40	2494	17
75	12	10	4	2	2
76	200	52	16	154	7
77	2710	194	59	7645	24
78	1426	142	43	2917	18
79	247	57	18	211	7
80	412	73	23	454	10
81	3935	234	71	13378	29
82	81814	1075	323	1268205	134
83	59	26	9	25	4
84	4206	239	73	14784	30
85	1013	114	36	1748	15
86	3641	222	68	11905	28
87	895	106	34	1452	14
88	224	53	17	182	7
89	495	81	25	597	10
90	1155	121	38	2126	16
91	35	21	7	11	3
92	1037	117	36	1809	15
93	71	29	9	32	4
94	966	113	35	1627	15
95	601	88	28	798	12
96	5832	282	86	24137	36
97	672	91	29	943	12
98	801	104	32	1229	13
99	554	86	27	706	11
100	2250	173	54	5785	22

Sr. No.	Area (μm²)	Perimeter (μm)	Projected diameter (μm)	Volume (μm³)	Airborne diameter(μm)
101	1602	150	45	3476	19
102	189	49	15	140	6
103	648	90	29	894	12
104	71	26	9	32	4
105	82	31	10	41	4
106	259	57	18	226	8
107	330	64	20	325	9
108	306	64	20	291	8
109	94	36	11	50	5
110	12	10	4	2	2
111	1414	138	42	2881	18
112	660	90	29	918	12
113	566	91	27	729	11
114	306	62	20	291	8
115	177	45	15	127	6
116	2898	198	61	8456	25
117	318	64	20	307	8
118	401	69	23	435	9
119	23823	578	174	199272	72
120	6398	298	90	27732	38
121	789	99	32	1202	13
122	24	15	5	6	2
123	224	53	17	182	7
124	4359	246	75	15598	31
125	59	24	9	25	4
126	542	84	26	684	11
127	306	61	20	291	8
128	153	46	14	103	6
129	224	51	17	182	7
130	141	41	13	91	6
131	330	66	20	325	9

DRILLED HOLE DATA FROM CMM

Cylindricity and hole diameter of drilled holes with Coolube 2210Al as the lubricant:
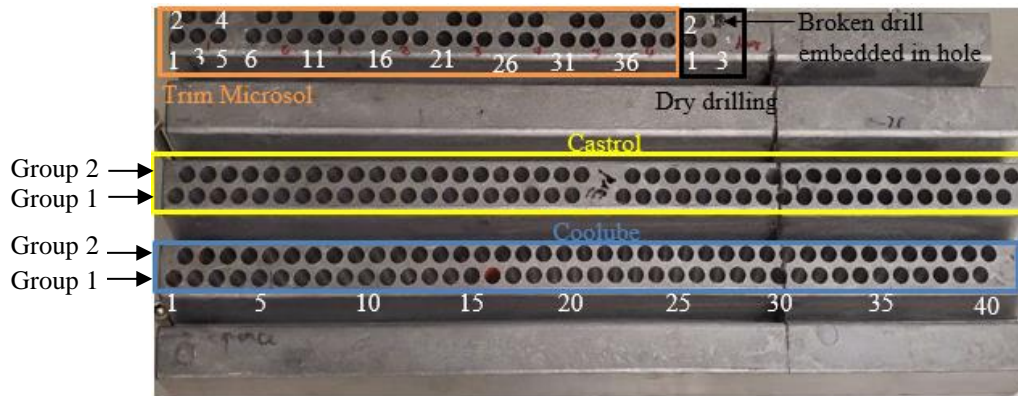

Figure 76. Drilled hole layout. Group 1 drilling tests with oil quantity 40 and 60 mL/hr. Group 2 drilling tests with oil quantity 100 and 400 mL/hr.

Hole Sr. No.	Air Pressure (kPa)	Oil quantity (mL/hr)	Cylindricity (mm)	Hole diameter (mm)
1			0.01485	7.99095
2			0.01396	7.99092
3	413	40	0.01698	7.98952
4			0.01942	7.99023
5			0.01915	7.98935
6			0.01539	7.98913
7			0.00958	7.99524
8	413	60	0.01194	7.99716
9			0.00981	8.00089
10			0.00274	8.00559
11			0.00638	7.99896
12			0.00615	8.00031
13	620	40	0.01106	7.99802
14			0.00872	7.99582
15			----------	----------
16			0.0088	7.99884
17			0.00547	8.00007
18	620	60	0.04777	7.99473
19			0.03968	7.9959
20			0.01843	7.99855
21			0.03308	7.99879
22			0.01689	7.99981
23	413	40	0.0199	7.999
24			0.02575	7.99954
25			0.02733	7.99711
26			0.02742	7.99597
27			0.0247	7.99924
28	413	60	0.02648	8.00187
29			0.02381	7.99473
30			----------	----------

			0.01897	7.99296
31			0.01897	7.99296
32			0.01827	7.99513
33	620	40	0.01603	7.99677
34			0.01049	7.99939
35			0.00651	8.00154
36			0.01651	7.99806
37			0.00362	8.00292
38	620	60	0.00478	8.00256
39			0.05567	7.99609
40			0.0079	8.00711

Cylindricity and hole diameter of drilled holes with Castrol Hyspray A 1536 as the

lubricant:

Hole Sr. No.	Air Pressure (psi)	Oil quantity (mL/hr)	Cylindricity (mm)	Hole diameter (mm)
1			0.0068	7.9771
2			0.00998	7.9816
3	413	40	0.00702	7.98669
4			0.01373	7.99083
5			0.00724	7.99043
6			0.01078	7.99098
7			0.01405	7.99168
8	413	60	0.01263	7.99392
9			0.02361	7.99223
10			0.03005	7.9973
11			0.00646	7.99873
12			0.0129	7.99902
13	620	40	0.01149	7.99952
14			0.0085	7.99938
15			0.02242	7.99666
16			0.00709	7.99843
17			0.0127	7.99615
18	620	60	0.0122	8
19			0.00883	7.99872
20			----------	-----------
21			0.02493	7.99103
22			0.03102	7.98517
23	413	40	0.01392	7.99084
24			0.01066	7.99181
25			0.0096	7.9914
26			0.01112	7.9922
27			0.00935	7.99449
28	413	60	0.00835	7.99782
29			----------	-----------
30			0.01196	8.0014
31			0.00612	7.99971
32			0.00637	8.0006
33	620	40	0.0055	7.99997
34			0.00676	8.00088
35			0.00514	7.99871
36			0.00724	8.0016
37			0.00615	8.00193
38	620	60	0.00588	8.00233
39			0.00871	8.00026
40			0.0101	7.99704

APPENDIX E

K-MEANS CLUSTERING

Following program code was used in RStudio version 1.1.463 to determine number of

clusters for airborne droplet sizes.

Statements	Comments
require("xlsx") require("readxl") require("ggplot2") require("factoextra") require("ORCME") require("fpc")	Install packages to read excel files, plot graphs, etc.
r_data=read_excel(file.choose(), 1) attach(r_data)	Choose the file for which the data needs to be analyzed. Access the data with attach command.
colors=c("blue") duration=150 hist(D, duration, col=colors, main="Droplet Diameter Distribution", xlab="Droplet Diameter(um)")	Select desired color for the histogram. Plot the histogram with desired duration, color, and name the X and Y axes.
set.seed(123) k.max <- 15	Elbow plot generation Assign a maximum value of k as 15.

|	
data <- r_data wss <- sapply(1:k.max, function(k){kmeans(data, k, nstart=50,iter.max = 15)$tot.withinss}) wss plot(1:k.max, wss, type="b", pch = 19, frame = FALSE, xlab="Number of clusters K", ylab="Total within-clusters sum of squares")	Calculate within-clusters sum of squares for k=1 to 15 and use the 'kmeans' function. Plot the elbow plot (within-clusters sum of squares vs number of clusters) with plot command and name the X and Y axes.
k3= kmeans(r_data,3,nstart = 50,iter.max = 15) k3	From the elbow plot, choose an appropriate k. For identifying means of clusters and other details use kmeans function again with chosen k.

APPENDIX F

ELBOW PLOTS

Input for generating elbow plots was airborne droplet sizes calculated after image

processing steps. Elbow plots for Coolube oil using the RStudio software version
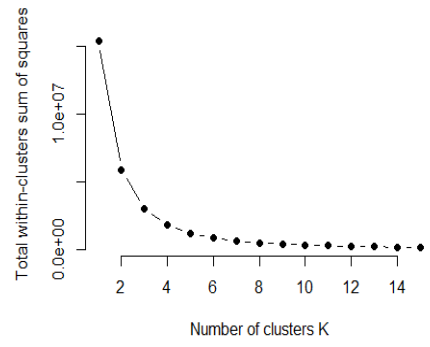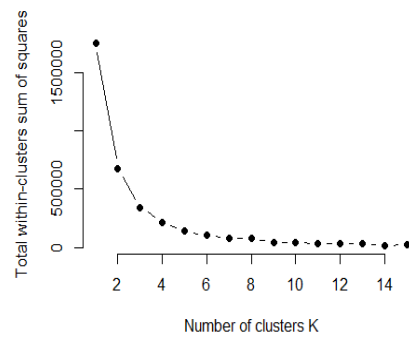
1.1.463 (referring to Appendix E) are listed below.

Air pressure (kPa)	4 mm drill	8 mm drill
413		
551		

| 689 | | |
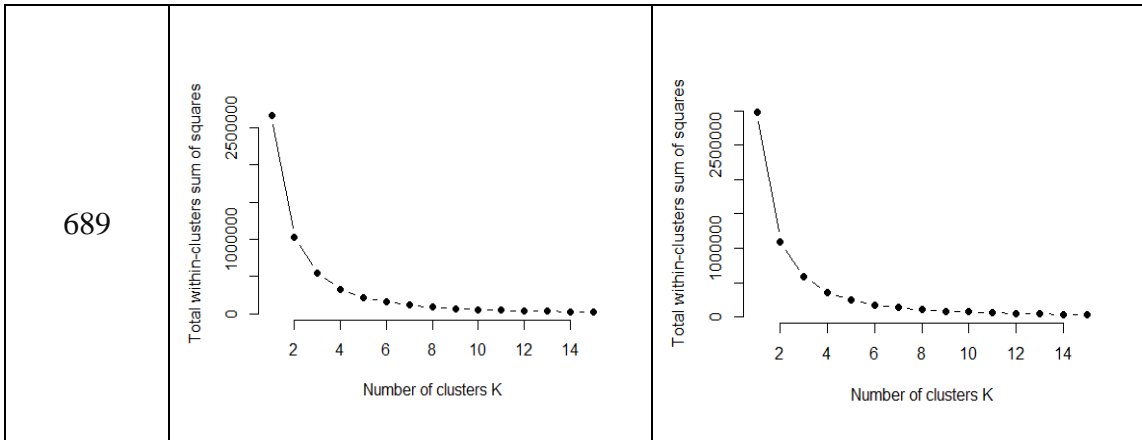
Elbow plots for Castrol oil using the RStudio software:

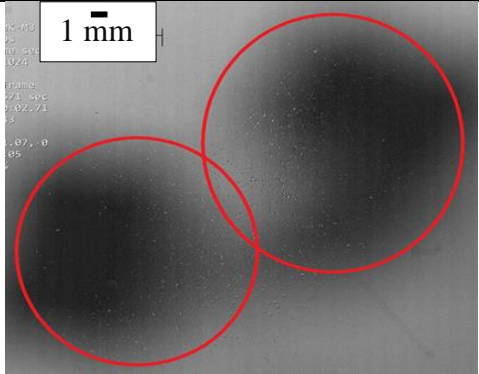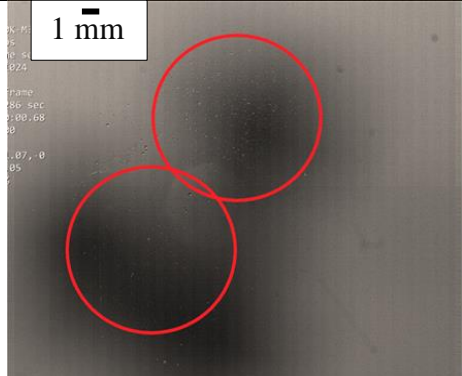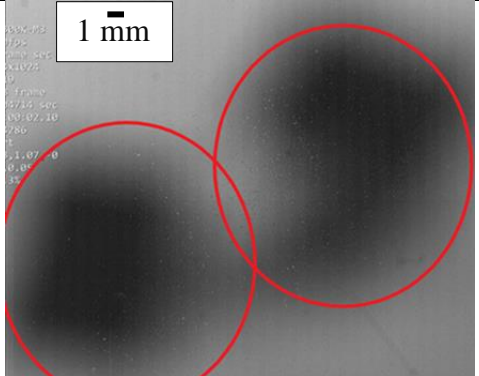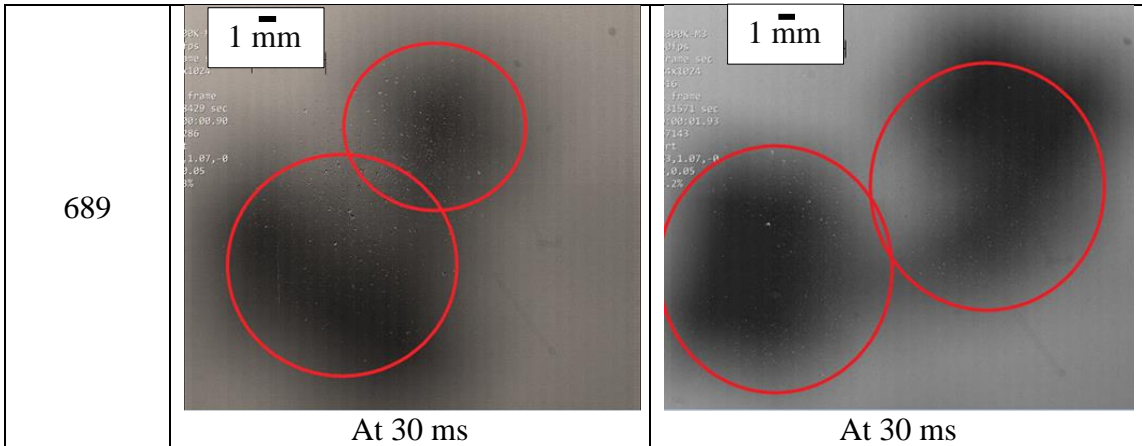| Air pressure (kPa)	4 mm drill	8 mm drill
413		
551		
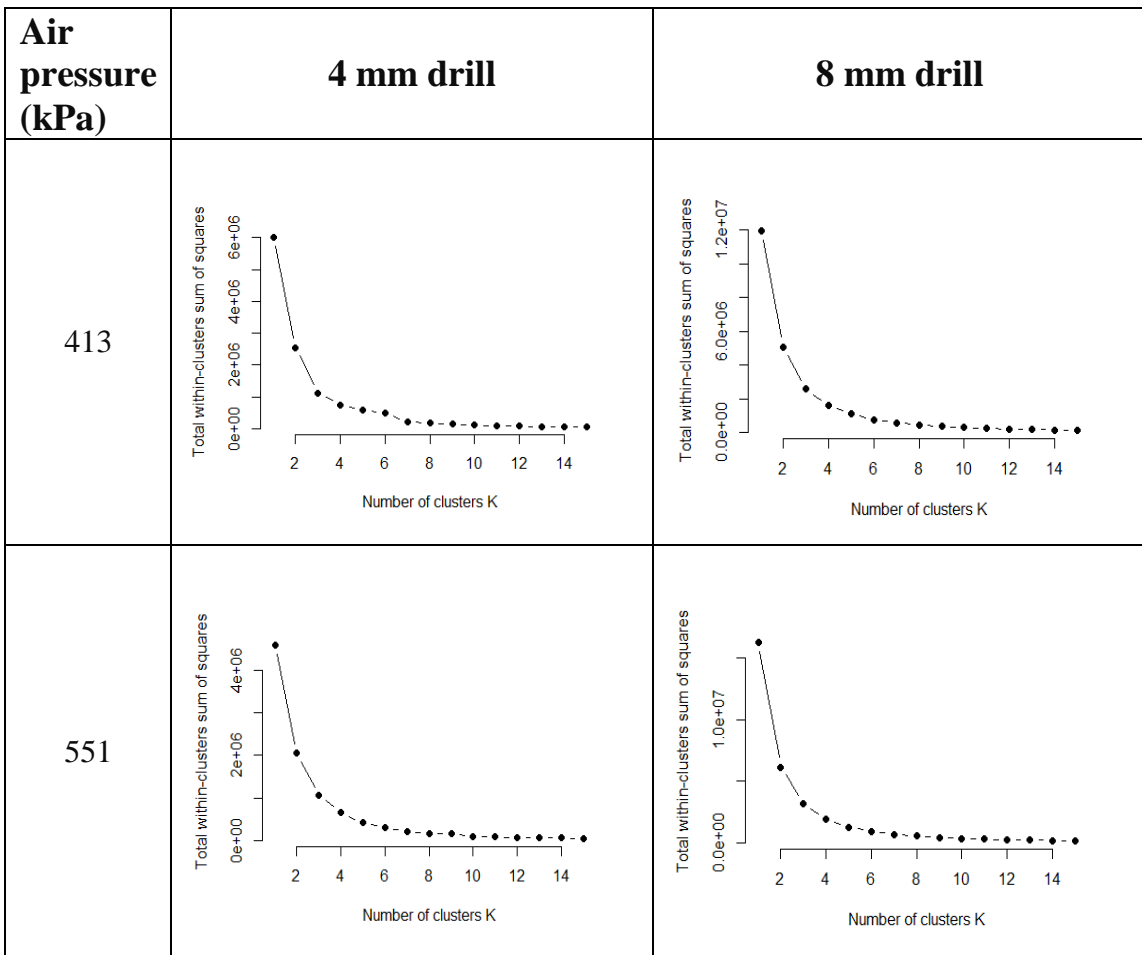
| 689 | | |
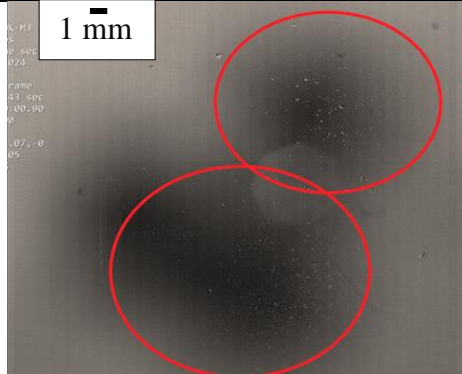
APPENDIX G

HIGH SPEED IMAGING DATA

The high speed imaging data collected from the horizontally positioned drill and vertical glass panel is enlisted below.
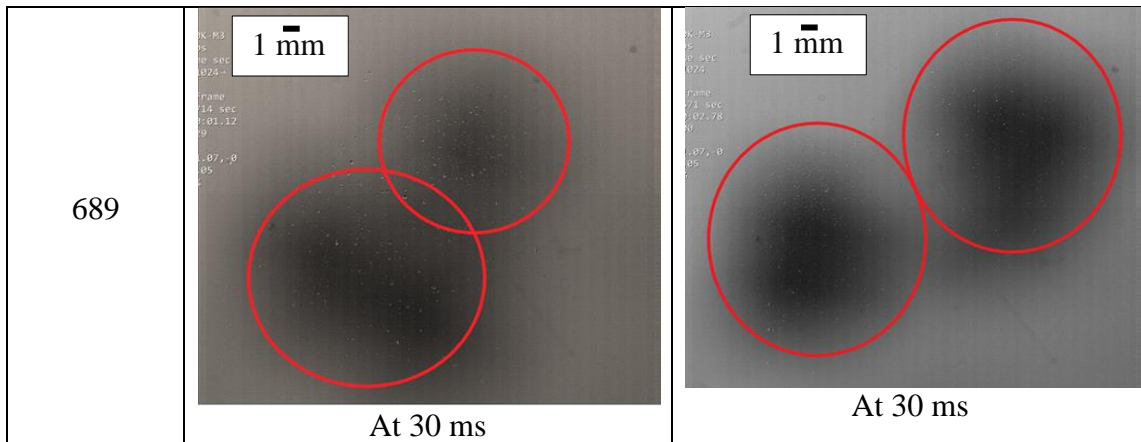
51 mm distance between the drill bit and the observation surface:

Air pressure (kPa)	4 mm drill	8 mm drill
413	At 80 ms	At 30 ms
551	At 30 ms	At 10 ms

689	At 30 ms	At 30 ms

76 mm distance between the drill bit and the observation surface:

Air pressure (kPa)	4 mm drill	8 mm drill
413	At 10 ms	At 30 ms
551	At 30 ms	At 30 ms

689	1 mm At 30 ms	1 mm At 30 ms

4 mm drill with air pressure of 413 kPa:

Distance from Glass (mm)	Size of Impact Zone (mm)	Distance between impact zones (mm)
25	6.15	9.94
51	7.87	13.18
76	8.59	17.50
Plugged hole	13.39	N/A

4 mm drill with air pressure of 551 kPa:

Distance from Glass (mm)	Size of Impact Zone (mm)	Distance between impact zones (mm)
25	5.40	7.34
51	8.59	12.40
76	8.93	13.11

4 mm drill with air pressure of 689 kPa:

Distance from Glass (mm)	Size of Impact Zone (mm)	Distance between impact zones (mm)
25	3.27	5.19
51	6.05	10.65
76	8.82	12.81

8 mm drill with air pressure 413 kPa:

Distance from Glass (mm)	Size of Impact Zone (mm)	Distance between impact zones (mm)
25	6.15	7.88
51	8.90	9.63
76	10.80	15.21

8 mm drill with air pressure 551 kPa:

Distance from Glass (mm)	Size of Impact Zone (mm)	Distance between impact zones (mm)
25	5.52	8.64
51	9.38	10.63
76	10.20	15.40

8 mm drill with air pressure 689 kPa:

Distance from Glass (mm)	Size of Impact Zone (mm)	Distance between impact zones (mm)
25	5.67	9.39
51	11.90	14.16
76	11.88	15.96

Exposure time of mist collected on observation surface:

Drill size (mm)	Distance from Glass (mm)	Pressure (kPa)	Exposure Time (ms)
4	25	413	70
4	25	551	30
4	25	689	30
4	51	413	80
4	51	551	30
4	51	689	30
4	76	413	10
4	76	551	30
4	76	689	30
8	25	413	30
8	25	551	10
8	25	689	10
8	51	413	30
8	51	551	10
8	51	689	30
8	76	413	30
8	76	551	30
8	76	689	30

APPENDIX H

REGRESSION ANALYSIS

Minitab 18.0 was used to perform regression analysis on the cylindricity and hole oversize data collected from metrology experiments. Regression analysis was performed to determine dependency of cylindricity and hole oversize on oil quanity and input air pressure.

Flood coolant method: Regression Analysis

Cylindricity (mm) versus Flood Coolant Flow (mL/hr), Coolant concentration in water (%)
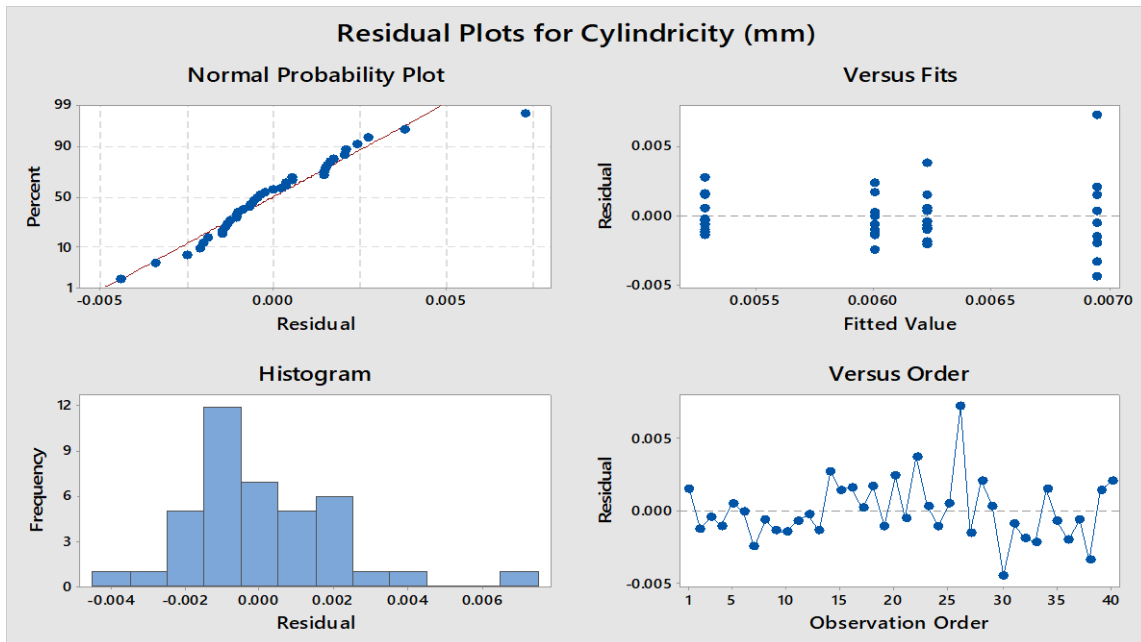
Model Summary

S	R-sq	R-sq(adj)	R-sq(pred)
0.0021461	7.68%	2.68%	0.00%

Coefficients

Term	Coef	SE Coef	T-Value	P-Value	VIF
Constant	0.00794	0.00114	6.97	0.000	
Flood coolant flow (mL/hr)	-0.000000	0.000000	-1.06	0.295	1.00
Coolant concentration in water	-0.000189	0.000136	-1.40	0.171	1.00

Regression Equation

Cylindricity (mm) = 0.00794 - 0.000000 Flood coolant flow (mL/hr)
                            - 0.000189 Coolant concentration in water

Residual Plots for Cylindricity (mm)

Hole diameter (mm) versus Flood Coolant Flow (mL/hr), Coolant concentration in water (%)

Model Summary

S	R-sq	R-sq(adj)	R-sq(pred)
0.0021408	3.56%	0.00%	0.00%

Coefficients

Term	Coef	SE Coef	T-Value	P-Value	VIF
Constant	8.00020	0.00114	7039.83	0.000	
Flood coolant flow (mL/hr)	0.000000	0.000000	0.77	0.447	1.00
Coolant concentration in water	0.000119	0.000135	0.88	0.384	1.00

Regression Equation

Hole diameter (mm) = 8.00020 + 0.000000 Flood coolant flow (mL/hr) + 0.000119 Coolant concentration in water

201
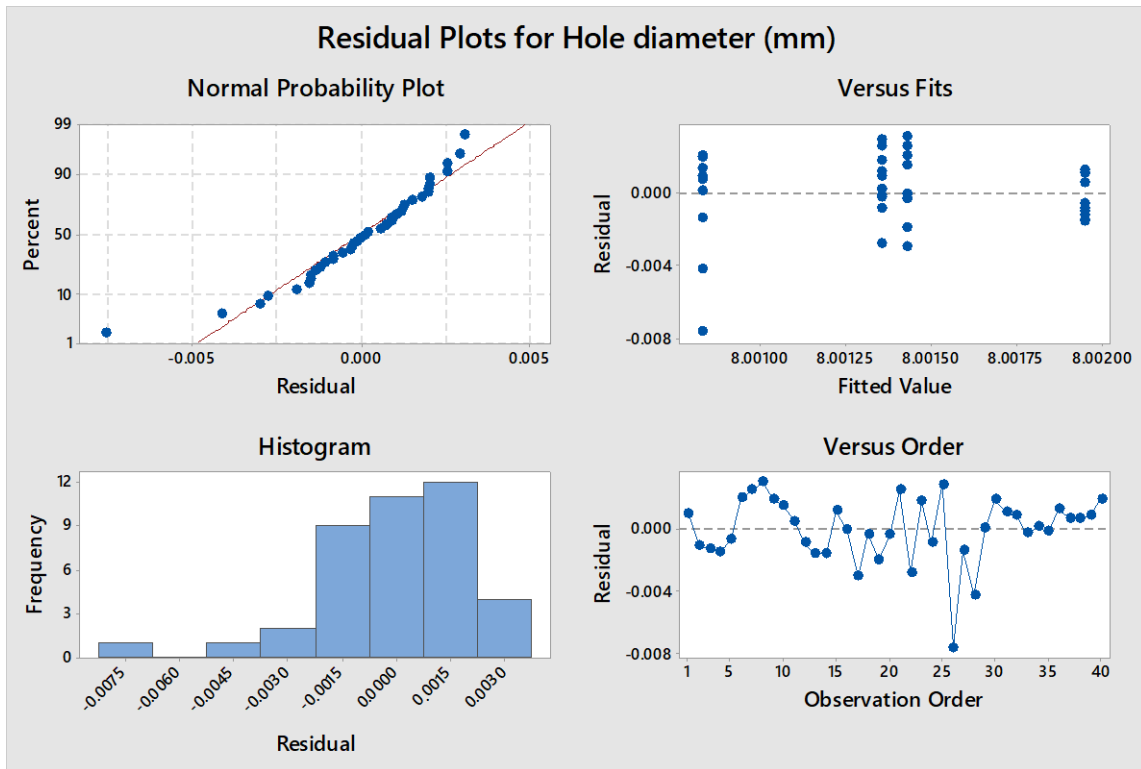
Coolube oil (40 and 60 mL/hr flow rate)
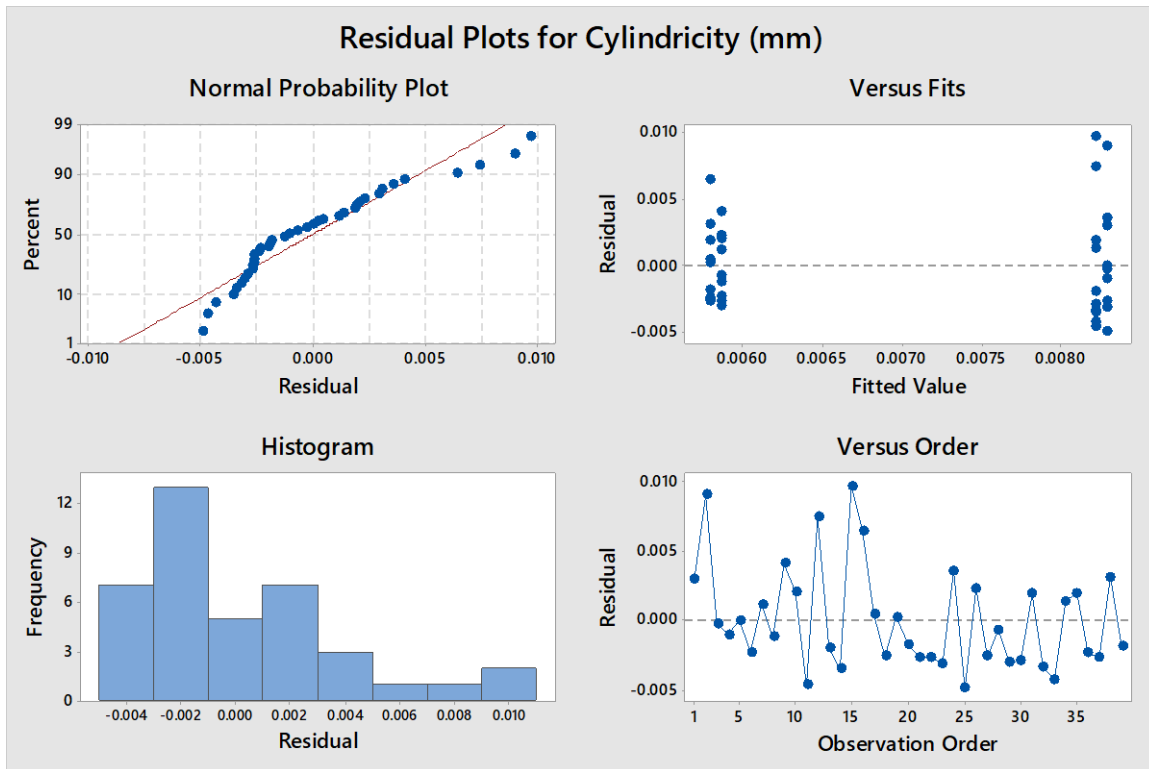Cylindricity (mm) versus Air Pressure (kPa) and Oil Quantity (mL/hr)

Model Summary

S	R-sq	R-sq(adj)	R-sq(pred)
0.0038002	9.98%	4.98%	0.00%

Coefficients

Term	Coef	SE Coef	T-Value	P-Value	VIF
Constant	0.01329	0.00429	3.10	0.004	
Air pressure (kPa)	-0.000000	0.000006	-0.06	0.954	1.00
Oil quantity (mL/hr)	-0.000121	0.000061	-1.99	0.054	1.00

Regression Equation

Cylindricity   = 0.01329 - 0.000000 Air pressure (kPa)
(mm)   - 0.000121 Oil quantity (mL/hr)

Residual Plots for Cylindricity (mm)

Hole diameter (mm) versus Air Pressure (KPa) and Oil Quantity (mL/hr)
Model Summary

S	R-sq	R-sq(adj)	R-sq(pred)
0.0026658	1.38%	0.00%	0.00%

Coefficients

Term	Coef	SE Coef	T-Value	P-Value	VIF
Constant	8.00622	0.00301	2661.63	0.000	
Air pressure (kPa)	-0.000002	0.000004	-0.56	0.579	1.00
Oil quantity (mL/hr)	-0.000018	0.000043	-0.42	0.677	1.00

Regression Equation

Hole diameter
(mm)

= 8.00622 - 0.000002 Air pressure (kPa)
  - 0.000018 Oil quantity (mL/hr)

Residual Plots for Hole diameter (mm)
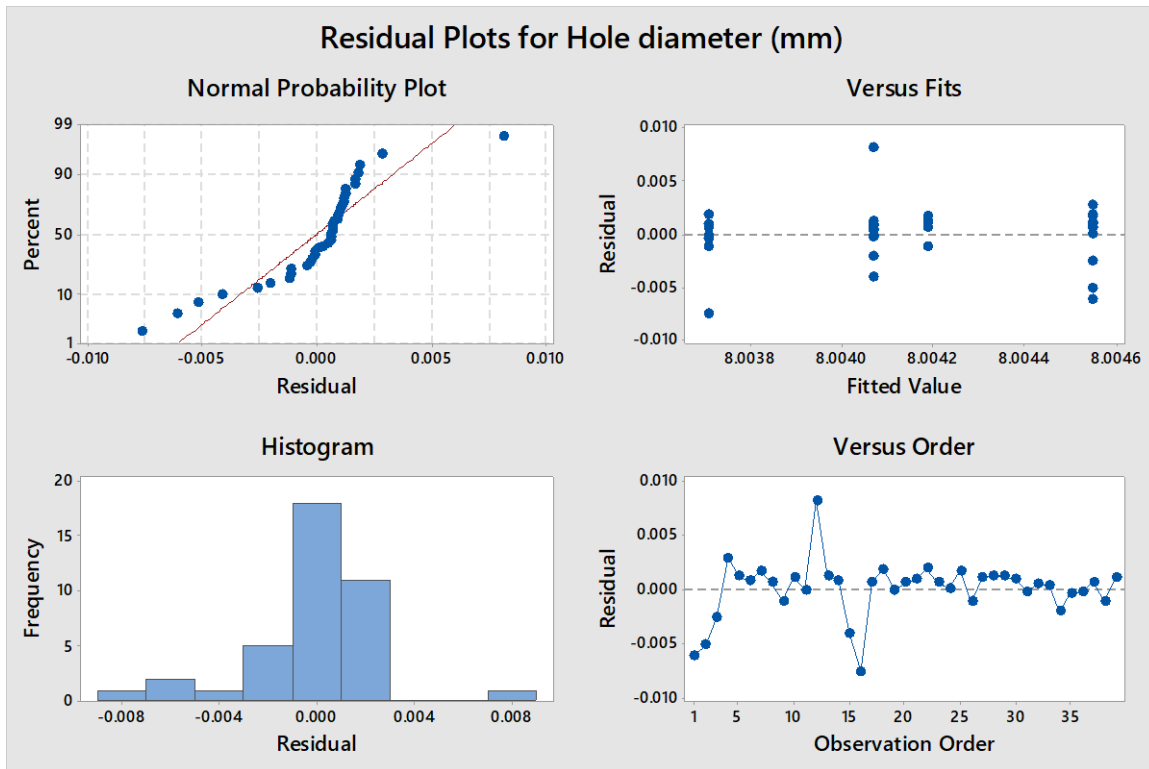
Coolube oil (100 and 400 mL/hr oil flow rate)
Cylindricity (mm) versus Air Pressure (kPa) and Oil Quantity (mL/hr)
Model Summary

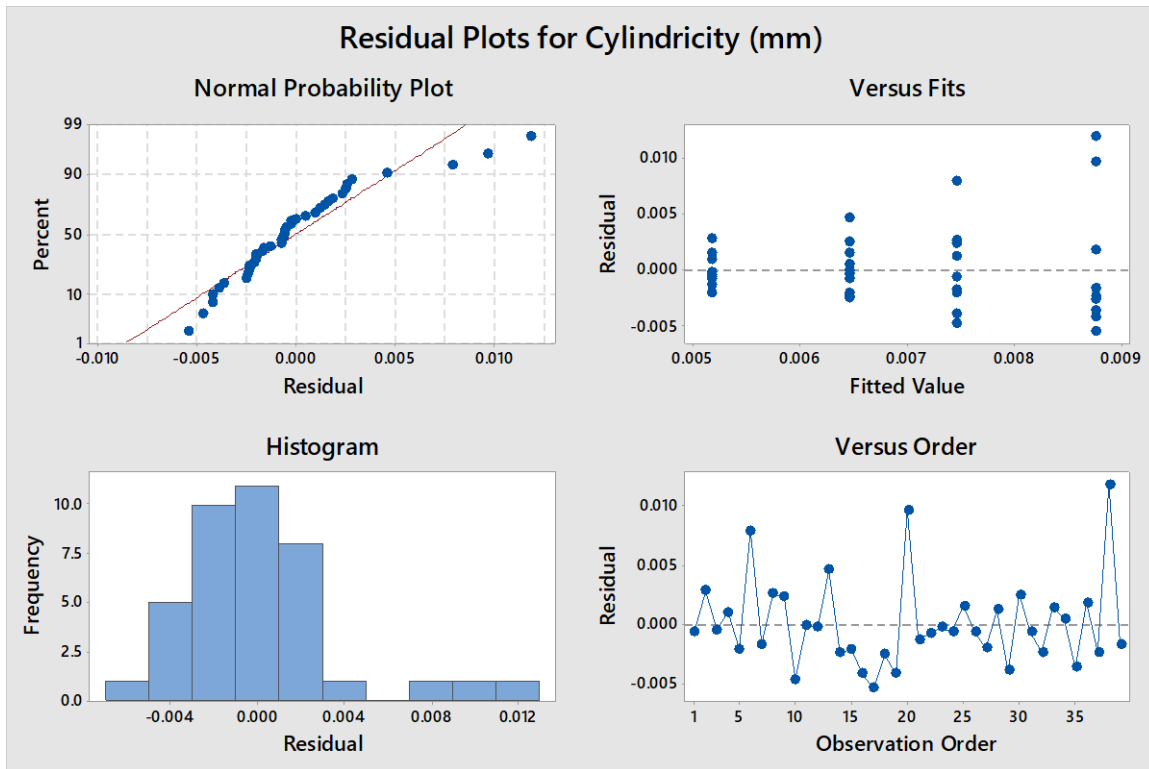| S	R-sq	R-sq(adj)	R-sq(pred)
0.0038005	11.78%	6.88%	0.00%

Coefficients

Term	Coef	SE Coef	T-Value	P-Value	VIF
Constant	0.00182	0.00325	0.56	0.579	
Air pressure (kPa)	0.000006	0.000006	1.06	0.296	1.00
Oil quantity (mL/hr)	0.000008	0.000004	1.89	0.067	1.00

Regression Equation

Cylindricity (mm) = 0.00182 + 0.000006 Air pressure (kPa) + 0.000008 Oil quantity (mL/hr)

204

Residual Plots for Cylindricity (mm)

Hole diameter (mm) versus Air Pressure (kPa) and Oil Quantity (mL/hr)

Model Summary

S	R-sq	R-sq(adj)	R-sq(pred)
0.0032849	7.05%	1.89%	0.00%

Coefficients

Term	Coef	SE Coef	T-Value	P-Value	VIF
Constant	8.00760	0.00281	2853.81	0.000	
Air pressure (kPa)	-0.000007	0.000005	-1.44	0.159	1.00
Oil quantity (mL/hr)	-0.000003	0.000004	-0.78	0.442	1.00

Regression Equation

Hole diameter (mm) $=$ 8.00760 - 0.000007 Air pressure (kPa) - 0.000003 Oil quantity (mL/hr)

Residual Plots for Hole diameter (mm)
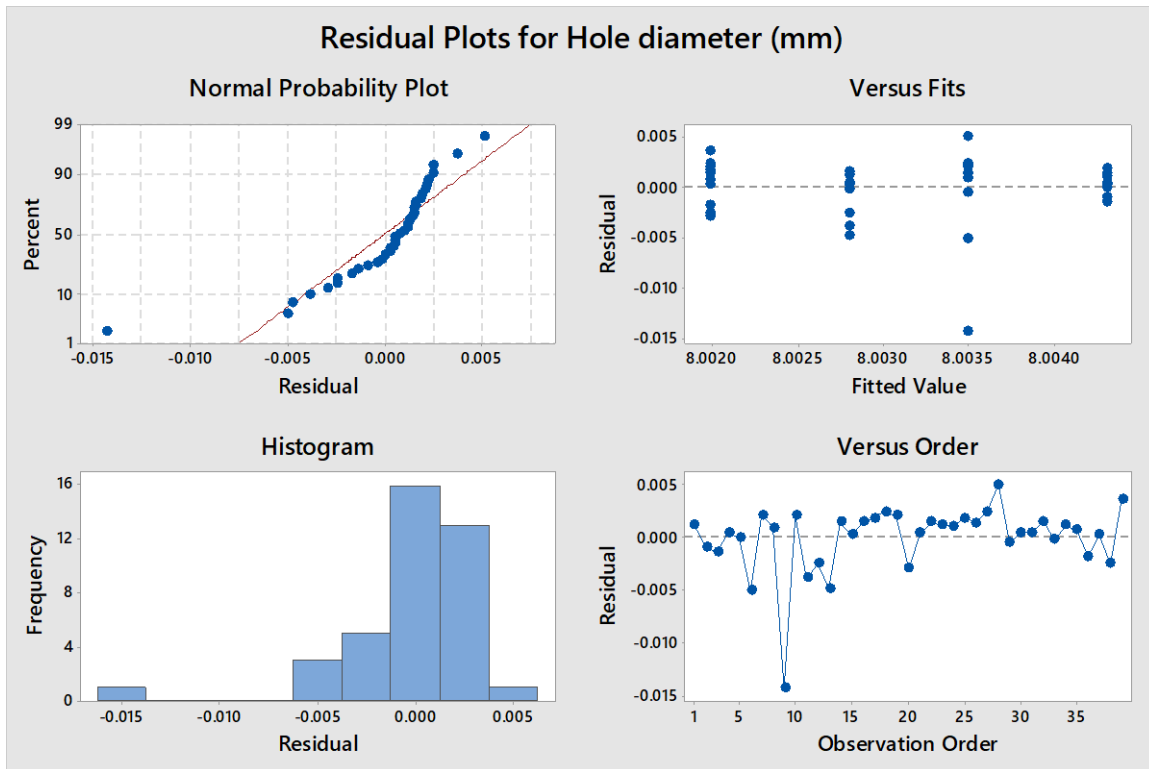
Castrol oil (40 and 60 mL/hr oil flow rate)
Cylindricity (mm) versus Air Pressure (kPa) and Oil Quantity (mL/hr)
Model Summary

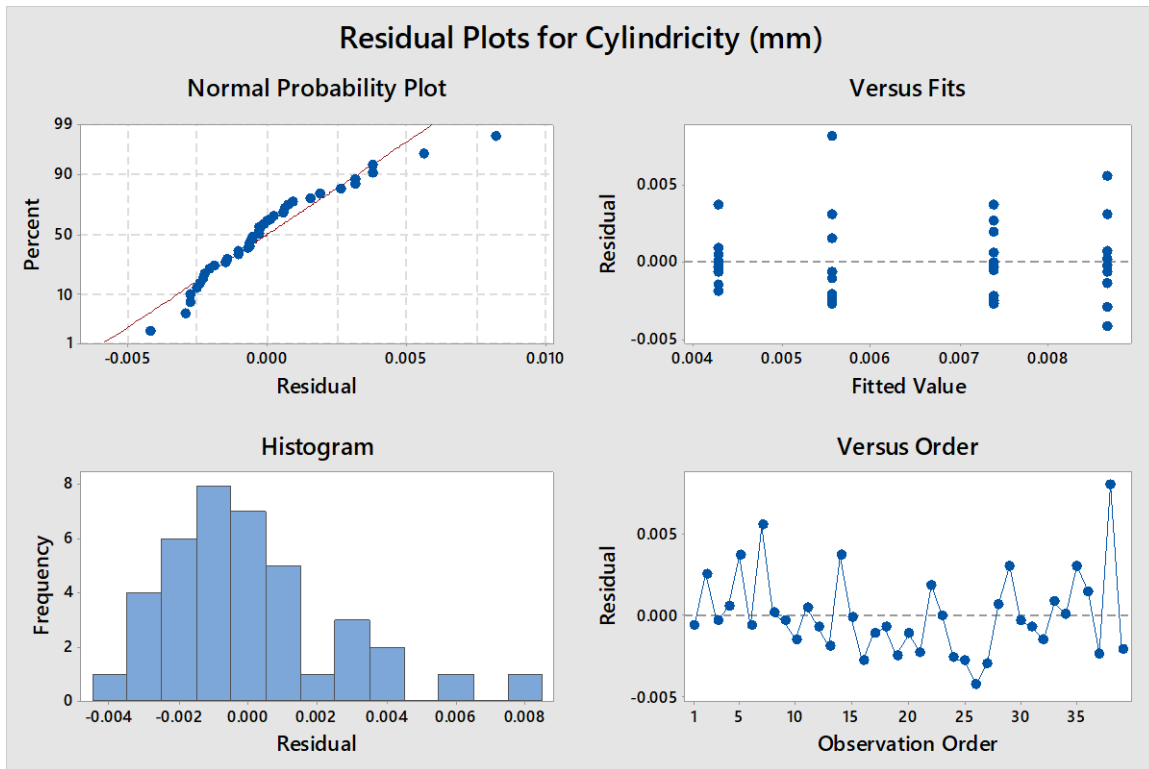| S	R-sq	R-sq(adj)	R-sq(pred)
0.0025895	30.92%	27.08%	18.87%

Coefficients

Term	Coef	SE Coef	T-Value	P-Value	VIF
Constant	0.01101	0.00292	3.77	0.001	
Air pressure (kPa)	-0.000015	0.000004	-3.74	0.001	1.00
Oil quantity (mL/hr)	0.000064	0.000041	1.55	0.130	1.00

Regression Equation

Cylindricity (mm) = 0.01101 - 0.000015 Air pressure (kPa) + 0.000064 Oil quantity (mL/hr)

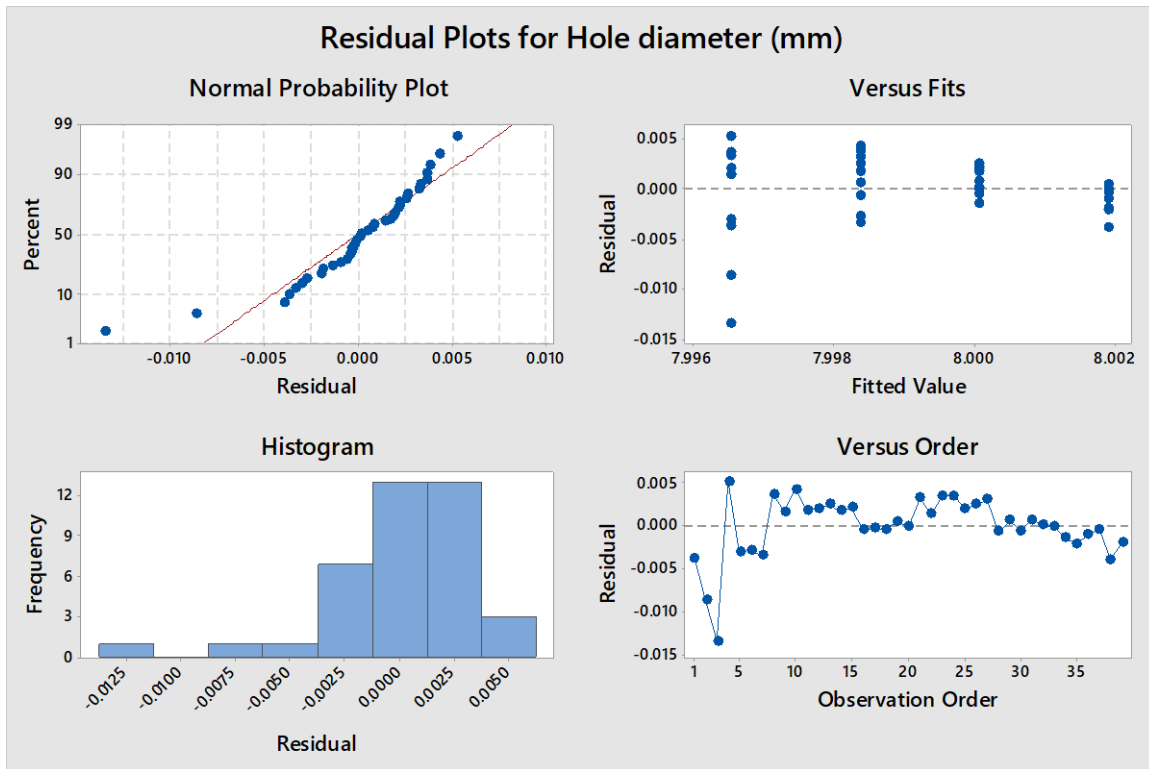Hole diameter (mm) versus Air Pressure (KPa) and Oil Quantity (mL/hr)
Model Summary

S	R-sq	R-sq(adj)	R-sq(pred)
0.0036259	25.09%	20.93%	12.17%

Coefficients

Term	Coef	SE Coef	T-Value	P-Value	VIF
Constant	7.98579	0.00409	1951.85	0.000	
Air pressure (kPa)	0.000017	0.000006	3.05	0.004	1.00
Oil quantity (mL/hr)	0.000092	0.000058	1.58	0.123	1.00

Regression Equation

Hole diameter (mm) $= 7.98579 + 0.000017$ Air pressure (kPa) $+ 0.000092$ Oil quantity (mL/hr)

Residual Plots for Hole diameter (mm)

Castrol oil (100 and 400 mL/hr oil flow rate)
Cylindricity (mm) versus Air Pressure (kPa) and Oil Quantity (mL/hr)
Model Summary

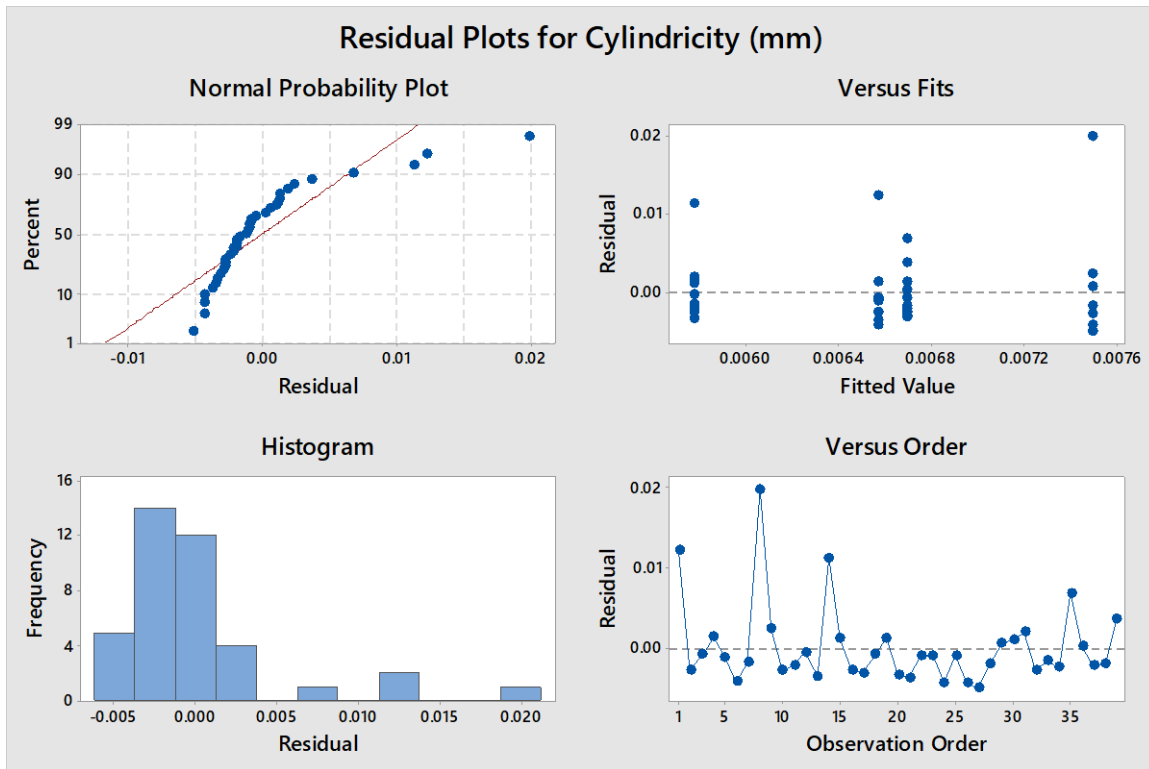| S	R-sq	R-sq(adj)	R-sq(pred)
0.0051292	1.46%	0.00%	0.00%

Coefficients

Term	Coef	SE Coef	T-Value	P-Value	VIF
Constant	0.00785	0.00438	1.79	0.082	
Air pressure (kPa)	-0.000004	0.000008	-0.48	0.631	1.00
Oil quantity (mL/hr)	0.000003	0.000005	0.56	0.580	1.00

Regression Equation

Cylindricity (mm) $= 0.00785 - 0.000004$ Air pressure (kPa) $+ 0.000003$ Oil quantity (mL/hr)

Residual Plots for Cylindricity (mm)

Hole diameter (mm) versus Air Pressure (kPa) and Oil Quantity (mL/hr)
Model Summary

S	R-sq	R-sq(adj)	R-sq(pred)
0.0012478	10.54%	5.57%	0.00%

Coefficients

Term	Coef	SE Coef	T-Value	P-Value	VIF
Constant	8.00243	0.00107	7507.82	0.000	
Air pressure (kPa)	-0.000004	0.000002	-1.96	0.058	1.00
Oil quantity (mL/hr)	-0.000001	0.000001	-0.58	0.565	1.00

Regression Equation

Hole diameter (mm) $=$ 8.00243 - 0.000004 Air pressure (kPa) - 0.000001 Oil quantity (mL/hr)

209

Residual Plots for Hole diameter (mm)

ANOVA Analysis:

Main Effects Plot for Cylindricity (mm)

Main Effects Plot for Hole diameter (mm)
Data Means

Main Effects Plot for Cylindricity (mm)
Data Means
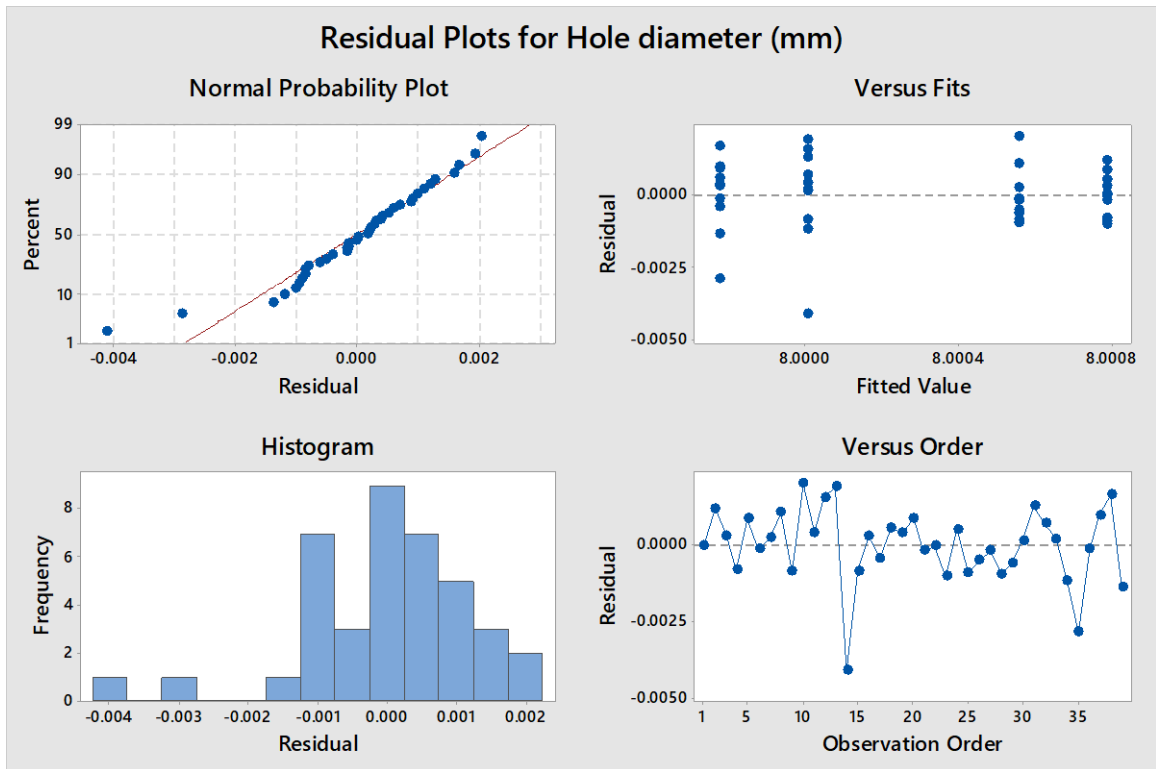
Main Effects Plot for Hole diameter (mm)
Data Means
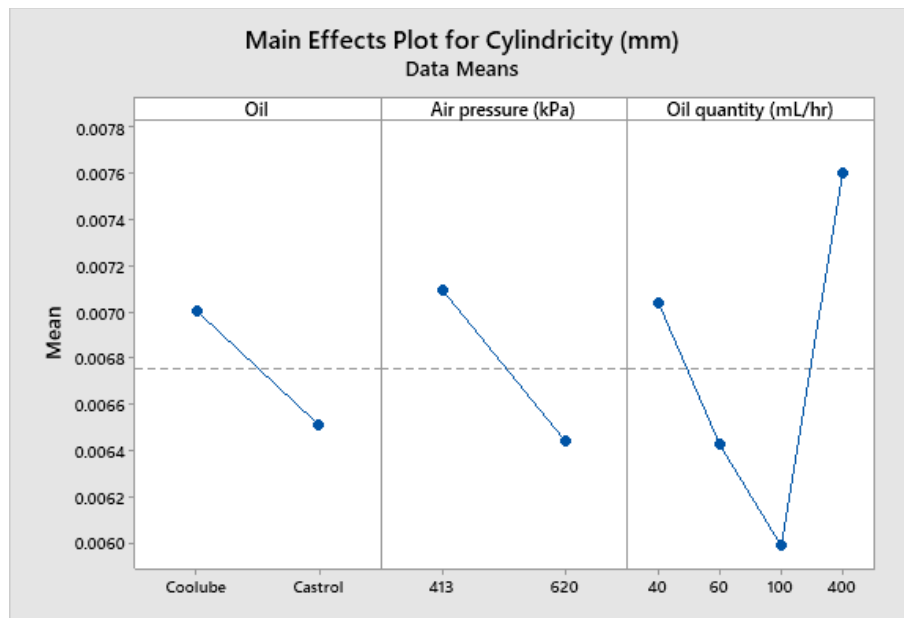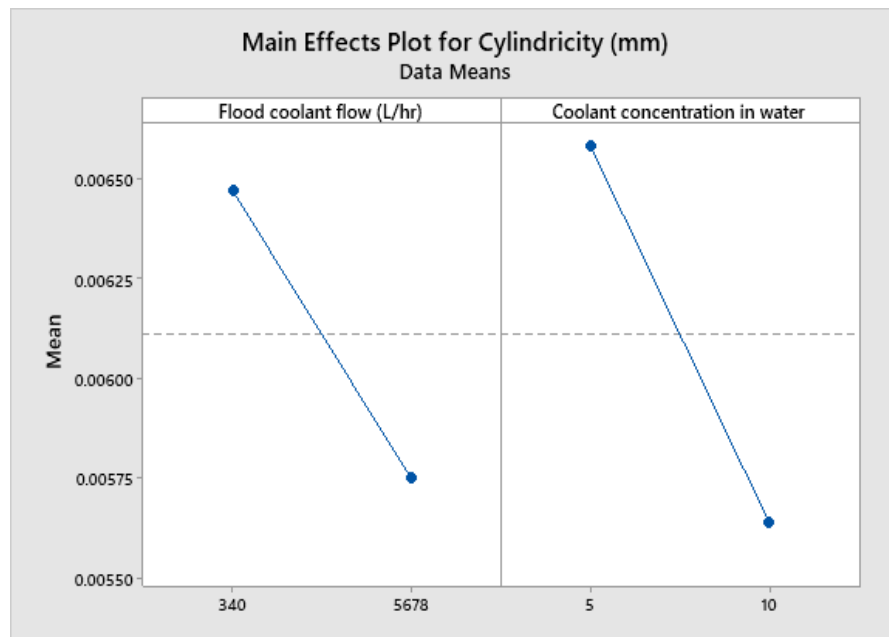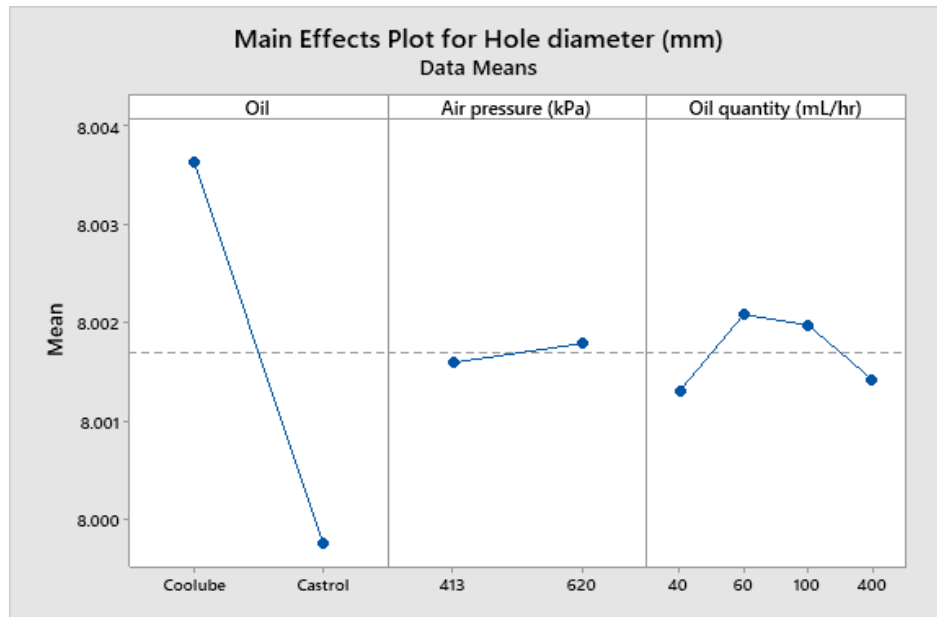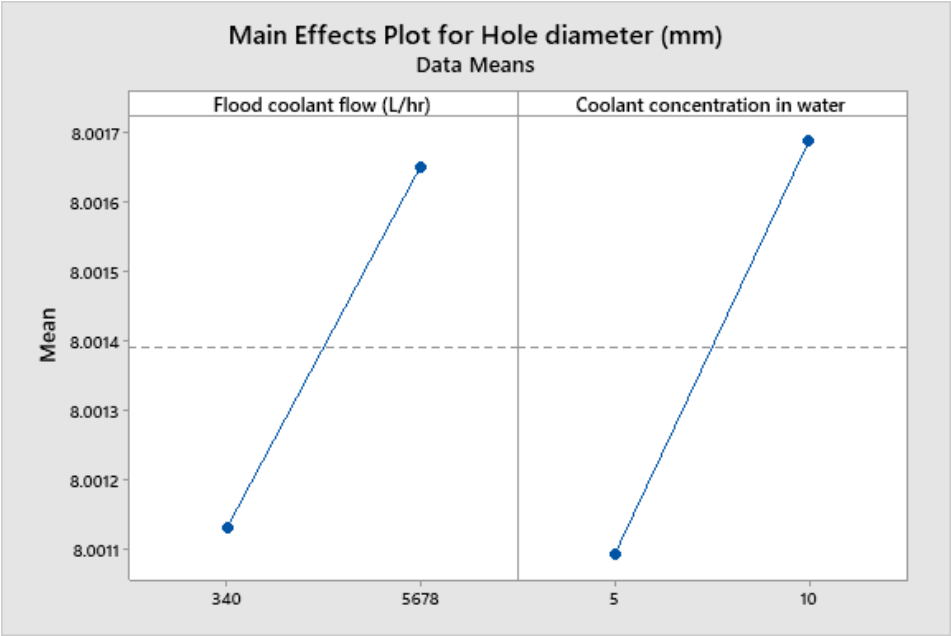
APPENDIX I

PUBLICATIONS

Patil, A., Raval, J., Bangma, T., Edinbarough, I., Tai, B., Stephenseon, D., Suleiman, O., & Hung, W. N. (2020). Characterization and Performance of Minimum Quantity Lubricants in Through-Tool Drilling. International Journal of Engineering Materials and Manufacture, 5(4), 98–115.https://doi.org/10.26776/ijemm.05.04.2020.01